2015

An Improved Adaptive Filtering Approach for Removing Artifact from the Electroencephalogram

Justin Ronald Estepp
Wright State University

AN IMPROVED ADAPTIVE FILTERING APPROACH FOR REMOVING OCULAR ARTIFACT FROM THE ELECTROENCEPHALOGRAM

A thesis submitted in partial fulfillment of the
requirements for the degree of
Master of Science in Biomedical Engineering

By

JUSTIN RONALD ESTEPP
B.S., Wright State University, 2006

2015
Wright State University

WRIGHT STATE UNIVERSITY

GRADUATE SCHOOL

April 16, 2015

I HEREBY RECOMMEND THAT THE THESIS PREPARED UNDER MY SUPERVISION BY Justin Ronald Estepp ENTITLED An Improved Adaptive Filtering Approach for Removing Artifact from the Electroencephalogram BE ACCEPTED IN PARTIAL FULFULLMENT OF THE REQUIREMENTS FOR THE DEGREE OF Master of Science in Biomedical Engineering.

_____

Ping He, Ph.D.
Thesis Director

_____

Thomas N. Hangartner, Ph.D.
Chair, Department of Biomedical,
Industrial, and Human Factors Engineering

Committee on
Final Examination

_____

Julie A. Skipper, Ph.D.

_____

Nasser H. Kashou, Ph.D.

_____

Robert E. W. Fyffe, Ph. D.
Vice President for Research and
Dean of the Graduate School

ABSTRACT

Estepp, Justin Ronald. M.S.B.M.E. Department of Biomedical, Industrial, and Human Factors Engineering, Wright State University, 2015. An Improved Adaptive Filtering Approach for Removing Artifact from the Electroencephalogram.

The biophysics of volume conduction that enable electrophysiological data acquisition also result in the mixing of data sources including possible, undesirable noise sources at the electrode interface. This work specifically focuses on improving the performance of the recursive least-squares (RLS) adaptive filtering method for removing eye movement artifact from the electroencephalogram. In biophysically-inspired simulated data, the RLS algorithm is verified to produce results that are inferior to extended infomax independent component analysis (ICA), the most widely used artifact correction approach in this problem space, due to its non-linear filter phase response and the presence of bidirectional contamination, or cross-talk, resultant of volume conduction in electroencephalographic data. The non-linear phase response of the RLS algorithm is mitigated by restricting its filter coefficients to form a linear phase, Type I finite impulse response filter. A reduced effect of cross-talk in RLS is achieved by filtering the reference noise input signal using a combination of non-local means weighting and Bayesian adaptive regression splines smoothing. When compared to extended infomax ICA, the modified RLS adaptive filtering approach meets or exceeds data source recovery accuracy while retaining highly desirable properties not afforded by blind source separation. These results support the use of a modified adaptive filtering approach for the near-ideal removal of eye artifact data from the electroencephalogram.

TABLE OF CONTENTS

LIST OF FIGURES

LIST OF TABLES

APPENDIX

I. INTRODUCTION

Since Hans Berger first reported the recording of electroencephalography (EEG) from humans in 1929 [1], the subject of artifact in EEG data has been actively studied by researchers interested in understanding cortical dynamics. As Luck points out in his seminal text [2], prominent neurophysiologists at the time of Berger's discovery believed the first recorded human EEG data to be artifactual in and of itself; that is, they believed that some other process, non-neural in nature, was responsible for the slow-wave amplitudes (later characterized as alpha waves with a characteristic frequency range of 8-12 [Hz]) that Berger first observed in 1924. That it took five years between observation and publication of the first recorded human EEG is telling of the skepticism with which Berger's data was reviewed. Soon after, however, Berger's initial findings were observed and confirmed by other prominent neuroscientists at the time [3] [4] [5]).

The controversy surrounding Berger's results can then be viewed as setting the stage for what has been nearly 100 years of research surrounding the recording of EEG and other non-neural artifact (in some disciplines, referred to as noise) sources. The combination of both neural and non-neural signals appearing at a single electrode on the scalp surface is made possible by a principle knowns as volume conduction. In its most basic idea, volume conduction can be described as a process by which electrophysiological signals that are generated within the body can be measured and observed at many locations on the skin surface. In practice, this results in any given electrode on the skin surface being susceptible to any number of signal-generating sources with sufficient proximity and amplitude to be seen with a given resolution,

or dynamic range and bit depth in the digital sense. These signal-generating sources need not be physiological in nature, but can also be caused by environmental electromagnetic interference such as line noise, cable sway, and variable impedance at the electrode-skin interface. Those sources that are physiological in origin and can often be seen in EEG data are electrooculographic, electromyographic, and electrocardiographic in nature. While small-amplitude electrocardiogram (ECG) appearing in the EEG is somewhat rare, the presence of electrooculogram (EOG) and electromyogram (EMG) artifact in EEG is very common.

When the potential for EEG to be contaminated with artifactual data sources exists, it is standard procedure to account for these artifacts, to the degree possible, in subsequent data acquisition and analysis. In a review by Fatourechi et al. [6], these procedures are generally separated into three categories: avoidance, rejection, and removal. Avoidance focuses on data collection and experimental design techniques that minimize the likelihood of artifact-generating conditions. Procedural safeguards include skin preparation under the electrode site (even for high-impedance data acquisition systems, in some cases [7]), reducing and eliminating cable sway, and monitoring for or shielding from line noise artifact from external, AC power sources. Experimental techniques to avoid artifact may involve asking the subject to refrain from certain behaviors such as excessive eye and body movements. While these may seem like reasonable considerations, practical implementation is difficult. It is impossible to completely suppress artifacts associated with eye and muscle movement, and, in fact, such an attempt may lead to changes in the underlying neural data (e.g. [8]).

As a practical consideration, artifact-influenced data segments, or epochs, can simply be removed from further data analysis; this is the artifact rejection approach. Aside from the loss of data that could be particularly detrimental to a study, rejecting artifact-laden data that relies on subjective or objective assessment can be subject to selection bias [9], very labor intensive, and

constrained to models and assumptions regarding what does and does not constitute 'artifact' that may not sufficiently approximate the true noise characteristics.

Artifact removal (sometimes referred to as artifact correction), the third and final approach, is often viewed as the most preferable case for this problem space. Algorithms designed to perform artifact removal start with the contaminated data source and 'clean' the noisy data such that, at its final stage, it closely approximates the actual, underlying EEG signal that would have been recorded without the presence of artifact. Such procedures should result in minimal distortion of the actual EEG data while significantly attenuating or eliminating signatures of non-neural origin. This result satisfactorily addresses worries with avoidance and rejection, namely unintended experimental outcome effects and loss of valuable data, respectively. Not being without concerns itself, artifact removal's single, biggest challenge is in quantifying the ability of any single algorithm to recover an EEG signal of unknown origin. Because volume conduction does not discriminate between the acquisition of signal and noise, it is fundamentally impossible to objectively determine, from any recorded signal, the exact contributions from any underlying data source.

While seemingly problematic, the volume conduction challenge with artifact removal methods can be addressed with careful, theoretical development and realistic simulation testing. Luck [2] presents a particularly approachable comparison to clinical treatment for disease and disorder: as with many medications and therapies, there can be unintended side effects to artifact removal that one should understand in the context of their own data. It is not a question, necessarily, of whether to apply artifact correction, but a matter of understanding the risks of these side effects, how to observe them should they occur, and how to alleviate them such that they do not further complicate the analysis and interpretation of EEG data. This is most readily achieved through a theoretical development and understanding of how any artifact removal

algorithm functions within the biophysical phenomenon of volume conduction. Biophysically-inspired simulation and modeling can be a useful tool to validate and verify algorithm performance in the context of plausibly real structural and functional mechanisms.

This work specifically focuses on understanding and improving the performance of one particular artifact removal technique, adaptive filtering [10], in the context of correcting for eye movement artifact in the EEG. Adaptive filtering, proposed by He et al. [11] [12] as a viable candidate for correcting an EEG signal for eye movement artifact, has been studied in comparison to other algorithm approaches for artifact removal; however, attempts to overcome some of its shortfalls and improve its performance are currently lacking in the literature. To begin, it is necessary to develop comprehension of electrophysiological biophysics as applied to EEG to understand how any algorithm may or not suitably approximate both the foundational anatomy and neural function of EEG. Following this, historical and contemporary artifact correction approaches can be evaluated in the context of this biophysical theory to better understand how each could be reasonably expected to perform under ideal conditions. It follows that algorithm performance under these ideal conditions can then be evaluated using simulations that are suitably derived from biophysical theory; as Nunez points out in his chapter in Wolpaw and Wolpaw [13], any algorithm that does not function well under ideal, simulated conditions cannot be expected to improve when subjected to real EEG data. These simulations, coupled with adaptive filter and EEG biophysics theory, can then be used to develop specific hypotheses and observe them in the context of the error in recovering the true, underlying EEG signal. Using this same approach of theoretical supposition and practical observation, contemporary and widely-used algorithms for artifact correction in EEG can be compared and contrasted to adaptive filtering. Finally, with a better understanding (and observation) of why and how adaptive filtering may be challenged in eye movement artifact correction, improvements can be developed, tested,

and compared with the same contemporary, gold-standard algorithms in use by the EEG community. Using this framework, this work demonstrates that a modified adaptive filtering approach from that presented by He et al. [11] [12] meets or exceeds the minimum recovery error that can be achieved with extended infomax independent component analysis (ICA; [14]), the most widely-accepted and practically implemented eye movement artifact algorithm in contemporary literature, while retaining highly desirable properties not afforded by blind source separation (BSS) approaches.

EEG BIOPHYSICS

To begin, a consideration of the foundational properties of EEG biophysics is necessary to understand how any artifact correction algorithm may be well- or ill-suited to solving the challenges of volume conduction. The discussion presented here is primarily motivated and informed by the writings of Nunez and Srinivasan [15] as well as the summary chapter on the same topic written by Nunez in Wolpaw and Wolpaw [13]. Interested readers should consult these works for additional theoretical, as well as mathematical, expansion and comprehensive reference lists.

EEG is a macroscopic epiphenomenon that is ultimately manifested by electrophysiological activity that exists, and can observed, at smaller, spatial scales. Neuronal activity, originating at the single-unit, or single-neuron, recording scale, can also be represented at microscale and mesoscale with methods for recording local field potentials (LFPs) and electrocorticography (ECoG), respectively. With the exception of EEG, each of these methods requires invasive electrodes to be placed below the skull or on/in the cortex and sub-cortical structures. While single-neuron, LFPs, and ECoG are not further discussed here, it is worth mentioning that each of these techniques captures complementary, and not redundant, information about brain function. The interpretation that EEG, ECoG, and LFPs are simply

observations of the same, single-cell, neuronal activity at differing spatial scales is an unfortunate, but common, misconception. Each method captures unique signatures of neural activity that arise from their unique spatial, structural, and functional properties. Similarly, magnetoencephalography (MEG), or the measurement of small-amplitude (femtoTesla, or 10^8 times *weaker* than earth's) magnetic fields resulting from aggregate, post-synaptic activity that can be observed outside of the head, is also a complementary technique. MEG differs from electrical approaches primarily due to the unique structural organization and orientation of cortical tissue that is not sufficiently represented in EEG.

As a macroscale epiphenomenon, EEG primarily results from post-synaptic potentials originating from large volumes of pyramidal cells that are perpendicularly aligned to the cortex, but aligned in parallel to themselves. To achieve a magnitude that can be observed through the surrounding cortex, cerebrospinal fluid (CSF), skull, and scalp, this post-synaptic activity requires coherence within relatively large volumes of tissue on the order of 10^3 to 10^4 [mm^3] containing approximately 100 million to 1 billion neurons. Although primarily from cortical gyri due to their closer proximity to the scalp surface, tissue found within the sulci and fissures may influence EEG, as well.

At this macroscale, tissue acts as a linear conductor; from an electrical perspective, the surrounding cortical, CSF, skull, and scalp tissue acts as a purely resistive network by which the source cortical activity is attenuated as it propagates to the scalp surface. This effect, with negligible capacitive properties, has been observed in *in vivo* tissue experiments for frequency ranges of interest in EEG from 1 to 40 [Hz]. Since propagation velocity from source to scalp is negligible, the resulting effect is an instantaneous, linear superposition, or summation, of all relevant cortical sources at the scalp surface; this is what is measured as EEG. In reality, the tissue conduction medium is an inhomogeneous network influenced by many properties, such as varying

skull thickness and tissue boundary effects, and also exhibits anisotropic conductivity properties (a directional dependence on conductivity, or resistivity, based on the direction of current flow). A common simplification in forming a biophysical model of EEG relaxes these realities to assume homogeneity and isotropic (directionally independent) conductivity. Of interesting note is that this simplification does not result in significant deviations between predicted and measured EEG data due to assumptions made of other variables, such as individual, local tissue conductivities, that have a far greater error effect. A notional depiction of this structural model for two cortical sources and four electrodes is shown in Figure 1.

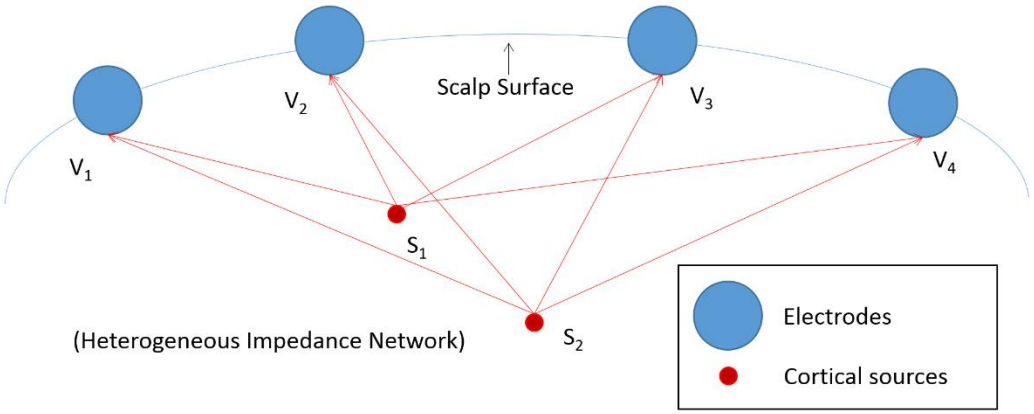

Figure 1. A notional, structural model of EEG biophysics. Sources located on or in the cortex are observed at all spatially-sufficient locations on the scalp surface. This propagation, with negligible delay, results in the instantaneous, linear superposition of these sources at the electrodes on the scalp. A practical, and common, simplification of the model is to assume that the tissue network is heterogeneous and isotropic.

The functional model of these coherent, cortical sources can be considered separately from the structural model. In keeping with the electromagnetic analogy, the aggregate, post-synaptic activity is best modeled as a dipole approximation. The current dipole model assumes a

current source (+) and sink (-) that are close enough in proximity to produce an equivalent dipole; for the single-unit neuron, this holds true at sufficient distances from the actual current-generating processes within the neuron itself. The equivalent current dipole of a coherent, cortical patch is then the linear summation of the underlying, coherent, post-synaptic activity. As with a standard-model electric dipole, the field surrounding the effective current dipole of a single neuron attenuates at an inverse distance-squared rate (assuming a homogeneous, isotopic medium, thus the justification for the simplified structural model). However, in a cortical patch with coherent neuronal behavior, the effect of a volume of coherent, equivalent dipoles leads to an attenuation rate with respect to distance that is, in fact, much slower than the inverse distance-squared rate. As with the structural model, this functional model is a simplification of cortical dynamics that results in a tractable, yet surprisingly sufficient, explanation for observing cortical activity on the scalp surface.

REMOVAL OF EOG ARTIFACT FROM THE EEG

Very early in the history of EEG, when data existed only on paper tape and frequencies were often referred to in counts of zero-crossings, neuroscientists were concerned about the effects of ocular artifact in EEG data. As with much research, the study of ocular artifact in EEG began with characterizations of the artifact. Overton and Shagass [16], as well as others prior, observed both inter-subject differences in artifact amplitude and spatial differences in scalp distribution patterns for individual artifact types. Noting that for specific subjects and specific artifact types the spatial patterns of artifacts seemed to be fixed, early approaches focused on estimating the contribution of artifact as a percentage of observed ocular movement. This was achieved by subtracting scaled versions of the vertical electrooculogram (VEOG) and the horizontal electrooculogram (HEOG) data sources from the EEG using post-hoc methods such as least-squares regression of maximum, observed amplitude differences to determine the correct

percentage [17] or, in an on-line procedure, using potentiometers to attenuate the VEOG and HEOG and subtract it from the EEG [18]. Both of these methods used a series of voluntary eye movements and blinks to determine the correct scaling factors that result in a sufficient attenuation of the ocular artifact.

HISTORICAL VIEWS

The work of Hillyard and Galambos [17] and Girton and Kamiya [18] led to the development of the most prominent, historical approach to correcting for ocular artifact in EEG: linear regression. Verleger, Gasser, and Möcks [19] formalized their conceptual, linear model as follows (Equation 1).

$$OBS(t) = \alpha \cdot EOG(t) + EEG(t) \qquad [1]$$

This linear regression model assumes that the EEG measured at the electrode (or EEG observed, OBS(t) is the actual, underlying EEG (EEG(t)) in a linear combination with a scaled ocular contaminant signal, EOG(t). This ocular contaminant is scaled by the coefficient α, which is reflective of the adjustment in amplitude necessary to accurately represent the artifact amplitude as observed at the EEG electrode. Calculation of α is then accomplished by observing the EEG time series, or some epoch within containing ocular artifact, along with one reference EOG channel [19] used a bipolar channel of VEOG above and below the right eye) and then calculating the regression coefficient of the EOG on the observed EEG.

This work spawned a large effort in the EEG community to adopt regression-based methods for ocular artifact correction. Individual laboratories began to improve upon the method by taking into account such factors as differences between voluntary and naturally-occurring eye artifact and the unique characteristics of blinks [20], averaging over individual artifactual epochs to reduce noise in the regression estimate [21], and the frequency-dependence of artifact

propagation [22].[1] The work of Semlitsch et al. was largely extended by Croft & Barry in a number of publications some years later [23] [24] [25] [26]). A seminal review article by Croft & Barry [27] is an excellent summary of the body of work surrounding regression-based artifact removal approaches.

CONTEMPORARY METHODS

Despite the popularity of regression methods for many years, the most prominent class of ocular artifact removal methods, today, revolves around concepts of dipolar source estimation and reconstruction. The essence of these approaches centers on the notion that artifact can be considered as having a relationship "among all channels", and not just "between all channels" as regression approaches tend to be implemented [28]. The benefit of considering artifact representations in source space is that EEG, as well as the ocular artifact, can be thought of as just another source in the model; this is, in principle, regression methods can be improved by accounting for the EEG activity that is present in reference EOG channels due to volume conduction [29] [30].

From the work of Nunez [13] and Nunez and Srinivasan [15], as discussed earlier, the equivalent dipole model of cortical activity is well understood. What is known, as well, is that there is also an equivalent dipole model of ocular activity. Very early studies seeking to characterize the electrical phenomena of ocular artifact arrived at conclusions that there exists some form of an electric dipole within the eye [31]. As it turns out, the equivalent dipole is the result of a potential difference between the positively charged cornea and the negatively charged retina. These studies also observed that eye movement has unique and differentiable properties

[1] To avoid detracting from this text, a discussion on frequency-(in)dependence can be found in Appendix A; suffice it to say that the reporting of any frequency-dependent properties in volume-conducting processes may result from unquantifiable artifact [85] [106] or a misrepresentation of temporal versus spatial influences [104] and that, by and large, the neuroscience community has adopted a frequency-independent view on volume conduction.

from the eyeblink. While there were competing theories early on, the most widely-accepted explanation for eyeblink artifact comes from Matsuo, Peters, and Reilly [32]: as the eye blinks, the movement of the eyelid as it traverses across the cornea modifies the electrical field associated with the eye itself. Early dipole modeling of electrical ocular activity [33] revealed that the most accurate model consisted of unique dipoles, each with unique locations, for vertical movement, horizontal movement, and blinks. This finding is in agreement with some regression approaches that found the best results when ocular artifact was estimated with three separate regression parameters for vertical movement, horizontal movement, and blinks (e.g. [34]).

Following the biophysical source dipole model for ocular artifact, computational models for representing ocular artifact in source space soon followed. This problem, known as blind source separation (BSS), assumes that what is measured as scalp EEG is a linear summation of the underlying, equivalent sources generated from cortical, ocular, and other types of activity (e.g., EMG); the goal, then, is to identify a linear mixture of these sources that gives rise to what is measured on the scalp.[2] An early example of this was the application of Principal Component Analysis (PCA) to represent the large variance associated with eye movement artifact in EEG as a set of linearly uncorrelated, orthogonal sources [35] [28]. Not long thereafter, Independent Component Analysis (ICA) was introduced as an algorithmic approach to source estimation [36] [37]. While ICA is, by definition, a subclass of algorithms to be considered under BSS, there are numerous ICA algorithm implementations, as well. In general, ICA assumes a set of non-Gaussian sources, **s**, that are linearly mixed by the mixing matrix, **A**, to form the set of observations that are measured at the scalp surface, **x**, as given by Equation 2.

[2] It should be noted here that source estimation, a purely mathematical endeavor, is not equivalent to source localization, which requires some knowledge about the anatomy through which the sources themselves propagate. Source estimation is a functional description of how the sources behave, while source localization is a structural model for where those functional sources exist in a head model.

$$x = As \qquad [2]$$

These sources must meet some criteria for statistical independence, although the specific criterion is a property of each unique algorithm. The first ICA publication by Makeig et al. [36] implemented the infomax algorithm [38]; a later publication by the same research group suggested the extended infomax algorithm [14] may be more suitable for EEG data given its ability to represent source space data as either sub-Gaussian or super-Gaussian [39]. The work published by Vigário [37], developed simultaneously but published after Makeig et al. [36], implemented the so-called fastICA algorithm developed by Hyvärinen and Oja [40] [41]. The methods of ICA have been popularized in an open-source toolbox called EEGLAB [42].

It has generally been accepted that ICA is a more appropriate approach for ocular artifact removal than PCA [43] and its use cases in EEG (e.g. [44] [45]) and fMRI (e.g. [46]) are well documented. As an example of its ubiquity, at this time of this writing, a Google Scholar search of the phrase "ICA AND EEG" returned over 27,000 results <https://scholar.google.com/scholar?q=EEG+AND+ICA>. While ICA (and, more specifically, extended infomax ICA) is perhaps the most widely implemented BSS approach, many others appear in the literature, as well. A sampling of the most popularly-used BSS methods can be found in Delorme et al. [47].

One of the challenging areas in using BSS for EEG artifact correction is the determination of which components appearing in the source space after decomposition are of artifactual origin. Standard procedure for many years after its popularization, and for many labs still today, required subject-matter expert evaluation of the sources based on their scalp topographies, activations, and frequency content to determine if they were of cortical origin and thus should be kept in the final forward projection back to channel space. For data sets of any size, this task requires a significant amount of time and effort. Early efforts to aid in the detection of source artifacts (e.g.

[48] [49]) eventually led to efforts focused on fully-automated identification and removal of artifact of all types (not just ocular) (e.g. [50] [51] [52] [53] [54] [55] [56]). It is also worth noting that while ICA appears more prominently in the literature than any other BSS approach, a number of others have been and continue to be evaluated for improvements in source separation, computational efficiency, and other considerations (e.g. [57] [58] [59] [60] [61] [62]).

ADAPTIVE FILTERING: A PROMISING, NEW APPROACH

He, Wilson, and Russell [11] presented adaptive filtering as a promising, new alternative for removing ocular artifact from EEG. Although the idea sparsely appeared in the literature previously [63] [64] [65], the work by He, Wilson, and Russell [11] was the first to succinctly demonstrate the effectiveness of the algorithm while outlining its potential advantages in comparison to either regression or ICA. In no particular order, these advantages are: 1) a priori calibration is not required (as in popular regression-based methods); 2) the adaptive filter can adjust to dynamic data acquisition conditions, if necessary (which many not be accounted for in techniques requiring a priori calibration); and 3) the adaptive filter can be implemented in real-time with negligible system delay. Further, He, Wilson, and Russell [11] noted that the adaptive filtering algorithm converged quickly (easily removing artifact within the first second of data acquisition) and produced stable results (with respect to increasing the model order). This algorithm can be found implemented in the BCILAB toolbox [66] as the function 'flt_eog.m'.

RECURSIVE LEAST-SQUARES

The variant of adaptive filter implemented by He, Wilson, and Russell [11] was the recursive least-squares (RLS) algorithm. The RLS algorithm, and adaptive filtering algorithms in general, require a reference noise input (or inputs), r[n], that are correlated in some unknown way to noise that appears in the primary input, s[n]. That is to say that the primary input, s[n], is

a linear mixture of desired signal, x[n], and noise, z[n]. The estimated noise-free signal contained within s[n], e[n], is then given by Equation 3.

$$e[n] = s[n] - \hat{r}[n] = x[n] + (z[n] - \hat{r}[n]) \qquad [3]$$

Equation 3 hypothesizes that there is a signal, $\hat{r}[n]$, that estimates the noise component of s[n], z[n]. The purpose of the adaptive filter is to determine a set of filter coefficients of length M, h[m], that estimates the noise component, $\hat{r}[n]$, from r[n], as given by Equation 4. A full proof of the adaptive filtering algorithm, and for the case of two reference noise inputs, is given by He, Wilson, & Russell [11].

$$\hat{r}[n] = \sum_{m=1}^{M} h[m] r[\, n + 1 - m] \qquad [4]$$

Following their 2004 paper, He et al., [12] compared adaptive filtering to a traditional regression method [29] in a number of simulation studies. A theoretical analysis showed that the regression method is actually a special case of the adaptive filtering method (under unique algorithm parameters). These results suggested that adaptive filtering can be conceptually likened to real-time, point-by-point regression that is capable of adjusting to non-stationarity in the relationship between the input reference and actual (measured) noise signals. Simulations whereby the amplitude and phase transfer functions of the simulated EOG noise signal were systematically varied showed that adaptive filtering outperformed the regression method at sufficient model orders (approximately M = 3) for both mean squared error (MSE) of the recovered time-domain EEG and a comparison of band power in typical frequency bands. It is also interesting to note that, for M = 1, the performance of the adaptive filters (in terms of MSE) was quite similar to that of the regression approach. These empirical results support the theoretical derivation of the similarity of the two methods when a set of unique algorithm parameters is used in the adaptive filter implementation.

THE NEED FOR REALISTIC, BIOPHYSICALLY-INSPIRED SIMULATION

One of the most challenging problems for validating any artifact correction approach is that real data prevents the realization of the noise-free signal, x[n] (Equation 3). Volume conduction ensures that data recorded at every EEG electrode are linear combinations of EEG, EOG, EMG, and potentially ECG and other electrophysiological sources. Without knowing the true x[n], quantifying the accuracy of its estimate, e[n], from real data sources is impossible.

The only analytic comparison that can be made using real data is to observe the effects of different artifact removal approaches on a known outcome, like the recovery of an event-related potential [67]. This, however, is faced with two primary deficiencies: first, this assumes that the observed outcome was not an artifactual phenomenon to begin, and second, that artifact correction should 'change' (or, conversely, not change, although the choice of hypothesis may not be particularly clear) the outcome in some meaningful way. Neither of those assumptions are particularly robust, although they may be necessary for real data to be used in evaluation in any capacity. Alternatively, real data can be used to visually inspect the performance of any ocular artifact correction algorithm. While subjective in nature, visual inspection can determine, in a general sense, if the algorithm is performing as expected [11].

A second approach to evaluating artifact correction is to use purely simulated data. Simulated data can be carefully controlled such that an ideal x[n] can be realized. However, simulated data are ultimately generated by a process that may or may not favor certain artifact correction approaches over others. It is also difficult to generate simulated data that are of a level of complexity near that of real data. Some simulation approaches, like those used in He et al. [12], use segments of real data that are presumed to be with and without artifact to build a somewhat realistic dataset; however, the choice to label data as being with and without artifact is subjective

and somewhat at odds with the notion that real data are always a combination of an unknown number, and type, of sources.

A more tenable approach to simulation is to use biophysically-inspired models that consider what are known to be the best representations of electrophysiology-generating processes. These models should incorporate realistic structural and functional elements with simplifications, as necessary (like assuming tissue volumes to be homogeneous and isotropic), to achieve a level of likeness to real data. In this case, the simulated data can be carefully controlled such that an ideal x[n] can be realized, thus facilitating true, quantitative comparison in the estimation of e[n]. If biophysically-inspired, this simulation approach does not inherently favor any artifact correction approach over another any more so than the use of real data; this is, of course, a positive in that any predisposition to unique algorithmic properties would likely be transferred to the real-data scenario. To increase the fidelity of the simulation, limited, real data could be used as part of the simulation for situations that are difficult to simulate, so long as the integration with the simulated data was done so in a biophysically-plausible manner.

AN IMPROVED ADAPTIVE FILTERING APPROACH

As noted in the discussion of He et al. [12], adaptive filtering is not without potential limitations that need to be further investigated. The most compromising issue with the method is that of bidirectional contamination, or 'cross-talk', that results from the volume conduction of multiple signal sources. In the simulations by He et al. [11] [12], the input noise reference EOG signals were considered to be free of any 'contamination' from nearby EEG sources; this is, in fact, not necessarily a valid assumption (but does not take away from the theory and proof of the usefulness of the method itself). As observed in data from work implementing the adaptive filter for EOG artifact correction (e.g. [68] [69]), it would appear that adaptive filtering over corrects frontal and fronto-temporal EEG channels. This effect is not entirely unanticipated as these

channels most heavily influence the cross-talk observed in the reference noise input EOG channels. Mitigating this effect requires one of two equally promising approaches: 1) conditioning the EOG references to reduce any bidirectional contamination from nearby EEG sources, or 2) finding a secondary reference noise input that can be used to correct for EOG artifact, but is not derived from EOG (that is to say, a secondary reference noise input that is not subject to bidirectional contamination).

Some cursory attempts have been made to condition the input reference noise EOG signals to improve cross-talk. Wallstrom et al. [70] estimated a filtered EOG signal using free-knot splines [71] prior to implementing a regression-based correction while Romero, Mañanas, and Barbanoj low-pass filtered the input reference noise EOG signals prior to adaptive filtering. While the performance of the low-pass filtered inputs used by Romero, Mañanas, and Barbanoj [72] was somewhat poor, this is to be expected – a simple low-pass filter will not alleviate cross-talk in the designed pass-band (at a cutoff frequency of 7.5 [Hz], the delta (0.5-3 Hz) and theta (4-7 Hz) bands were in the pass-band, but alpha (8-12 Hz) was within the stop-band of the low-pass filter). Interestingly enough, promising methods for noise reference input signal conditioning, like those demonstrated to be effective in Wallstrom et al. [70], have not been evaluated for their utility in adaptive filtering implementations.

Recent literature has shown promise in the use of eye tracking technology as a secondary reference noise estimate [73] [74] [75] [76]. Despite the attractiveness of such a method, the use of eye tracking data as a reference noise input to the adaptive filtering method has only seen limited investigation. It can be reasoned that the derivation of the exact reference noise inputs to use may be somewhat unobvious, given that there is no common noise estimate used in available literature to date. Kierkels et al. [74] simulated gaze data from a dipole model as an input to a Kalman filter, Noureddin, Lawrence, and Birch [75] used pupil-derived signals as inputs to both

recursive least-squares (RLS) and H∞ [77] [78] adaptive filtering algorithms, and Plöchl, Ossandón, and König [76] only use eye tracking data as a method to identify components related to EOG artifact that resulted from an ICA decomposition. At the very least, the addition of eye tracking as a necessary source to obtain an independent reference noise input could be an unnecessarily complicated requirement should better-conditions reference noise inputs be otherwise obtainable from electrophysiological sources.

While the performance of BSS -based approaches has been frequently demonstrated to be superior to other approaches (e.g. [72]), others have shown regression-based approaches (e.g. [70] [56]) to exhibit better performance. While Romero, Mañanas, and Barbanoj [72] directly compared BSS and RLS adaptive filtering methods (among others), there are few other published studies where a direct comparison of BSS to adaptive filtering was made. There are also a limited number of examples where adaptive filtering is combined with BSS to take advantage of the most positive attributes of both. Chan et al. [79] used ocular sources as derived from a BSS implementation (Second-Order Blind Inference, or SOBI; [80]) as the reference noise inputs to an RLS adaptive filter. With some additional processing of these reference noise inputs, the RLS adaptive filter achieved better performance over SOBI and infomax by themselves, and also better than the standard RLS adaptive filtering using VEOG and HEOG as dual reference noise inputs. This is, presumably, due to the reduction of cross-talk in the reference noise inputs that was achieved by extracting them from the SOBI-derived source space. In a slightly different approach, Klados et al. [81] assumed that there was still some residual EEG even in ICA-decomposed source components of primarily artifactual content. To preserve this residual EEG (from an extended infomax decomposition), an RLS adaptive filter, using VEOG and HEOG as dual reference noise inputs, was used to remove the EOG artifact from the source space artifactual channels, leaving only the residual EEG to remain. A forward-mixing of the source matrix after correction using the

RLS adaptive filter produced more accurate results than two other evaluated methods, LMS adaptive filtering and a wavelet-enhanced ICA implementation [82]. Somewhat surprisingly, the authors of this study did not compare these new results to either traditional RLS or extended infomax ICA.

While both of these approaches combining adaptive filtering and ICA are designed to take advantage of the strengths of each, the primary goal was to reduce cross-talk in the reference noise inputs [79] or, conversely, the primary input [81] used by the RLS adaptive filter to prevent over correction due to bidirectional contamination. It if would be possible to achieve cross-talk attenuation in the reference noise inputs to the adaptive filter without having to rely on BSS to do so, it is likely that the necessity of the BSS application in both of these new algorithms could be eliminated.

A NOVEL, ANALYTIC APPROACH

Even in cases where carefully simulated data are used to evaluate algorithm performance, thus avoiding the quantitative evaluation problem using real data, the choice of empirical measures for objectively comparing artifact removal between methods is non-trivial. Across the variety of references mentioned here, there are many different analytic paths taken: voltage time series, power spectra, learning algorithm performance, and power in traditional, clinical frequency bands are some of the outcome measures considered, with comparisons such as visual inspection, mean difference, percent error, mutual information, correlation, root/mean-square error, residual variance, signal-to-noise ratio (SNR), receiver operating characteristic (ROC) curves, classifier accuracy, sensitivity, specificity, and many others appearing at least once. It is not the goal of this work to determine or suggest which approach, or combination of approaches, may be most broadly applicable; it is reasonable for researchers to choose outcome metrics most suited to their specific application. Given a common dataset, some labs may choose to perform large-

scale simulation analyses on dozens of approaches to determine what may be most suitable to for their specific purpose [83].

Klados et al. [81] introduced a somewhat novel concept to their work. In addition to quantifying aggregate performance of any algorithm over an entire time series, they chose to qualitatively represent their results in two, complementary ways: accuracy at removing the ocular artifact and distortion of the original EEG time series. This was achieved by visually inspecting pre-artifact EEG to estimate distortion of the underlying EEG source data in addition to also visually inspecting the ocular artifact period as an estimation of the quality of the artifact removal. Even though their quantitative comparisons were calculated over the entirety of the time series, the qualitative approach to separately examine artifact removal and EEG preservation (in the absence of artifact) is of value.

SUMMARY

This introduction has covered prior art in ocular artifact correction in order to provide sufficient background and theory in the pursuit of improving the adaptive filtering method. From this review, the key points are summarized as follows:

- There are equivalent dipole models of both EEG and ocular artifact; this allows for complete functional simulation to be accomplished using equivalent dipole sources.
- BSS techniques, preceded by regression methods, have dominated the ocular artifact correction literature for much of the published research history on EEG. Only recently has adaptive filtering been popularized in the literature; based on early successes, it warrants further investigation given the nature of its suitability for many applications. As a point of comparison, BSS approaches should be considered along with any adaptive filtering implementation in order to provide benchmark performance. As adaptive filtering can be considered a special form of regression (and, in some literature, this wording is used

interchangeably to include adaptive regression, as well), it is not necessary to consider an explicit form of regression algorithm for comparison.

- Rigorous, quantitative comparison of algorithm effectiveness can only be achieved for carefully simulated data. While this should only be a first step toward understanding any artifact removal method, it stands to reason that any method that does not perform well under simulation will not perform well on real data. In order to ensure translation of the observed algorithm performance in simulation data to real data, the simulation should take into account the structural and functional biophysical models that are known to represent both EEG and ocular artifact as measured on the scalp surface. Where sensible to do so, model simplifications may be made for computational purposes.
- Although few in number, limited efforts to improve the effectiveness of adaptive filtering have focused on implementing secondary BSS approaches for reducing the effects of bidirectional contamination, or cross-talk, on the reference noise input signals used to form the adaptive filter; beyond simple techniques such as low-pass filtering, reducing cross-talk in the reference noise inputs using other means has not been sufficiently explored.
- The ability of any algorithm to effectively remove ocular artifact, when present, is equal in importance to the ability of that same algorithm to avoid distortion in the underlying EEG when ocular artifact is not present. A more complete examination of ocular artifact removal algorithm performance should take both of these properties into account, both subjectively (visual inspection) and objectively (empirical evaluation).

From regression characterization, the equivalent dipole model, and the separation of sources in BSS source space, is it well known that total ocular artifact must be represented by a minimum of three sources: horizontal movement, vertical movement, and blinks. This initial

investigation focused independently on blink artifact as a method to examine hypotheses for a single artifact type; expansion to vertical and horizontal artifact will be achieved in future work.

II. METHODS

METHODOLOGY GOALS

In line with the overall goals of this work, the methods described in this section were selected with specific purposes in mind. These purposes are generally aligned to three primary advances in the adaptive filtering method: the creation and implementation of a biophysically-inspired simulation model, the restriction of the adaptive filter to a linear-phase frequency response, and the reduction of the effects of cross-talk, or bidirectional contamination, in the reference noise input channel.

BIOPHYSICALLY-INSPIRED EEG SIMULATION: BESA SIMULATOR

To realize the structural and functional properties of EEG neurophysics, BESA Simulator (Version 1.0, June 2013; BESA GmBH, Graefelfing, Germany) was used to create realistic EEG signals as they would appear on the scalp surface. Simulator is a freeware program, written by Patrick Berg, for the purpose of using underlying equivalent dipole sources to simulate scalp surface EEG. Within the framework of Simulator, individual dipole sources can be defined within a four-shell head model [84] that simulates the linear, instantaneous summation and propagation of the dipole sources through cortex, CSF, skull, and scalp. Default values for shell (layer) thickness and conductivities were used and are displayed, below, in Table .

Table 1. Default parameters used for the four-shell head model in BESA Simulator. A default head radius of 85 [mm] was used along with the default conductivities from BESA Simulation.

Layer	Thickness [mm]	Conductivity [S/m]
Scalp	6	0.33
Bone	7	0.0042
CSF	1	1.0
Cortex	---	0.33

In addition to individual dipole sources, Simulator can also simulate background EEG that exhibits characteristic spatial coherence on the scalp surface and generally follows the $1/\sqrt{f}$ magnitude falloff of scalp EEG frequency spectra. To create the true EEG data source, **EEG**(c,t) (where c is the channel, or electrode, index, and t is an index of time), Simulator was used to create a sufficiently long time series for which the first 15 minutes of data (sampling frequency, f_s = 256 [Hz], or 230,400 data points) were kept for further analysis. Using parameters as indicated in BESA's Raw Data Simulation Wizard, the background EEG data were set to a root-mean-squared (RMS) amplitude of 7.5 [uV], with the alpha proportion set at 0.8 of the RMS amplitude. A 64-channel electrode montage was used; separate channels for bipolar VEOG (inferior to and superior to the left eye on the orbital bone), HEOG (on the outer canthus of each eye), and left and right mastoids, for a total of 70 simulated data channels. The channel montage is shown in Figure 2. The reference montage was set to common-average.

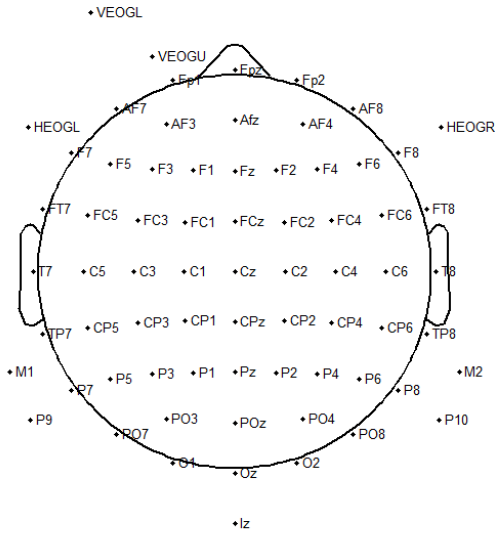

Figure 2. The 64-channel EEG montage used for data simulation in BESA Simulator. Additional electrodes for bipolar VEOG and HEOG, and left and right mastoids, have been added. Electrodes below the horizon of the axial view are shown with a flattened projection perspective.

EEGLAB [42] (v13.4.4b) was used in MATLAB R2011b (The Mathworks, Inc., Natick, MA, USA) for basic plotting and visualization functionality. A 5 [s] sample of the simulated data

generated by Simulator, with an inset showing the power spectrum of the first channel (Fp1), is shown in Figure 3. A closer look at Fp1, AF7, and AF3 is shown in Figure 4.

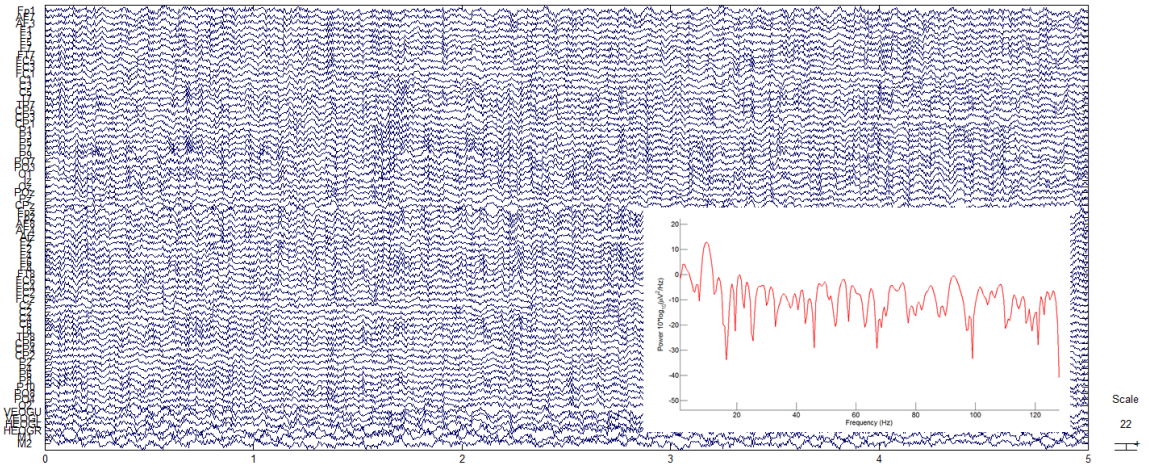

*Figure 3. Simulated EEG data, **EEG**(c,t), from BESA Simulator. Data are shown on a 5 [s] window. Note that the simulated EEG data exhibit spatially-coherent properties for electrodes that are in close proximity. The inset (bottom right) shows the power spectrum for the first data channel, Fp1; note that it follows the general $1/\sqrt{f}$ magnitude falloff with respect to frequency. An increase in alpha power can be observed at f = 10 [Hz].*

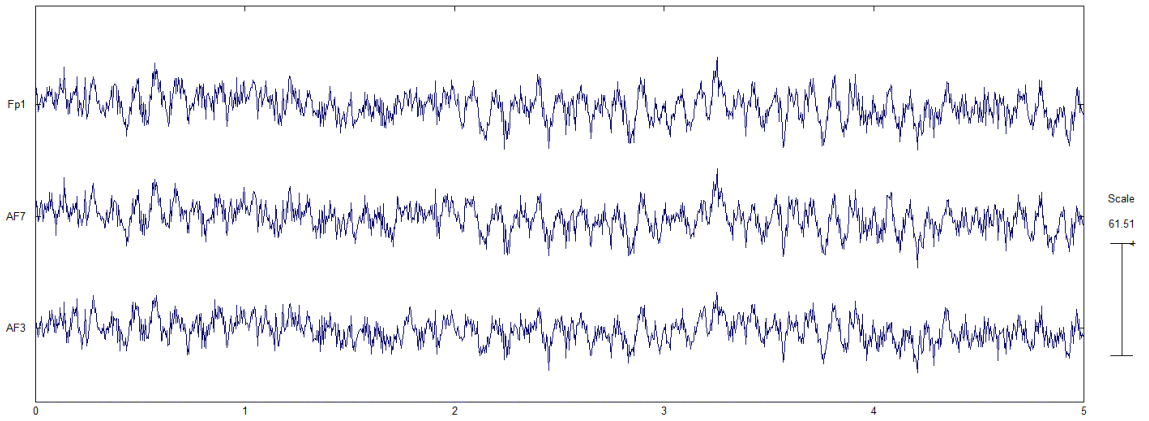

Figure 4. Detailed simulated EEG data (Fp1, AF7, and AF3). This is the same data as shown in Figure 3, shown on the same time scale (a 5 [s] window). The spatial coherence of electrodes in close proximity to one another is more easily seen here; Fp1, AF7, and AF3 are located next to each other in the electrode montage (Figure 2).

The EEG data, **EEG**(c,t), generated by Simulator is in generally good agreement with properties of real EEG data that would be observed in scalp recordings. In addition to the $1/\sqrt{f}$ magnitude falloff with respect to frequency, the simulated EEG also exhibits local, spatial coherence for electrodes that are close to each other, this accurately capturing the nature of volume conduction. A larger-amplitude alpha source centered at f = 10 [Hz] can also be observed

in the data. This alpha source was included in the simulated data so that a common signal of some interesting consequence, and not just coherent background noise, could also be represented in the data. The simulated EEG time series are also of an appropriate peak-to-peak amplitude of less than 50 [uV] (Figure 4), a property that would also be expected of artifact-free EEG. This simulated EEG data sufficiently meet both the structural (four-shell model) and functional (equivalent dipole simulation) requirements for biophysical plausibility in generating the simulated EEG, or x[n], the true, artifact-free data. The second part of the simulation requires that the same be applied to the simulated ocular artifact data, as well.

A QUASI-SIMULATED EOG ARTIFACT

Simulating a sufficient EOG artifact source requires careful consideration of the properties of ocular artifact. As previously mentioned, the work presented here focuses on eye blink artifact only in strict simulation and can be extended to other artifact sources in future work. From Berg and Sherg [33], a sufficient dipole model for blink artifact can be achieved with a single, equivalent dipole at each eye location. The placement of these dipoles in the four-shell model satisfies the conditions for a biophysically-plausible structural model; the results of this structural model, as implemented in Simulator, are shown in Figure 5.

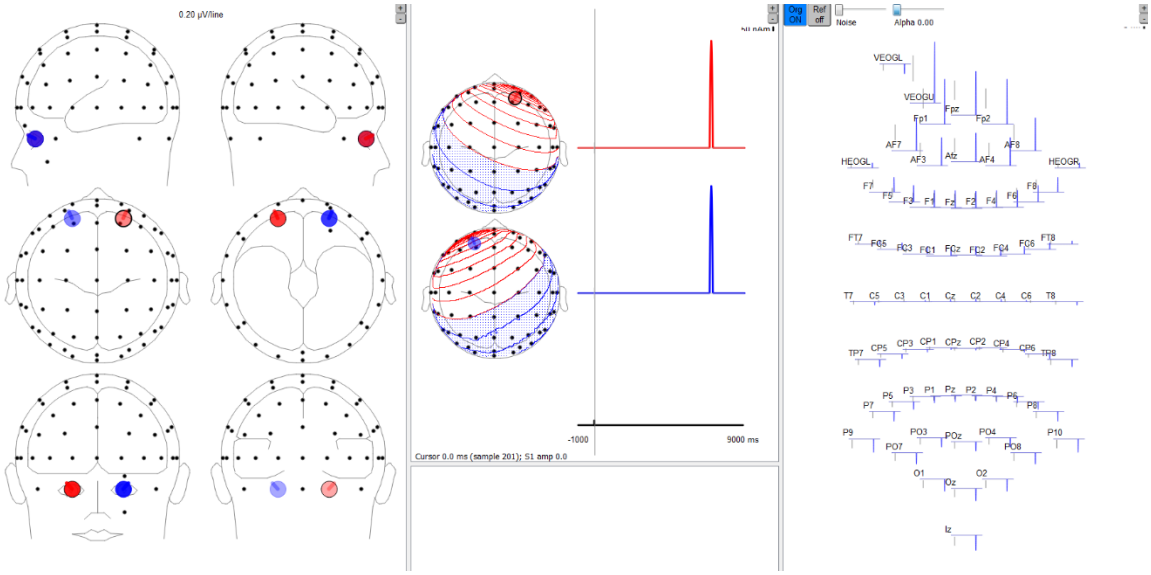

Figure 5. The eye blink artifact dipole (structural) model. As described by Berg and Sherg [33], the ocular eye blink can be sufficiently characterized by a single dipole place near each eye. The left panel shows the physical location of the simulated dipoles. The middle panel shows the spatial, or topographic, maps for each of the dipoles along with an artificial eye blink representation (one-half of a since wave with a frequency of 2.5 [Hz], or an approximate blink duration of 200 [ms]). The resulting, equivalent contribution at the scalp electrodes by what is simulated by the dipole model is shown in the right panel. Note that the functional representation of the eye blink in this figure is for illustrative purposes, only; actual eye blink functional simulation was achieved by a different process as described in the following text.

As with the simulated EEG data, the structural model, with illustrative functional properties only, generates properties of blink artifact in the scalp electrodes that would be expected in real EEG data. Eye blink artifact contamination is most severe in the frontal and front-temporal electrodes, with overall eye blink amplitude generally decreasing as the montage proceeds posteriorly. Occipital and parietal electrodes are most generally affected by the negative polarity of the equivalent blink dipole, with overall artifact amplitude less than what would be seen in the frontal and fronto-temporal electrodes.

Construction a functional eye blink model that is well representative of what naturally occurs in ocular electrophysiology is not achievable with ‘simple’ functions such as the half-cycle 2.5 [Hz] since wave that was shown in Figure 5 for illustrative purposes. Characteristics of spontaneous blinks vary in amplitude and duration; as reported by Lins et al. [85], spontaneous

and volitional blinks have different properties from each other, as well. The closing phase, from the onset of the blink to its peak at closing or partial closing, is shorter in duration than is opening phase, from its peak at closing or partial closing to open again. Half-amplitude duration as reported by Lins et al. [85], or the duration between the half-closing amplitude points on both the opening and closing phases of the blink, averages between 100 and 200 [ms].

While a suitable function could be created in order to simulate blink activity, its properties would have to be substantially varied in order to capture the inherent variability in natural blink characteristics that are expected to be see. A more practical approach, as implemented by He et al. [12], is to extract a set of canonical blink exemplars from real data and condition them to be suitable for use in simulation. This technique preserves the natural variation in blink properties that would be difficult to achieve in a purely computational simulation while, at the same time, providing a characterized source for blink artifact that is ideally free of cross-talk contamination from EEG. For the data presented here, a total of 60 blinks were extracted from a dataset collected using a BioSemi ActiveTwo (BioSemi B.V., Amsterdam, The Netherlands). The original BioSemi data were recorded at 2048 [Hz] from a 128-channel electrode montage with the additional VEOG, HEOG, and mastoid channels described in the simulated montage used here. After translating the raw dataset to a common-average reference and downsampling to 256 [Hz], blink artifacts were visually identified from the VEOG electrode placed superior to the left eye on the orbital bone, VEOG(-) (in the traditional bipolar representation, the bipolar VEOG channel subtracts the superior electrode from the inferior electrode, or VEOG = VEOG(+) – VEOG(-), which results in blinks being negatively oriented in the time series data with maximally achieved negative amplitude from the bipolar configuration). An example data segment from VEOG(-) is shown in Figure 6. At this electrode site in the VEOG bipolar pair, the blink artifact consists of a large, positive amplitude signal on the order of 100 to 200 [uV]; this electrode site was preferentially

chosen over the VEOG electrode place inferior to the left eye as its characteristic amplitude is somewhat smaller (and negative) due to the orientation of the equivalent blink dipole. Quite convincingly, the simulated properties of the blink dipole structural model with illustrative functional blink profile, as shown in Figure 5, exhibits the exact same characteristics as the simulated VEOG electrode locations.

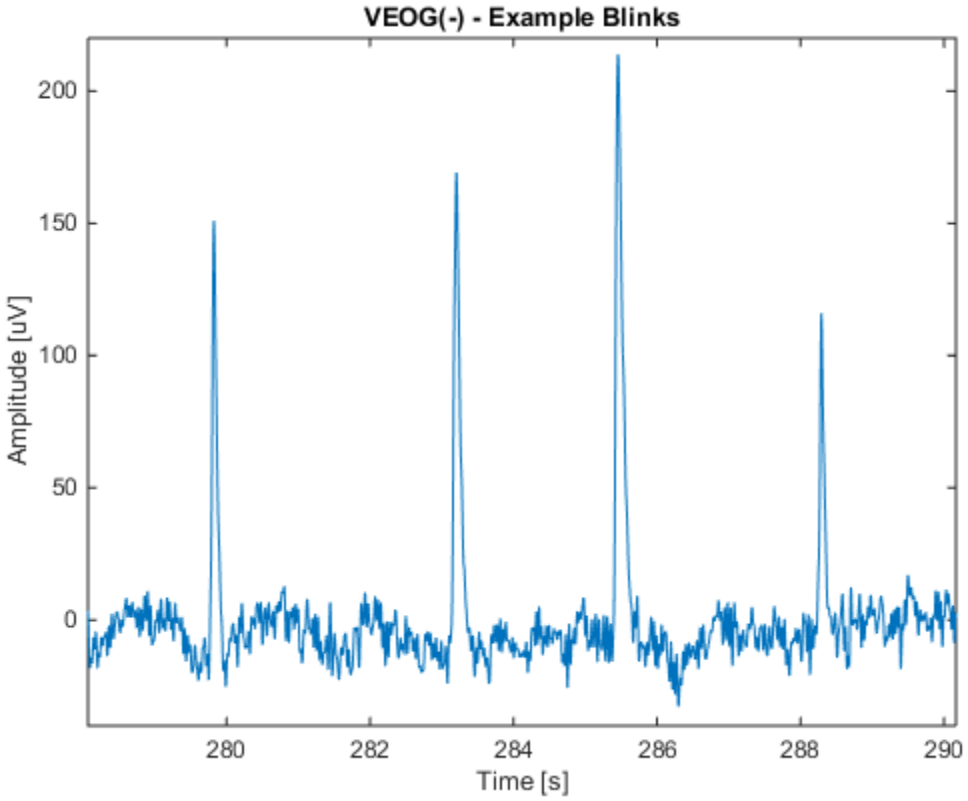

Figure 6. Example segment from VEOG(-), the negative electrode in the traditional, bipolar EEG channel formed from electrodes above and below the left eye. This segment shows 4 (of the 60) blinks that were ultimately chosen for the simulated blink data exemplars.

Prior to extracting the 60 individual blink exemplars, the VEOG(-) channel was smoothed using a smoothing spline approach [12] to reduce the EEG cross-talk effect, thus resulting in a blink channel that is primarily free of EEG contribution. The chosen algorithm to accomplish spline smoothing was the default smoothing spline option in the MATLAB (2014b) curve fitting toolbox, or 'cftool'. An exploratory analysis was completed to choose the best smoothing parameter, p;

the results of this analysis, with a final choice of p = 0.99999, are shown in Figure 7. The choice of this smoothing parameter resulted in preservation of the original blink amplitude while also achieving a significant attenuation, or smoothing, of the contaminating EEG data.

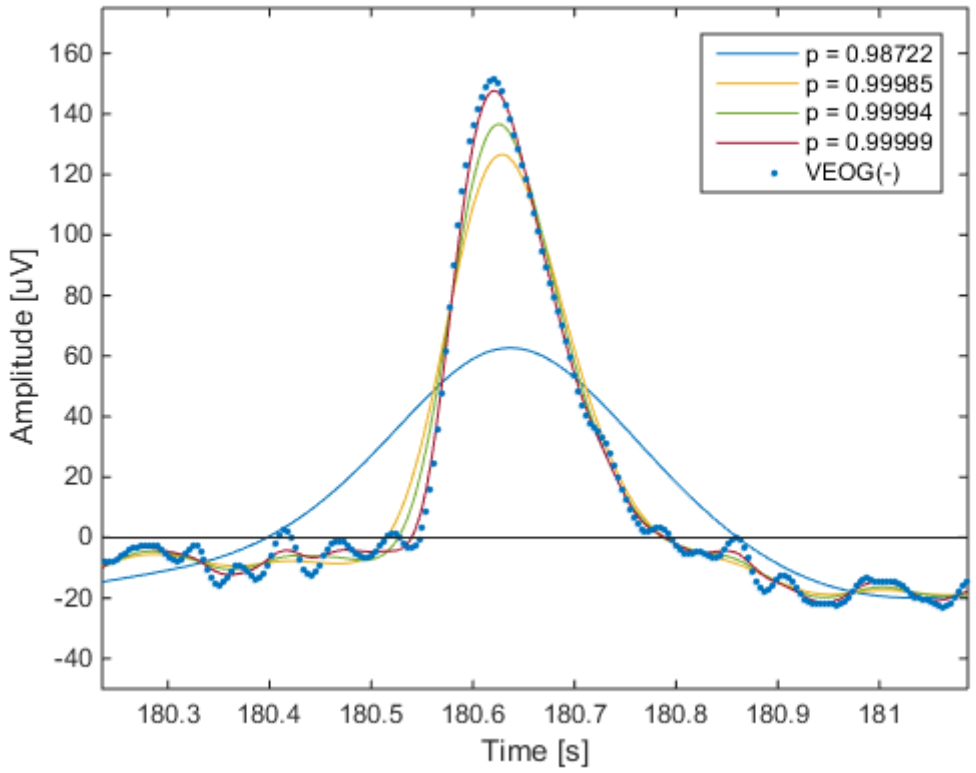

Figure 7. Exploratory analysis for smoothing VEOG(-). The final choice of smoothing parameter, p, was determined based on the overall preservation of the blink in tandem with attenuation of the contaminating EEG due to volume conduction. Final simulation used the value of 0 = 0.99999. While not shown here for clarify of the figure, other choices of p that were investigated were p = {0.99825. 0.99990, 0.99998}.

After spline smoothing, each of the sample blinks was clipped from the smoothed VEOG(-) in windows centered at the peak of the blink closure and of a duration lasting 0.5 [s], or 128 data points. In order to avoid discontinuities in later simulated data, the blinks were adjusted to have an amplitude of 0 [uV] at the beginning and end of each blink segment. This was achieved by tapering each blink artifact segment at its endpoints with a Hanning window of equal duration. An example blink segment, Hanning window, and final, smoothed blink example are shown in Figure 8.

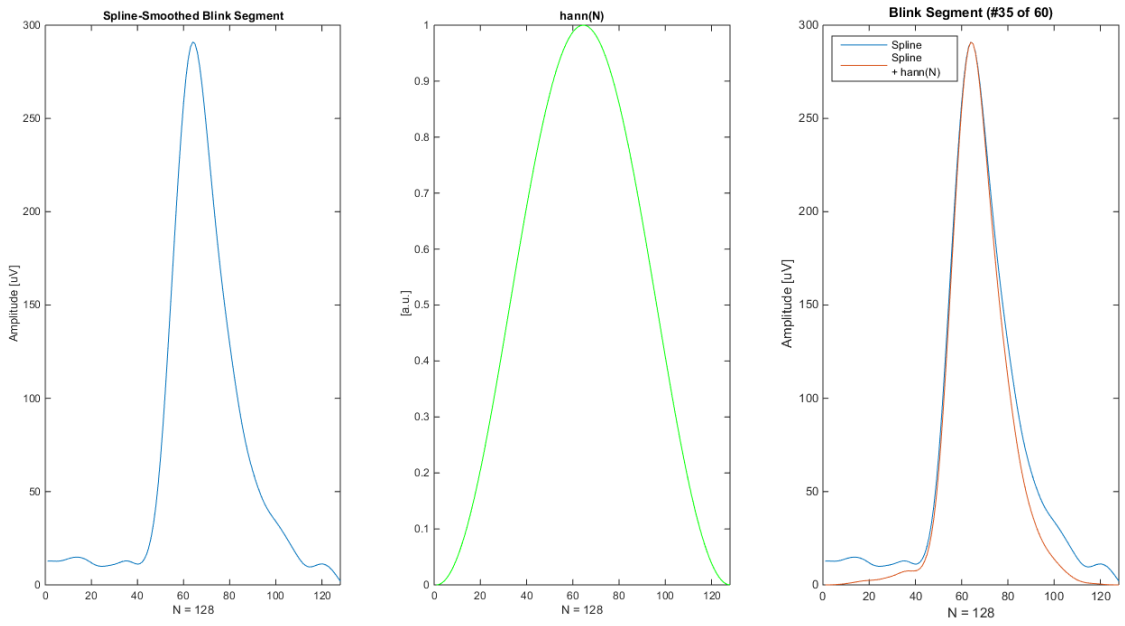

*Figure 8. Example of smoothed, tapered blink artifact. The left panel shows the spline-smoothed blink, while the middle panel shows the N = 128 point Hanning window. The resulting, tapered blink artifact segment, Spline*hann(N), is shown in the right panel along with the original, spline-smoothed segment (to observed the effect of applying the Hanning window). The example shown in this figure is exemplar # 35 of 60.*

To match the simulated EEG data, **EEG**(c,t), in dimensionality, the 60 blink exemplars were first added to a zero-vector of length N = 230,400 at regular, 15 [s] intervals, starting at t = 7 [s]. Having been composed of data originating from a real recording at VEOG(-), the resulting vector time series became the source blink artifact waveform at the VEOG(-) electrode, represented as the row vector **blink**(t), a [1xN] vector; alternatively, this vector can also be thought of as the equivalent source dipole for blink artifact projected onto VEOG(-). As the dipole model for blink artifact consists of two dipoles, one at each eye, the equivalent source dipole for blink artifact, then, is the linear summation of the two dipoles. Since the four-shell model is a purely resistive model, individual projections of the blink artifact equivalent source dipole at all other electrodes can be determined by simulating a single dipole with known amplitude in the same four-shell model and calculating the ratio of its projected amplitude at all other electrodes to the amplitude measured at VEOG(-). This was accomplished using the illustrative source dipole in Figure 5.

Individual projections of the blink artifact equivalent source dipole as referenced to VEOG(-) are shown topographically in Figure 9.

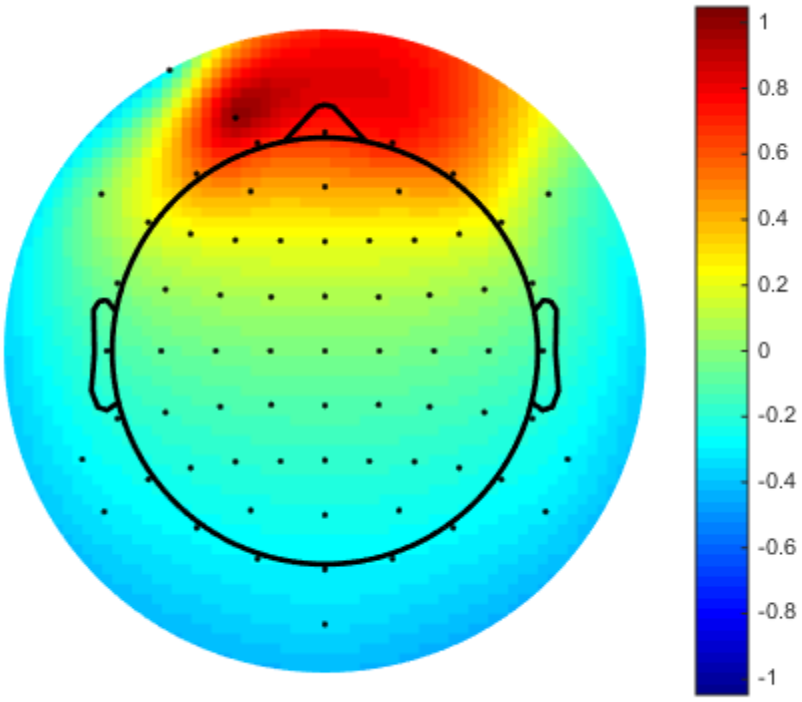

Figure 9. Projection of the blink artifact equivalent source dipole as referenced to VEOG(-). It is possible to determine this projection as referenced to VEOG(-) given that the four-shell model assumes a purely resistive, isotropic conduction medium. Note that the relative projection is maximal, or equal to 1, at VEOG(-); practically, this demonstrates the justification for using VEOG(-) in the common bipolar montage for measuring VEOG, as the blink artifact source projects most strongly to the supraorbital ridge given its orientation.

The vector representation of the topographic data presented in Figure 9 is a [70x1] vector containing the coefficients indexed at each electrode; let this vector be defined as the column vector **blinkcoeff**(c), where c is the appropriate channel index. The source blink matrix, **BLINK**(c,t), is then given by Equation 5. A representative sample source blink matrix is shown in Figure 10.

$$\mathbf{BLINK}(\mathrm{c},\mathrm{t}) = \mathrm{blinkcoeff}(\mathrm{c}) * \mathrm{blilnk}(t) \qquad [5]$$

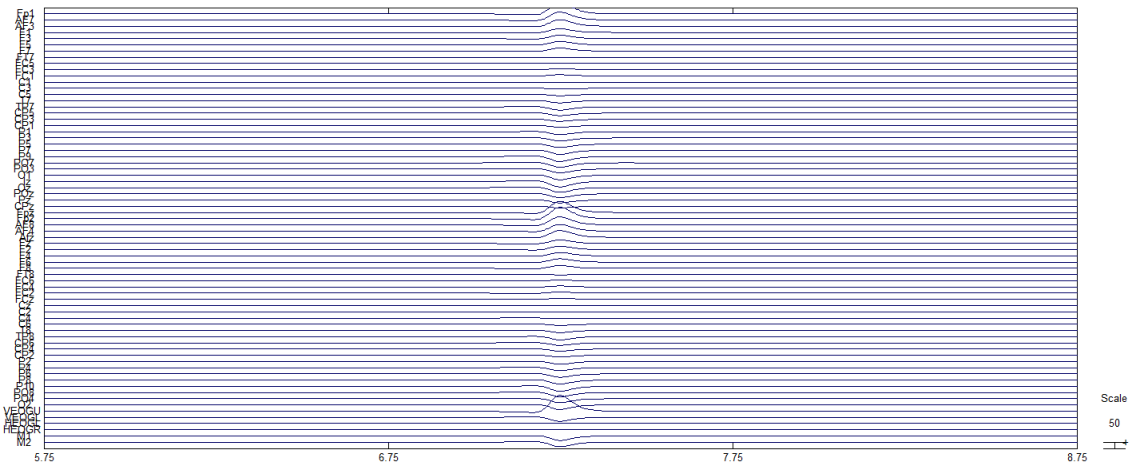

*Figure 10. A representative sample of **BLINK**(c,t) shown over a 3 [s] window. The blink artifact can be visible seen at t = 7.25 [s]; when a blink is not present, the waveform amplitude at each electrode has an amplitude of 0.*

The result of these simulations, one for **EEG**(c,t), and one for **BLINK**(c,t), provides the independent, cross-talk free source waveforms for each source datatype. The final step to achieving the fully-simulated data set is to calculate the linear summation of the EEG and blink source data matrices, given as **S**(c,t); the linear summation is defined in Equation 6, and the fully-simulated dataset is shown in Figure 11. Note that Equation 6 is of the same form as Equation 3 that defines the primary input of the adaptive filter, s[n] = x[n] + z[n]. Using this simulated dataset, the independent, cross-talk free sources of signal, x[n], and noise, z[n], are explicitly defined; therefore, the performance of all ocular artifact removal algorithms can be objectively quantified given that the data space has been simulated as a function of a biophysically-inspired model.

$$\boldsymbol{S}(c,t) = \boldsymbol{EEG}(c,t) + \boldsymbol{BLINK}(c,t) \qquad [6]$$

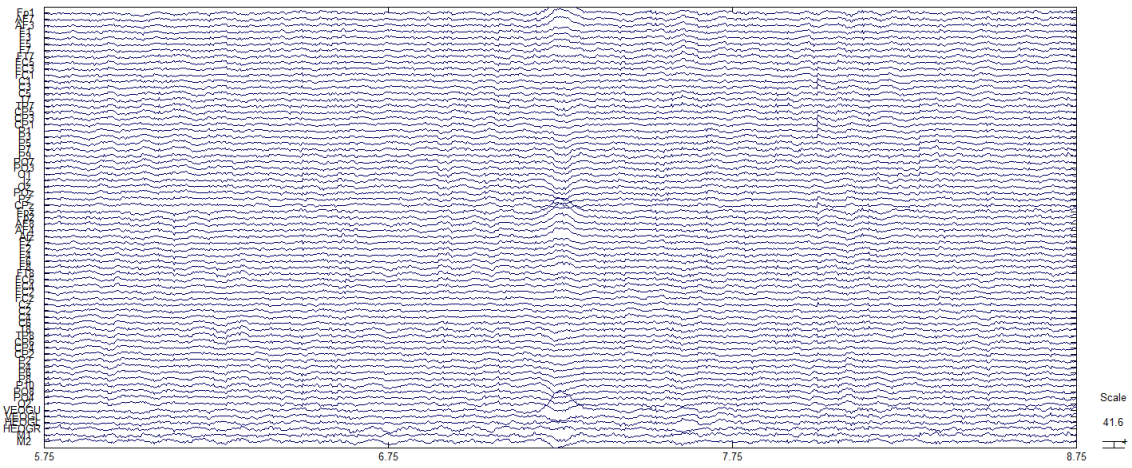

*Figure 11.The fully-simulated dataset, **S**(c,t). Shown on the same time scale as **BLINK**(c,t) in Figure 10, the linear summation of **EEG**(c,t) with **BLINK**(c,t) is easily noticeable. As in Figure 10, the blink artifact appears at t = 7.25 [s].*

EXTENDED INFOMAX ICA DECOMPOSITION

As extend infomax is one of the most widely purposed ICA algorithms for EEG data analysis, it was used as the ICA implementation in this work and considered as the *a priori* best case for ocular artifact correction. EEGLAB's implementation of extended infomax, the 'runica' function in MATLAB (R2011b), was used to perform the source space estimation given x = **S**(c,t), per Equation 2. In order to frame the choice of any further methodology, results for the extended infomax source space estimation are presented here. In the source space, **s** (per Equation 2), eye blink activity isolated to a single component (IC #1). Its spatial map, or the vector in **A** describing its projection to the scalp surface, along with its component activity, are shown in Figure 12.

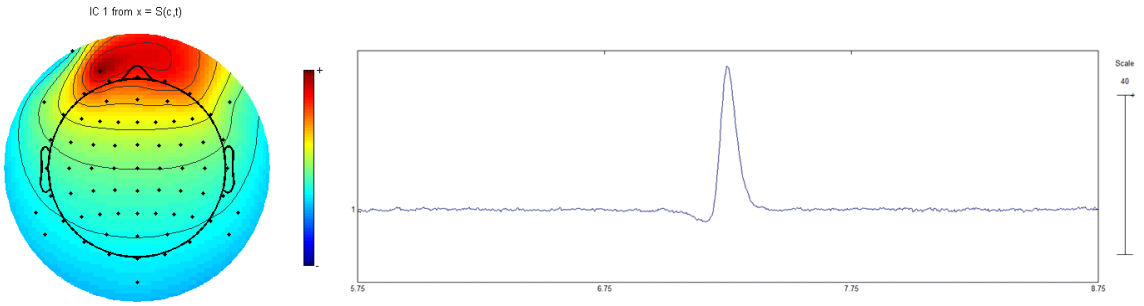

*Figure 12. Results from the extended infomax source estimation of x = **S**(c,t). The entirety of the blink artifact was represented in a single component, IC #1. Its spatial map, or the vector in **A** describing its projection to the scalp surface, is shown in the left panel. The right panel shows a 3 [s] window of its component activity (and is, in fact, the same 3 [s] window shown in Figures 10 and 11). The amplitude scales of both the spatial map and component activity are arbitrary as the number of combinations of these two data sources that could combine to produce the [uV]-scaled sources in **x** = **S**(c,t) is infinite.*

That the eye blink artifact data were contained in a single component is not at all surprising. Even though the underlying source model contained two unique dipoles representing the blink artifact generated by each eye, this activity is concurrent and can thus be functionally represented as a single equivalent dipole source that is a linear summation of the two source dipoles. This result is a well-known property of ICA; source activities that are identical and concurrent, like those originating from the simultaneous, functional activity from two structurally independent sources, have only a single, functional representation in source space and cannot be separated. Having determined the blink artifact scalp projection referenced to **blink**(t) in Figure 9, the spatial map in Figure 12 would be expected to have a near-identical, relative spatial distribution if ICA was successfully isolation the equivalent blink source dipole; it is the case that these two topographies are nearly indistinguishable.

The contribution of IC1 can be eliminated from channel space **x** by settings its relative spatial weights in the mixing matrix **A** to 0, which will be represented here as the artifact-free mixing matrix $\widehat{\boldsymbol{A}}$; doing this and then forward-projecting the sources given by $\widehat{\boldsymbol{A}}\boldsymbol{s}$ allows for an artifact-free estimation of the original channel space, $\widehat{\boldsymbol{x}}$. The ICA-corrected channel data are shown in Figure 13.

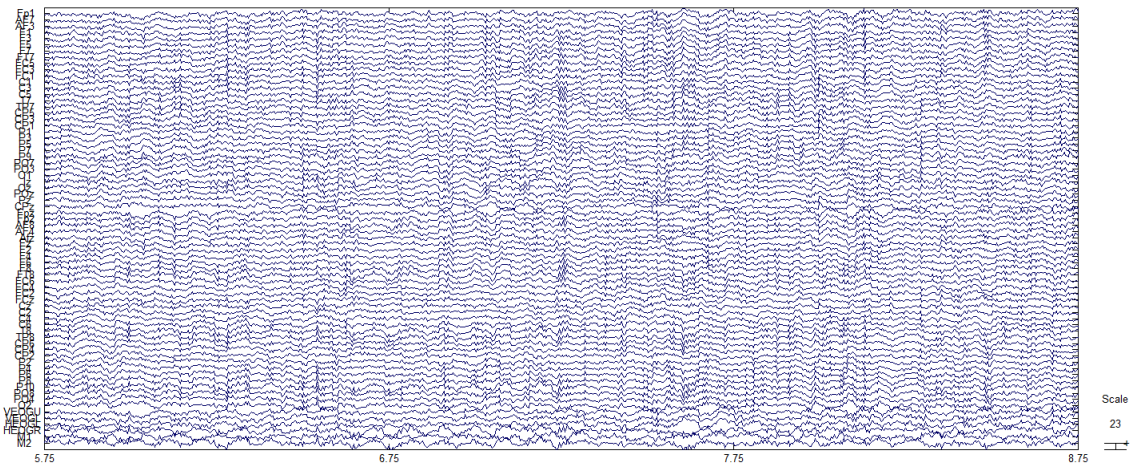

Figure 13. The ICA-reconstructed channel space, $\hat{\boldsymbol{x}}$. Shown along the same 3 [s] window as Figures 10-11, the blink artifact that was previously present at t = 7.25 [s] has been eliminated with very little disturbance to the EEG.

THE MOTIVATING EXAMPLE: AN IDEAL REFERENCE NOISE INPUT

Given that the general goal of this work is to improve the adaptive filtering method for the removal of ocular artifact from the EEG, it would be helpful to have a set of more definitive benchmarks against which to compare new algorithm implementations. To begin, the RLS adaptive filter as implemented by He et al. [12] for a single reference input, r(n) = VEOG, can serve as an estimate for prior art adaptive filtering performance. Extended infomax ICA has already been implemented as a benchmark for a relevant BSS approach; its results are shown in Figure 12 and Figure 13. The most obvious, theoretical improvement that could be made to adaptive filtering would be the availability of a reference noise input, r(n), that is primarily free of the cross-talk, or bidirectional contamination, from EEG sources that results from volume conduction. Using the biophysically-inspired simulated data given by Equation 6, an ideal reference noise input with these properties can be derived from the underlying blink source data, **BLINK**(c,t), that is perfectly representative of the blink artifact and entirely free of contamination from EEG sources. This should provide a theoretical best case for the traditional RLS adaptive filter algorithm implementation. To stay with the realistic practice of using the bipolar VEOG channel as the

reference noise input, the ideal, source noise reference is given by Equation 7, where VEOG(+) and VEOG(-) were indexed in rows 66 and 65, respectively.

$$\mathrm{r(source)} = VEOG(source) = \boldsymbol{BLINK}(VEOG(+), t) - \boldsymbol{BLINK}(VEOG(-), t) \qquad [7]$$

ARTIFACT REMOVAL AND EEG PRESERVATION: T1 and T2

Equally as important to the concept of artifact removal as being able to accurately estimate and correct for artifact sources is the capacity of the algorithm to preserve the true signal when no artifact is present. Analyzing artifact correction algorithm performance in this way has not been adequately addressed in prior art. To improve upon how algorithm performance is measured, a new approach is proposed here.

Given the simulated data model, **S**(c,t), the temporal locations of artifact and non-artifact time periods are well characterized. The only suitable estimate for an algorithm's artifact removal capability is to observe its performance when the artifact is present; this time period, in a generally sense, will be referred to as T1 through the rest of these writings. When the artifact correction algorithm estimates a noise source and removes it from a signal by linear subtraction, the preservation of the underlying signal cannot be differentiated from the accuracy of the noise source estimation during T1. Therefore, a secondary time period, namely when the noise source is known to be inactive, must be used to estimate the algorithm's capability to preserve the true signal in the absence of artifact; let this time period be denoted as T2.

Comparing traditional RLS (r[n] = VEOG), ideal RLS (r[n] = VEOG(source)), and ICA during T1 and T2 should provide insight on the relative performance for each approach prior to proposing any algorithm modifications. To achieve this, a set of time periods T1 and T2 were defined such that T1 encompassed the known blink artifact periods as they were originally simulated with a duration of 0.5 [s], or 128 points in length, centered about the maximal eyelid closure as determined by the blink peak. As a comparable definition for T2, let T2 be an equally-sized window

of 0.5 [s], or 128 data points, centered 1 [s] after the blink apex (that is, the beginning of T2 is equidistant to the end of T1 and the end of T2 with a distance of 0.5 [s], or 128 data points). An illustration of T1 and T2 is shown in Figure 14.

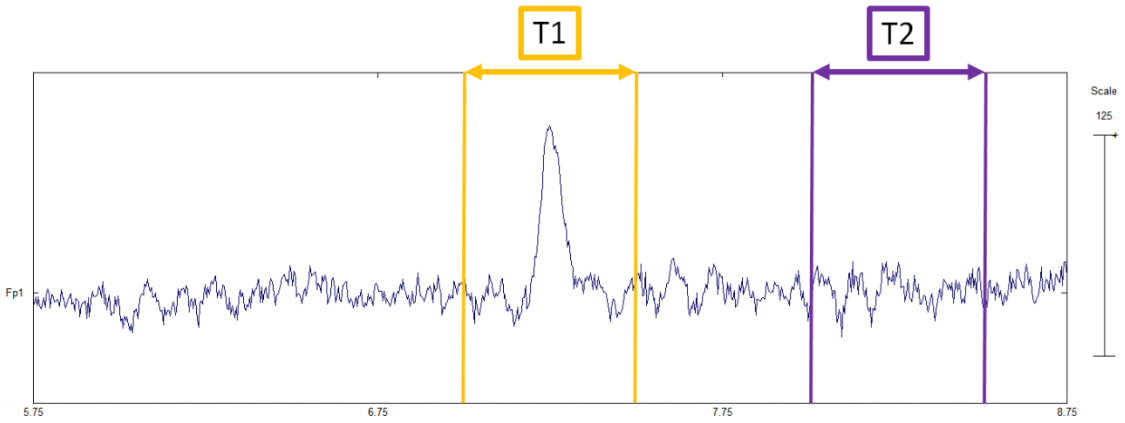

*Figure 14. An illustration of T1 and T2. The beginning of T2, where no blink artifact is present, is equidistant from the end of T1 and the end of T2. The entire activity of the artifact, per the simulation model **S**(c,t), is contained within T1.*

For each of the three benchmark algorithms, their input data sequences and filtered outputs are described in Table . For the purposes of algorithm evaluation, only the filtered output at electrode Fp1, the closest electrode to VEOG(-), is evaluated.

*Table 2. Description of primary input, primary noise reference, and filtered outputs for the benchmark algorithms. Note that ICA, by definition, includes the entirety of the available data matrix, **S**(c,t), as its comparable input data, and the entirety of its forward-projected, artifact-corrected output, $\hat{\boldsymbol{x}}$, as its comparable output data. Only the output channel in $\hat{\boldsymbol{x}}$ corresponding to Fp1, $\hat{\boldsymbol{x}}(Fp1,t)$, is analyzed for the purposes of algorithm evaluation. Note that VEOG(+) and VEOG(-) refer to the positive and negative electrodes, respectively, in the traditional bipolar pair above and below the left eye. The (source) notation indicates that data from the known artifact sources in the simulation are used for computation.*

Algorithm	**Primary Input (s[n])**	**Reference Noise Input (r[n])**	**Filtered Output (e[n])**
RLS	$s(n) = Fp1 = \boldsymbol{S}(Fp1,t)$	$r(n) = VEOG = \boldsymbol{S}(VEOG(+),t) - \boldsymbol{S}(VEOG(-),t)$	$e(\mathrm{n})$
RLS(source)	$s(n) = Fp1 = \boldsymbol{S}(Fp1,t)$	$r(source) = VEOG(source) = \boldsymbol{BLINK}(VEOG(+),t) - \boldsymbol{BLINK}(VEOG(-),t)$	$e(\mathrm{source})$
ICA	$\boldsymbol{S}(c,t)$		$\hat{\boldsymbol{x}}$

To compare the performance of each method, the difference between the filtered output, which should be an estimation of the underlying EEG signal, and the original source EEG at Fp1,

EEG(Fp1,t), is calculated as the error signal for each method. These recovery error vectors, denoted as rev[n], are defined in Table .

Table 3. Definitions of recovery error vectors, rev[n], for each of the benchmark algorithms. Note that indexing vectors 't' (time) and 'n' (point-by-point) have the same length and relative scale, but are represented separately to emphasize that RLS is a point-by-point algorithm.

Algorithm	Recovery Error Vector
RLS	$rev(RLS) = \boldsymbol{EEG}(Fp1, t) - e(n)$
RLS(source)	$rev(RLS(source)) = \boldsymbol{EEG}(Fp1, t) - e(source)$
ICA	$rev(ICA) = \boldsymbol{EEG}(Fp1, t) - \hat{\boldsymbol{x}}(Fp1, t)$

T1 and T2, each of 128 data points (0.5 [s]) in length, can be aggregated across all exemplar data segments from the recovery error vectors to form [60x128] dimensional matrices **T1erv** and **T2erv**. Each algorithm can then be assessed for its accuracy at removing the blink artifacts (T1) and its capacity to preserve the EEG signal when no artifact is present (T2). By expressing **T1erv** and **T2erv** as [60x128] dimensional matrices, EEG recovery error can be evaluated as a mean effect over the segment windows (a [1x128] column vector) or over the blink exemplars (a [60x1] row vector) by calculating RMS error over the columns and rows, respectfully, of the error matrices. Analyzing the error matrices in these complementary ways allows for the investigation of temporal effects over the duration of the blink artifact as well as aggregate performance over all exemplar artifacts for the entire time series.

RMS error vectors as calculated over the columns (temporal average, represented as a time series) and rows (exemplar average, represented as boxplot distributions) and presented as time series data and boxplot distributions, respectively, in each of the panels for the next two figures (Figure 15 and Figure 16). Each figure represents an analysis of both T1 and T2, side-by-side. For both RLS and RLS(source) algorithm implementations, a filter length of M = 3 and a forgetting factor of λ = 0.9999, as suggested by He et al. [12], were used to form the parameters of the filter. Where boxplot distributions are shown, the central (red) mark represents the

median, the edges of the boxes are the 25th (lower) and 75th (upper) percentiles, and the whiskers extend to the most extreme, non-outlier points. Data points are considered to be outliers if they are at an absolute distance of greater than 1.5 times the box height from either the first or third quartile. Notches in the boxplots are set to MATLAB's default to visually estimate the 95% confidence interval about the median.

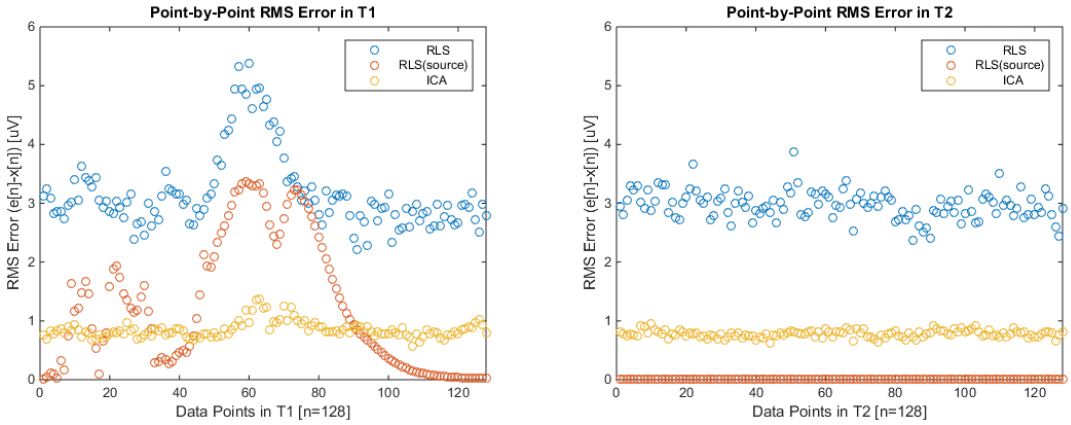

Figure 15. Temporal average RMS error for T1 and T2 for RLS, RLS(source), and ICA.

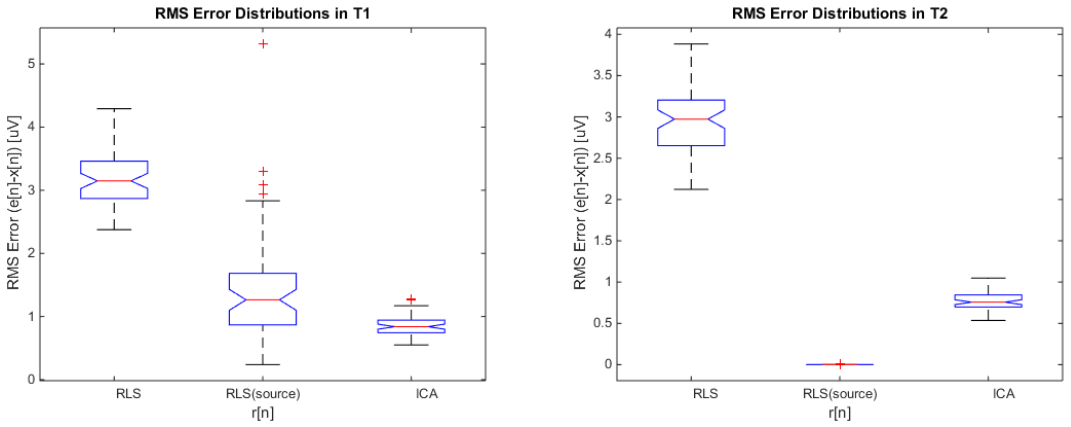

Figure 16. Exemplar RMS error distributions for T1 and T2 for RLS, RLS(source), and ICA.

These results contain a number of interesting findings. These findings are most succinctly presented in list form, following which a discussion of the interests in these results will motivate a proposed series of improvements to the adaptive filtering technique.

- ICA performs quite well, with consistently less than 1 [uV] RMS error, at both removing the blink artifact (T1) and preserving the ongoing EEG (T2) (Figure 15 and Figure 16).

These results will be used to further evaluate success at improving the adaptive filtering method; achieving results as good as, or better, than ICA for an adaptive filtering implementation would be a novel, valuable contribution to the EEG and neuroscience communities.

- RLS, using the traditional VEOG reference noise input with M = 3 and λ = 0.9999 [12], has equally worse performance than ICA in both T1 and T2 (Figure 16). It would appear that the largest errors during T1 come from time points where the blink artifact has a maximal amplitude (Figure 15).
- RLS(source), where the RLS algorithm is provided a practically optimal reference noise input, results in substantially less error than traditional RLS in both T1 and T2 (Figure 16). In fact, the performance of RLS(source) during T2 appears to be substantially better than ICA (Figure 16), resulting in an almost perfect (zero-error) preservation of the EEG signal in the absence of blink artifact. Similarly to RLS, RLS(source) reports maximum error where the blink artifact has maximal amplitude (Figure 15).
- There is a noticeable, characteristic difference between RLS and RLS(source) during T1 that goes beyond overall less error. If the T1 window (Figure 15) is roughly halved, RLS(source) has a smoother error curve during the second half of T1 than the first half; RLS exhibits roughly equal performance in both halves. Given that r(source) is free of cross-talk in both T1 and T2, there are other filtering effects during T1, not attributable to cross-talk that were not originally hypothesized. Additionally, toward the end of T1, the error produced by RLS(source) is actually *less* than the error produced by ICA.

What these results reveal is that **there is great promise in pursuing an improved adaptive filtering method**. When provided with a practically optimal reference noise input that is free of cross-talk, the preservation of the EEG signal during T2 is nearly perfect, and actually results in far

less recovery error than ICA. However, there are oddly noticeable characteristics of the adaptive filter during T1 that suggest room for improvement beyond just reducing cross-talk. This, then, leads to two primary goals for further exploration: **first, the attenuation, or elimination, of cross talk in r[n], and second, investigation the sources of error during T1 that are not purely attributable to cross-talk**.

ADAPTIVE FILTER MAGNITUDE, PHASE, AND GROUP DELAY RESPONSES

To begin to understand why, even with the effect of cross-talk mitigated, RLS(source) behaves unexpectedly during T1, it is easiest to start by visualizing $\hat{r}[n]$, the estimated noise source generated by RLS(source), as compared to $z[n]$, the actual noise source (Equation 3) in Figure 17. Instead of the time widow used in previous data examples, the segment in Figure 17 is the *second* blink in the time series; the first blink is skipped in the visualization in order to give the adaptive filter the opportunity to reach convergence on the first artifact exemplar.

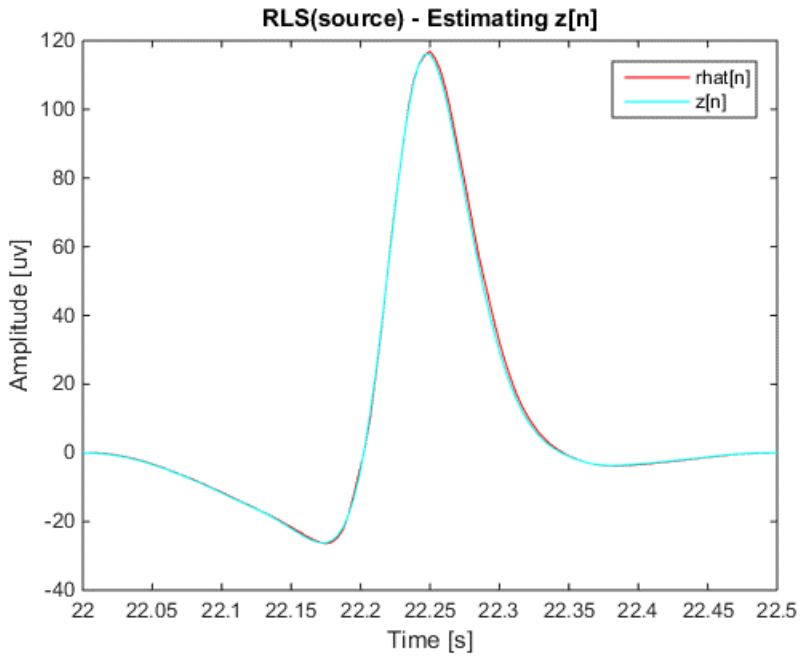

Figure 17. The estimated noise source, $\hat{r}[n]$, generated by RLS(source) as compared to $z[n]$, the actual noise source.

From Figure 17, it would appear that RLS(source) is able to successfully estimate the amplitude of the noise source. However, there appears to be an offset or a misalignment between

$\hat{r}[n]$ and $z[n]$ that is most pronounced toward the end of the blink, almost as if there is a causal delay in the filter response. Since the RLS adaptive filter is, at its root, a finite impulse response (FIR) filter of length M, the filter coefficients as determined by the RLS algorithm, h[m] (Equation 4), can be used to explore the frequency-domain properties of the filter. Since h[m] is updated by the point-by-point recursion algorithm, the change in the properties of h[m] can also be examined over time: more specifically, the properties of h[m] can be examined over the course of the blink artifact in T1 as shown in Figure 17. The magnitude, phase, and group delay responses for h[m] as generated by RLS(source) for the T1 segment shown in Figure 17 are shown in Figure 18. In order to simply the filter response visualization, the magnitude, phase, and group delay responses for h[m] are shown for f = 2.5 [Hz]. Significant power attributable to the blink artifact should be present in the delta band ([0.5 to 3 [Hz]), thus making f = 2.5 [Hz] a meaningful frequency at which to observe the filter response.

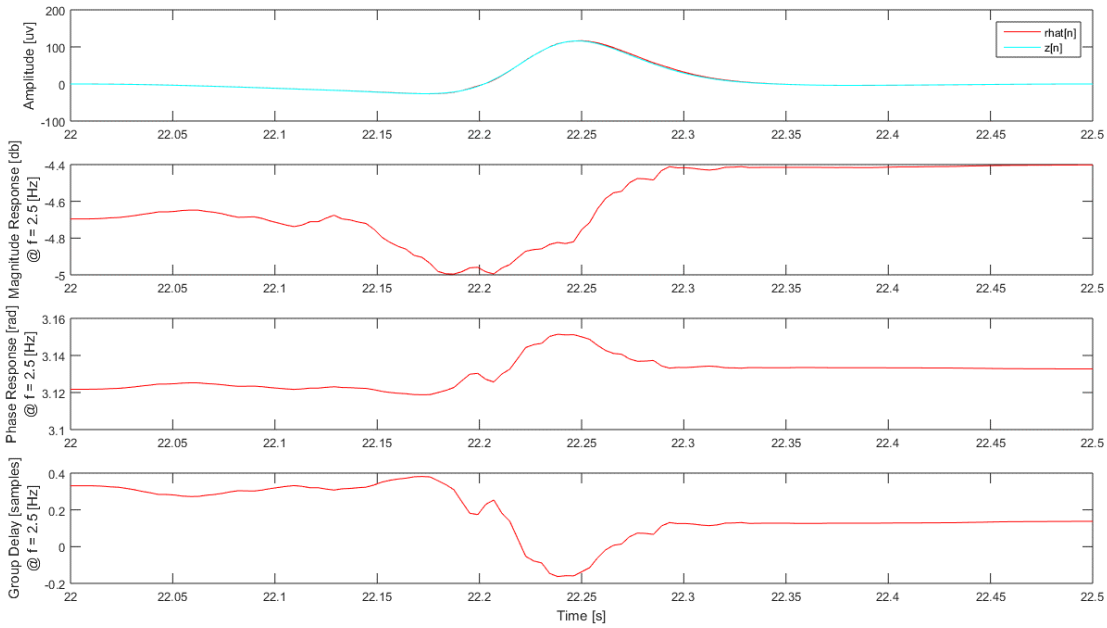

Figure 18. Magnitude, phase, and group delay responses for h[m] during T1. The data shown on the first subplot, $\hat{r}[n]$ and $z[n]$, are identical to that shown in Figure 17.

From Figure 18, the answer to the misalignment is very clear: the non-linear phase of the filter described by h[m] causes a variable, but causal, group delay in $\hat{\boldsymbol{r}}[\boldsymbol{n}]$ that results in its misalignment to $\boldsymbol{z}[\boldsymbol{n}]$. Given the large amplitude and slope that is characteristic of the blink artifact, even a small misalignment, as observed in Figure 17, can result in substantial error when using $\hat{r}[n]$ to estimate $\mathrm{e}[n]$ (Equation 3).

BIDIRECTIONAL CONTAMINATION (CROSS-TALK)

From Figure 15 and Figure 16, the impact of cross-talk is clear, especially for T2. It would appear that reducing cross-talk in the reference noise input also improves the filter error during T1, as well; however, this is now confounded with the non-linear phase and variable group-delay responses that were observed in Figure 16 and Figure 17. In order to fully understand how cross-talk impacts T1, the issue of non-linear phase response of the adaptive filter must first be solved.

LINEAR-PHASE ADAPTIVE FILTERING

In a perfect situation, the adaptive filter could be designed such that a zero-phase filter response is guaranteed. Other than the trivial case where M = 1, a causal, zero-phase filter cannot be realized. There may be some situations such as post-hoc, or offline, analysis where causality does not need to be strictly enforced. Such a case is the MATLAB function 'filtfilt', which filters a signal forward and (non-causally) backward to achieve an equivalent zero-phase filter double the order and having a squared magnitude response of the original. However, there is also the need for the filter to accurately estimate the transfer function between r[n] and z[n] (that is, h[m]). Given that the properties of this transfer function cannot be known *a priori* (and if they were, such knowledge would seemingly obfuscate the need for an adaptive filtering process to begin), it is not possible to relax its form from anything other than that what is empirically determined by the adaptive filtering algorithm (i.e., using 'filtfilt' to allow for non-causality inherently changes the transfer function). If a zero-phase, non-causal filter that correctly estimated the transfer

function between r[n] and z[n] were to be realizable, the loss of causality would still be a significant negative impact.

In situations where the phase response of the filter is an important design criteria, but causality is also required, linear-phase filtering is a preferred solution. Linear-phase FIR filters are a class of FIR filters with coefficient vectors that are either symmetric or antisymmetric and have either even or odd lengths; thus, there are four types of linear-phase FIR filters. Properties of each linear-phase filter type are listed in Table .

Table 4. Properties of linear-phase FIR filters. M, consistent with the rest of this text, is defined as the filter length; filter order is then given by M-1. Linear-phase FIR filters all exhibit the same, constant group delay that is a function of its filter order, α=(M-1)/2.

Type	**Length (Order)**	**Coefficient Form m:{1:M}**	**Linear Phase Response** $\boldsymbol{\theta(\omega) = -\alpha\omega + \beta}$	**Group Delay**
Type I	Odd (Even)	h[m] = h[M+1-m] (symmetric)	$\alpha = \frac{M-1}{2}$ $\beta: \{0, \pi\}$	α
Type II	Even (Odd)	h[m] = h[M+1-m] (symmetric)	$\alpha = \frac{M-1}{2}$ $\beta: \{0, \pi\}$	α
Type III	Odd (Even)	h[m] = - h[M+1-m], h[(M+1)/2] = 0 (antisymmetric)	$\alpha = \frac{M-1}{2}$ $\beta: \left\{\frac{\pi}{2}, \frac{3\pi}{2}\right\}$	α
Type IV	Even (Odd)	h[m] = - h[M+1-m] (antisymmetric)	$\alpha = \frac{M-1}{2}$ $\beta: \left\{\frac{\pi}{2}, \frac{3\pi}{2}\right\}$	α

The primary benefit to linear-phase FIR filters is that they all share the same constant group delay, α, that is purely a function of the filter length, M, given by α = (M-1)/2. As such, all linear-phase FIR filters have a constant, and predictable, group delay such that the filter output can be phase-aligned to the primary input of the filter by delaying the primary input by α samples. This makes phase alignment for the output of linear-phase FIR filters very simple to achieve as long as the primary input delay is tolerable given any particular application.

LINEAR-PHASE RECURSIVE LEAST SQUARES

Given the need to consider phase alignment in the adaptive noise cancellation problem, and that linear-phase FIR filters are a suitable choice for doing so, the logical solution would be to investigate linear-phase constraints for the RLS algorithm. Fortunately, algorithms for phase re-alignment in general adaptive filtering applications have been studied [86]. Pseudocode for implementing the Type I, linear-phase FIR, RLS adaptive noise-cancelling filter (lpRLS) is given in Figure 19; its block diagram is shown in Figure 20. Note that some of the variable names from Friedlander & Morf's original derivations [86] have been changed to better match the general RLS equations given here (Equations 3 and 4). An example result of the improve alignment that can be achieved with lpRLS is shown in Figure 21. For the clarity of the figure, the time scale has been narrowed to a small window surrounding the eye opening phase of the blink. While the improvement may seem marginal at best, the data pointers shown in Figure 21 demonstrate that even single data point of misalignment between r[n] and z[n] could result in an error as large as 10 [uV] in e[n]. Given that EEG is expected to be no larger in amplitude than 50 [uV] peak-to-peak, a 10 [uV] error is of substantial size. In the pseudocode in Figure 19, and also in the original derivation by Friedlander and Morf [86], a matrix inverse operation is required to update P(N+1); the consequences of this are discussed in detail in.

```
%% Input Variables
s = s;              % s[n], Primary Input
r = r;              % r[n], Reference Noise Input
M = 3;              % Filter Length (Must Be Odd, Type-I FIR)
Lambda = 0.9999;    % Recommended by He et al. (2007)

%% Output Variables
e = zeros(1,N);     % e[n], Estimated Noise-Free Signal

%% Local Variables
N = length(s);      % Number of Discrete Data Points in Time Series s[n]
d = (M-1)/2;        % d = Filter Group Delay (Linear-Phase FIR)
sigma = 0.01;       % 'sigma' Should be Small if Variance of s[n] Is Unknown
                    % (Friedlander & Morf, 1982)
h = zeros(M,1);     % h[m], Linear-Phase FIR Filter
rhat = zeros(1,N); % Estimated Noise, rhat[n]
P = eye(M)./sigma; % Initialize 'P0' for Recursion

%% Execute the Recursive (Point-by-Point) Algorithm
for n = M:N
    % Update Current Values of 'rp' and 'sbar'
    r_n = r((n-M+1):1:n); % Current Window of r[n]
    rp = [r_n(end:-1:1); r_n]'; %
    sbar = [1;1]*s(n-d);
    % Update P(N+1)
    P = (P - ((P*rp)*inv((Lambda*eye(2))+(rp'*P*rp))*rp'*P))./Lambda;
    % Update K(N+1)
    K  = P*rp;
    % Update h(N+1)
    h = h + K*(sbar - (rp'*h));
    % Apply Updated Linear Phase RLS-AF to r[n]
    rhat(n) = r_n(end:-1:1)*h;
    % Account For Delay, Find e(n-d) With Delayed s(n-d)
    e(n-d) = s(n-d) - rhat(n);
end
```

Figure 19. Pseudocode for the Type I, linear-phase FIR, RLS adaptive noise canceller. This algorithm was adapted from the recursive implementation of the least-squares adaptive linear-phase filtering algorithms given by Friedlander & Morf (1982). A brief discussion of the matrix inverse required to update P(N+1) is provided in Appendix B.

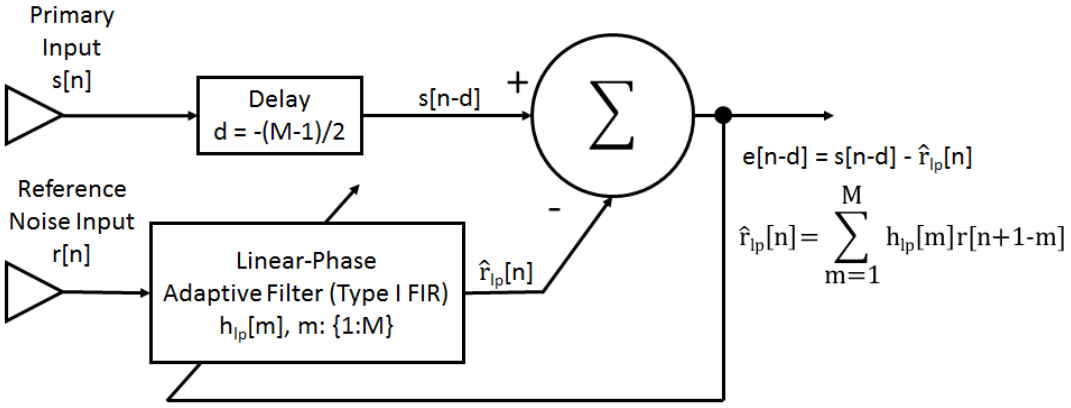

Figure 20. Block diagram for the lpRLS algorithm. In addition to the Type I FIR constraint on $h_{lp}[m]$, the primary input, s[n], is delayed to account for the constant group delay caused by the filter. The resulting output, e[n-d], is then appropriately phase-aligned with s[n].

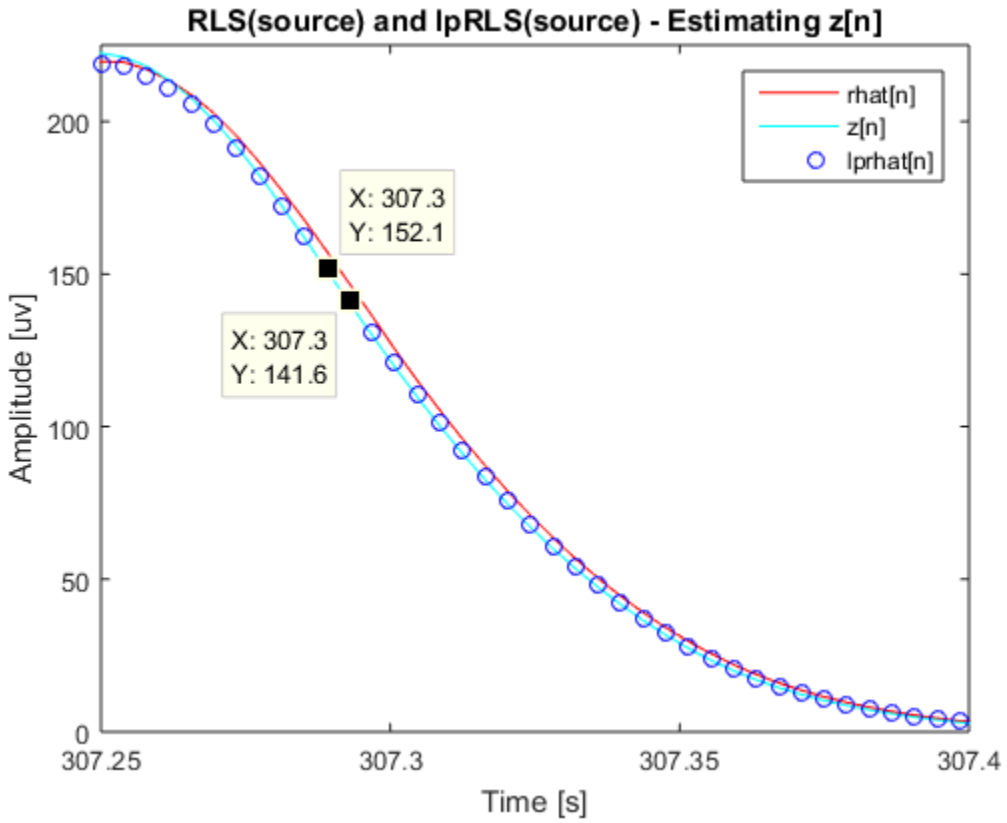

Figure 21. An example of phase alignment improvement in estimating z[n] using lpRLS. Even with a narrow time window, the improvement due to lpRLS (lprhat[n]) over traditional RLS (rhat[n]) may seem marginal, at best. However, in this phase of the blink, a single data point of misalignment as shown in this figure using data pointers could lead to an error as large as 10 [uV] in the final estimate e[n]. Given that EEG is expected to be less than 50 [uV] peak-to-peak, a 10 [uV] error is substantial.

Practically, there is no reason to evaluate traditional RLS implementations in this work any further unless considered as a basis for comparison to other methodologies. A phase-aligned filter output will always be preferred to being out-of-phase due to a variable group delay; the result shown in Figure 21 confirms that lpRLS solves the non-linear phase, or variable group delay, problem with traditional RLS. As a result, any further evaluation of improvements to the adaptive filtering algorithm will be examined for lpRLS only.

REDUCING CROSS-TALK

Efforts to reduce cross-talk in the reference noise input to the adaptive filter have not been prominently investigated in recent literature. As demonstrated in Figure 15 and Figure 16 using a practically ideal source reference noise input, the ability to do so could put adaptive filtering on par with, or even ahead of, the success of BSS algorithms for ocular source separation. Two studies mentioned earlier [79] [81] fused adaptive filtering approaches with BSS as a secondary stage. Reduced cross-talk in the noise reference input that could be achieved with other methods may be more practical for use in many situations such as reliable, automated correction and on-line, or real-time, systems.

LOWPASS FILTERING

Romero, Mañanas, and Barbanoj [72] tested the efficacy of low-pass filtering the reference noise input prior to adaptive filtering as a means for reducing EEG cross-talk. They chose a low-pass cutoff frequency of 7.5 [Hz], although further specification of filter form or other parameters were not provided. Unsurprisingly, applying the low-pass filter did not improve the error found in accurately recovering band power measures for frequencies in the passband (below 7.5 [Hz]), and improvement elsewhere was mixed depending on the outcome measures analyzed. This result is commensurate with the theory that the low-pass filter would have reduced EEG cross-talk for frequencies in the stopband while leaving frequencies in the passband unaffected.

In this work, low-pass filtering is again investigated as a possible approach for reducing cross-talk. As opposed to choosing only a single cutoff frequency, several frequencies over the range of relevant frequency content (and possibly slightly beyond) found in EEG (5, 7.5, 10, 15, 20, 25, 30, 35, 40, and 45 [Hz]) were simulated.

The specific filter form used here is the Butterworth filter [87]. The Butterworth infinite impulse response (IIR) filter was chosen for its flat passband and ease of design (using the MATLAB (R2014b) 'butter' function, only a filter order and cutoff frequency need be specified). All low-pass Butterworth filters were fourth order. In order to avoid any potential phase misalignment, the MATLAB (R2014b) function 'filtfilt' was used to resolve a non-causal, zero-phase implementation of each filter design (with, as mentioned previously, a double filter order and squared magnitude response in comparison to the originally-designed filters).

SMOOTHING SPLINES

If the ultimate goal of conditioning the reference noise input is such that the blink information is preserved and the EEG cross-talk is attenuated or eliminated, the use of smoothing splines may be a beneficial. The goal of any smoothing spline algorithm is to fit a piecewise polynomial function to a time series such that noise, of high-frequency characteristics, are eliminated from the signal by the smooth polynomial fit. There are many choices for estimating a smoothing spline for a given curve. Lacking an *a priori* preference for a general smoothing spline implementation, the general smoothing spline functionality in MATLAB's (R2014b) Curve Fitting Toolbox, the 'csaps' function, was used to calculate a variety of smoothing splines over a range of smoothing parameters, denoted by p. The smoothing parameter can be thought of a value by which the algorithm determines how smooth of a fit over noise will be achieved weighed against a potential reduction in the goodness of the overall fit itself. For example, p = 0 produces straight line of least-squares fit through the data; this fit is very smooth, but the goodness of the fit is likely

to be very poor. Conversely, p = 1 produces a perfect cubic spline interpolant of the data; as it fits the data on the lowest dimensionality possible, point-by-point, the goodness of the fit is quite high, but there is no smoothing achieved because the piece-wise fit of the splines contain the exact data points of the original curve as their endpoints. While there are some approximations for determining initial values of p that may be suitable, these were not used here; instead, the smoothing parameter was adjusted over a range of values until the fit of the blinks became very poor as p approached 0, or until the goodness of fit was sufficiently high as to prevent any smoothing of the EEG cross-talk artifact as p approached 1.

BAYESIAN ADAPTIVE REGRESSION SPLINES

A specific smoothing spline implementation that was suggested by Wallstrom et al. [70] for ocular artifact removal using a regression approach is the Bayesian adaptive regression splines, or BARS, algorithm [71]. This technique, sometimes referred to as free-knot splines (as by DiMatteo, Kenovese, and Kass [71]), allows the knots, or endpoints, of the splines to be adjusted in quantity and location. The notional concept is that a waveform may be better smoothed, while still preserving signal characteristics of interest, if knots are placed at optimal locations in the time series. The interpretation of this provided by Wallstrom et al. [70] as it relates to the VEOG reference noise input is that allowing the knots to be dynamically adjusted and concentrated around the blink artifact itself should result in a better goodness of fit of the blink without the cost of a loss of smoothness during non-blink, or primarily EEG cross-talk dominated, areas of interest. In comparison to the general smoothing spline approach described above, the BARS algorithm should allow for simultaneous preservation of the blink and smoothing of the EEG cross-talk, which is the goal of searching for a better-conditioned reference noise input signal for the adaptive filter.

NON-LOCAL MEANS

The final method proposed for this work in an effort to reduce cross-talk in the reference noise input is Nonlocal Means, or NLM, filtering [88] [89]. The NLM algorithm was originally designed for edge preservation in image data, but it has found a number of uses in biomedical processing (e.g. [90]), and particularly for medical image processing (e.g. [91] [92]). The approach of NLM is to look for a set of signal observations given the presence of additive noise that may obscure the signal. These observations, ideally, would have similar temporal structure. The search for these observations is accomplished by defining a representative patch size, or a segment of the one-dimensional signal of some length, and then compare every patch in the signal to every other patch in the signal as a point-by-point, fully exhaustive operation. The patches are always averaged together by a weighted process such that a patch containing a morphology that is characteristically represented in many other patches is weighted heavily (or, preserved in the mean amongst many observations). The weighted average is the 'Means' part of NLM; the 'Nonlocal' part is derived from the notion that the distance between similar patches has no bearing on the weight applied to it in the mean such that the entirety of the available dataset can be used to search for similar patches without penalty other than computational expense. Given a sample, s of time series, v, the estimate of de-noised signal, $\hat{u}(s)$, is given by Equation 8, and the weighting function, $w(s,t)$, is given by Equation 9.

$$\hat{u}(s) = \frac{1}{\sum_t w(s,t)} \sum\nolimits_{t \in N(s)} w(s,t) v(t) \qquad [8]$$

$$w(s,t) = exp\left(- \frac{\sum_{\delta \in \Delta} \big(v(s+\delta) - v(t+\delta) \big)^2}{2 L_\Delta \lambda^2} \right) \qquad [9]$$

NLM requires very few algorithm parameter definitions; only the patch size, P (per Equation 9, $L_\Delta = 2P + 1$, where Δ is a local patch surrounding s), and bandwidth parameter, λ, that is a function of the estimated noise standard deviation, σ (λ = 0.5σ), are necessary to be

explicitly determined. As noted by Tracey & Miller [90], a reasonable choice of patch size should approximate the characteristic duration of the signal observation. The comparison patch is also a sample within v, centered on t, that is of length L_Δ. Equation 8, then, is calculated at all comparison points t within the sample s ($t \in N(s)$). For preserving the QRS complex in noisy data, they recommend a patch size equal to the Q-R interval. To reduce the overall computational requirement of the exhaustive search, the neighborhood, or the area over which a patch may search against other patches, may be reduced from the entirety of the available signal (fully non-local) to a subsection, or subsections, of the entirety (partially non-local). For electrophysiological signatures such as the QRS complex that are highly stereotyped (for healthy cardiac function) and appear regularly and frequently in the ECG, a significantly reduced neighborhood search over a minute of data, or less, may be expected to perform quite well.

The application of NLM to conditioning the reference noise input to the adaptive filter would be to search for characteristic observations of the blink artifact as the signal while, presumably, the EEG cross-talk would average out to approximately 0 [uV] due to low weighting in comparison. A patch size that would adequately capture the characteristic blink would likely be on the order of 100 to 200 [ms] to match up with the expected mean blink duration [85]. The standard deviation of the estimated noise, or in this case, the EEG cross-talk, was calculated as 5 [uV] from the simulated data presented here (using [**EEG**(VEOG(+),t)-**EEG**(VEOG(-),t)] to estimate σ). The NLM filter can thus be applied to the reference noise input in varying patch sizes, σ = 5 [uV], and the performance of the adaptive filter can be observed in relation. Practically speaking, the search neighborhood need not be the entire 15 [min] of simulated data, but a post-hoc analysis such as this can accommodate the fully exhaustive search.

SIMULATION APPROACH

Given the available methods presented here, the strategy for algorithm evaluation is to first compare individual parameters of a particular approach (low-pass filtering, smoothing splines, BARS, and NLM) as applied to the traditional reference noise input, r[n] = VEOG, and examine its performance relative to r[n] = VEOG and r[n] = r(source). This comparison will be done for both T1 and T2 as estimates of artifact removal and signal preservation, respectively. The lpRLS algorithm will always be used in lieu of the traditional RLS algorithm; from a theoretical and practical perspective, the correctly-aligned phase between r[n] and s[n] should always produce less signal recovery error than introducing non-linear phase shifts into the processing pipeline. All of this will be accomplished using the biophysically-inspired, source-generated dataset.

After evaluating the best of each reference noise input conditioning approach, the most suitable result from each approach can be compared to each other as well as to ICA, which will be the gold standard measure of performance for this analysis.

III. RESULTS

LINEAR-PHASE ADAPTIVE FILTERING

Although the biophysics of volume conduction and the structural and functional assumptions assumed to the simulated data in this work present a strong theoretical argument that linear-phase filtering should be superior to allowing the RLS adaptive filter to generate a non-linear phase response, it is still useful to compare the two algorithms at the level of the empirical results they generate. From Figure 15 and Figure 16, it was discovered that the phase non-linearity was only observable during T1 when r[n] = r(source) was used as the reference noise input. Therefore, RLS and lpRLS were examined using r(source) as the reference noise input in order to further quantify the improvement achieved by restricting the adaptive filter response to Type I FIR. Figure 22 and Figure 23 show the same analysis as Figures 15 and 16, namely performance of the adaptive filters as both temporal and exemplar aggregates. For the purposes of consistency in comparison, ICA is also included. Since there was only a single ICA decomposition performed on the simulated dataset **S**(c,t), the ICA results presented in these figures, as well as all others, do not change; this allows the evaluation of every modification to the adaptive filtering algorithm to be compared against that which is considered to be the benchmark.

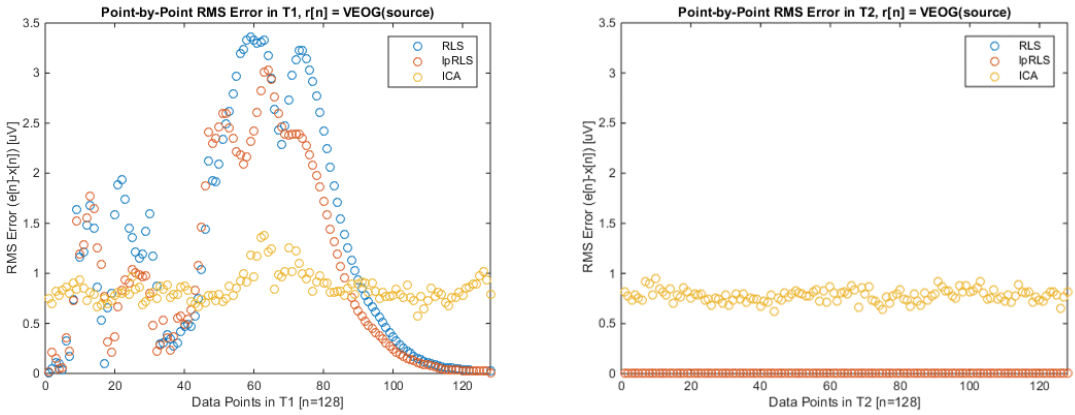

Figure 22. Temporal average RMS error for T1 and T2 for RLS and lpRLS using r[n] = r(source). ICA results are also shown for the purposes of benchmark comparison.

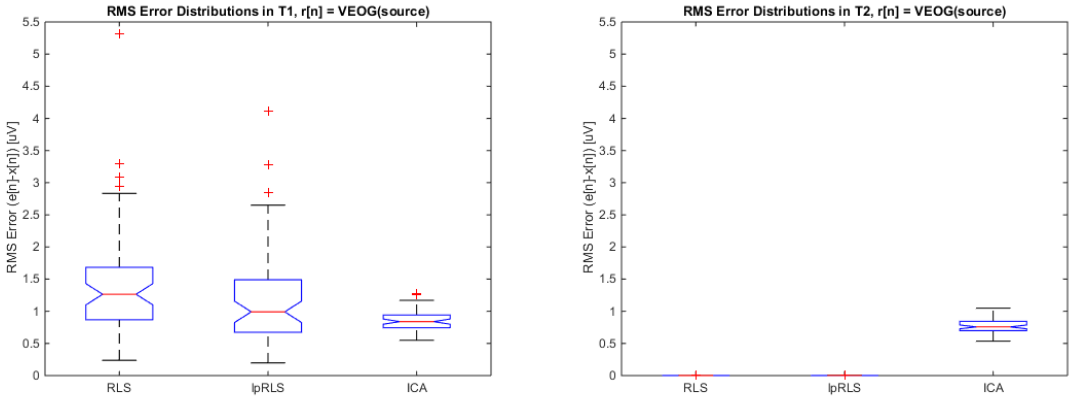

Figure 23. Exemplar RMS error distributions for T1 and T2 for RLS and lpRLS using r[n] = r(source). ICA results are also shown for the purposes of benchmark comparison.

Visual interpretation of these results would appear to confirm that, indeed, lpRLS solves the phase misalignment issues of the prior art RLS algorithm and is able to reduce the mean error in EEG signal recovery during T1. Results during T2 are convincingly identical to one another, with both producing a near-perfect signal recovery that exceeds the performance of ICA; from a practical perspective, further comparison of T2 for these results isn't necessary. There are, however, two outstanding concerns with these results. First, the improvement appears to be only during approximately the second half of the blink artifact window (T1). Second, more quantitative evidence beyond subjective, visual inspection would be desirable in order to better understand the contribution of the linear-phase filter to the reduced error.

To better understand why the performance of lpRLS seems to differ between the first and second halves of T1, the magnitude, phase, and group delay responses of the lpRLS adaptive filter are shown in Figure 24. Similarly to Figure 18, the filter response is observed at f = 2.5 [Hz] to simplify the visualization. The actual blink noise source as determined by the simulated data model, z[n], is also plotted along with the estimated noise sources as determined by the RLS (rhat[n]) and lpRLS (lprhat[n]) algorithms. For each of the magnitude, phase, and group delay responses, both RLS and lpRLS filters are shown.

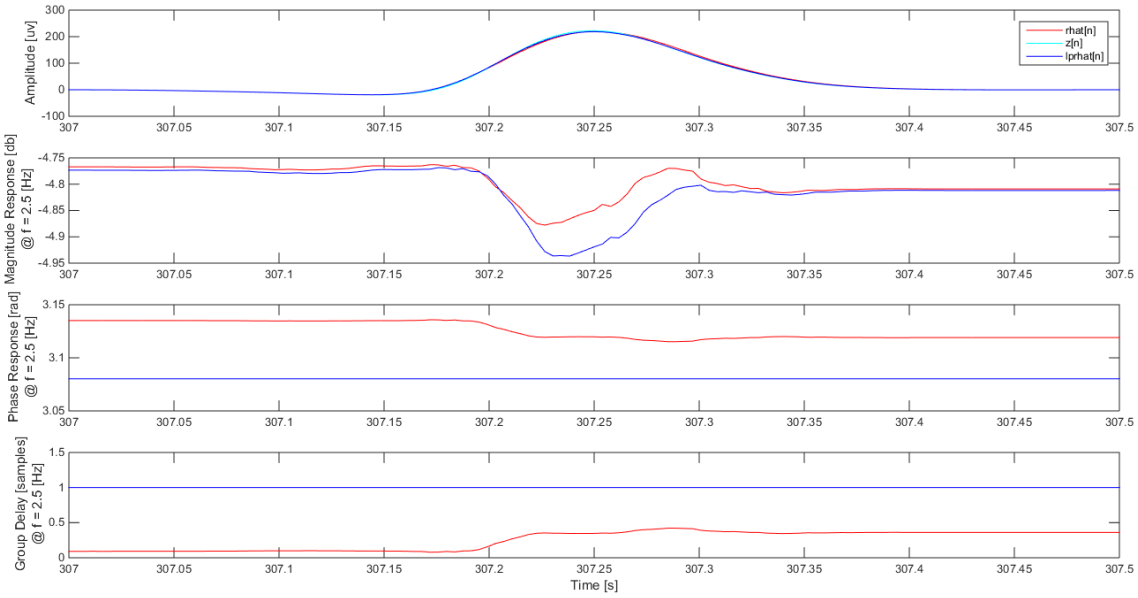

Figure 24. Magnitude, phase, and group delay responses for h[m] and h_{lp}[m] during T1 using RLS and lpRLS, respectively. The reference noise input for both algorithms was r[n] = r(source). The data shown on the first subplot, $\hat{r}[n]$, $z[n]$, and $\hat{r}_{lp}[n]$ are from the same blink artifact segment shown in Figure 21.

As expected, Figure 24 shows a constant phase response for f = 2.5 [Hz] as well as a constant group delay (d = 1 for M = 3). Even though the lpRLS algorithm generates a filter, h_{lp}[m], that is linear-phase, there is still a variability that exists in the filter's magnitude response during the blink artifact. This variability appears in h[m], the filter generated by the RLS algorithm, as well. It would therefore appear that the variable magnitude response is not related to filter implementation, but to the *adaptive* property of the adaptive filter itself. As the filter encounters the blink, it will adjust its coefficients to solve the minimization function that defines the adaptive

filter [11]. This adjustment period, as shown in Figure 24, does eventually stabilize toward the end of the blink. If the magnitude response variability is a property of the adaptive filter itself, then the linear-phase implementation may not beneficially affect the phase alignment of $\hat{r}_{lp}[n]$ until the filter response begins to stabilize. To further probe this theory, T1 was split into two halves that were then analyzed independently. The T1 split-half analysis is shown in Figure 25 and Figure 26.

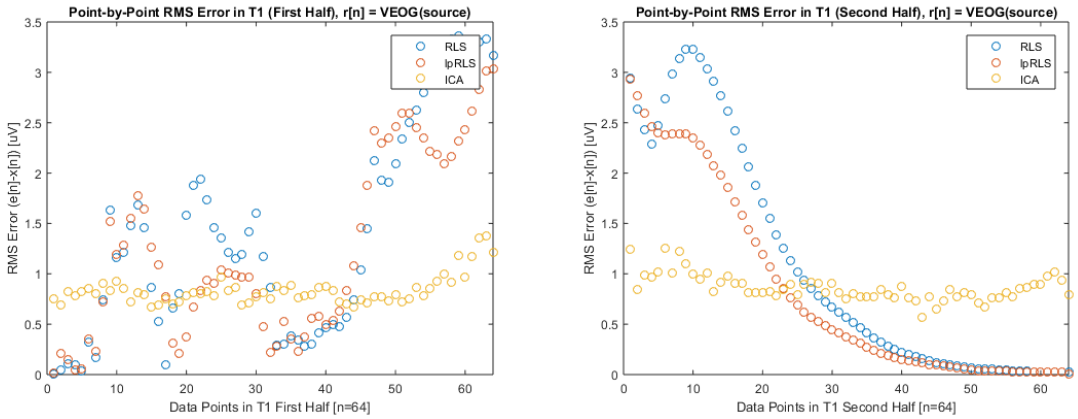

Figure 25. Temporal average RMS error for T1 First Half and T1 Second Half for RLS and lpRLS using r[n] = r(source). ICA results are also shown for the purposes of benchmark comparison.

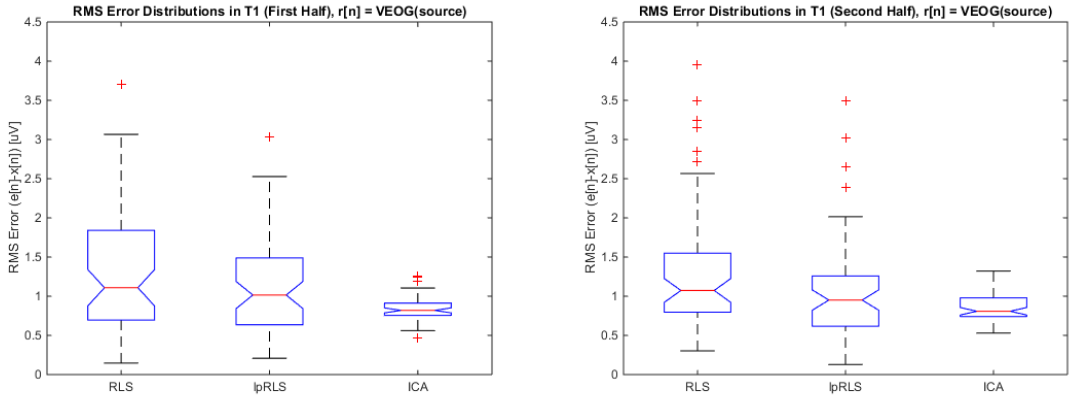

Figure 26. Exemplar RMS error distributions for T1 First Half and T1 Second Half for RLS and lpRLS using r[n] = r(source). ICA results are also shown for the purposes of benchmark comparison.

Having separated the halves of T1 to examine the effect of filter convergence, a test for significant effects of artifact correction algorithm was performed using a one-way ANOVA[3]. For T1 First Half, the effect of algorithm was significant, $F_{(22,179)} = 7.2357$, $p < 0.001$, $\eta_p^2 = 0.0756$. Following the significant main effect of algorithm, post-hoc, pairwise comparisons using MATLAB's 'multcompare' function were performed to examine the main effect. All post-hoc, pairwise comparisons for these tests, as well as all others presented elsewhere in this work, were corrected for multiple comparisons using Tukey's Honestly Significant Difference (HSD). Both RLS ($p < 0.001$) and lpRLS ($p = 0.03$) were significantly different than ICA, but not significantly different from each other (0 = 0.4447). The same analysis was also performed for T2 Second Half. Again, the main effect of algorithm was significant, $F_{(22,179)} = 8.7713$, $p < 0.001$, $\eta_p^2 = 0.0902$. Both lpRLS ($p = 0.46$) and ICA ($p < 0.001$) were significantly different than RLS, but not significantly different from each other ($p = 0.17$). These results can be visualized in Figure 27; additional information for the post-hoc, pairwise comparisons is given in Table . These results can be summarized by noting that lpRLS did not produce significantly lower error than RLS until the second half of T1; however, when the error for lpRLS was significantly lower than RLS, it was not significantly different from ICA. Thus, there is still some appreciable amount of error due to filter convergence, but once the filter has approximately converged, lpRLS can achieve the same, low overall error as ICA during T1. While not for discussion here, the effect of filter convergence in the context of adaptive filtering will be explored later in this work by comparing results of the recursive algorithms to

[3] One-way ANOVAs were used in lieu of two-way ANOVAs with segment as a factor (levels of T1 First Half and T1 Second Half). Significant interactions (or lack thereof) between algorithm and segment may or may not be interesting to formally examine, but they are not the focus of the work presented here. As with significant main effects and post-hoc, pairwise differences, significant interactions between segment and factor can be estimated by the data presented in the exemplar RMS error boxplots for each test. An example of how one might perform such an estimation is given in Appendix C.

those that result in a single set of optimal filter coefficients (in the least-squares sense as applied to the energy minimization criteria of the adaptive filter) for an entire time series.

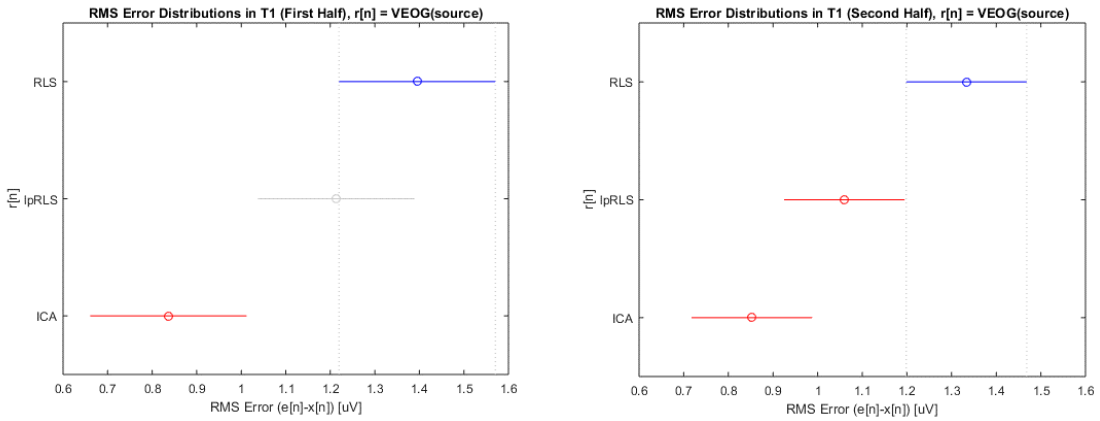

Figure 27. Post-hoc, pairwise comparisons for T1 First Half and T2 Second Half for RLS and lpRLS using r[n] = r(source). ICA results are also shown for the purposes of benchmark comparison.

Table 5. Post-hoc, pairwise comparisons for T1 First Half and T1 Second Half comparing RLS to lpRLS. Comparisons resulting in significant differences ($\rho < 0.05$) are highlighted in orange.

Segment	Paired Comparison	μ	95% CI	p-value
T1 First Half	RLS, lpRLS	0.1819	[-0.1692, 0.5330]	0.4447
T1 First Half	RLS, ICA	0.5586	[0.2075, 0.9097]	0.0006
T1 First Half	lpRLS, ICA	0.3767	[0.0257, 0.7278]	0.0319
T1 Second Half	RLS, lpRLS	0.2737	[0.0038, 0.5436]	0.0460
T1 Second Half	RLS, ICA	0.4808	[0.2109, 0.7507	0.0001
T1 Second Half	lpRLS, ICA	0.2071	[-0.0628. 0.8526]	0.1700

REDUCING CROSS-TALK

As with the analysis performed for the effect of algorithm (RLS, lpRLS, and ICA) on the error in EEG signal recovery, comparable analyses can be performed to examine the effects on recovery error for each of the proposed algorithms to reduce cross-talk, or bidirectional contamination, from the reference noise input. All of these algorithms were applied to the

reference noise input and then used in conjunction with lpRLS to test overall error in the adaptive filter system. Having clearly theorized and empirically demonstrated that lpRLS produces either the same (T1 First Half, T2) or less (T1 Second Half) error than RLS, there is no justifiable reason to include RLS in any further analyses. One-way ANOVAs were used to examine the effect of each algorithm; where necessary for significant differences in the one-way tests, post-hoc, pairwise comparisons, corrected for multiple comparisons using Tukey's HSD, were performed to further detail the sources of the significant main effect. While each algorithm is first analyzed independently, the best-performing set of parameters from each is selected for an omnibus comparison that includes ICA. Each algorithm is also compared to r[n] = VEOG and r[n] = r(source) to more directly observe the reduction in cross-talk.

LOW-PASS FILTERING

Low-pass filters consisted of fourth-order Butterworth filters with cutoff frequencies at 5, 7.5, 10, 15, 20, 25, 30, 35, 40, and 45 [Hz]. These frequencies were chosen to represent a range of salient frequencies contained within EEG, although some studies have provided evidence that scalp frequencies above 20 [Hz] are of myogenic, and not cortical, origin [93]. The results for low-pass filtering the reference noise input are shown in Figure 28 (temporal aggregate), Figure 29 (exemplar boxplots), and Figure 30 (post-hoc, pairwise multiple comparisons). Because of the number of post-hoc, pairwise comparisons, the full table can be found in Appendix D.

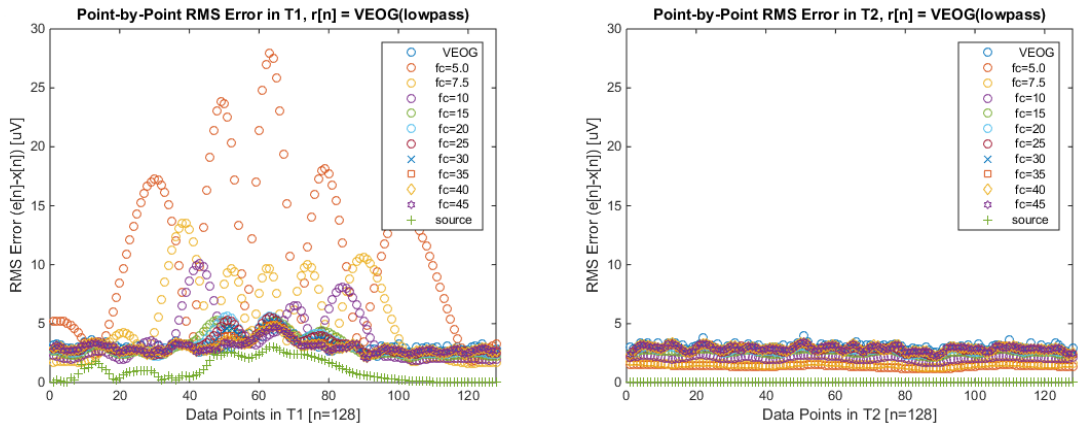

Figure 28. Temporal average RMS error for T1 and T2 using lpRLS and r[n] = r(lowpass). Results for r[n] = VEOG and r[n] = r(source) are also shown for comparison.

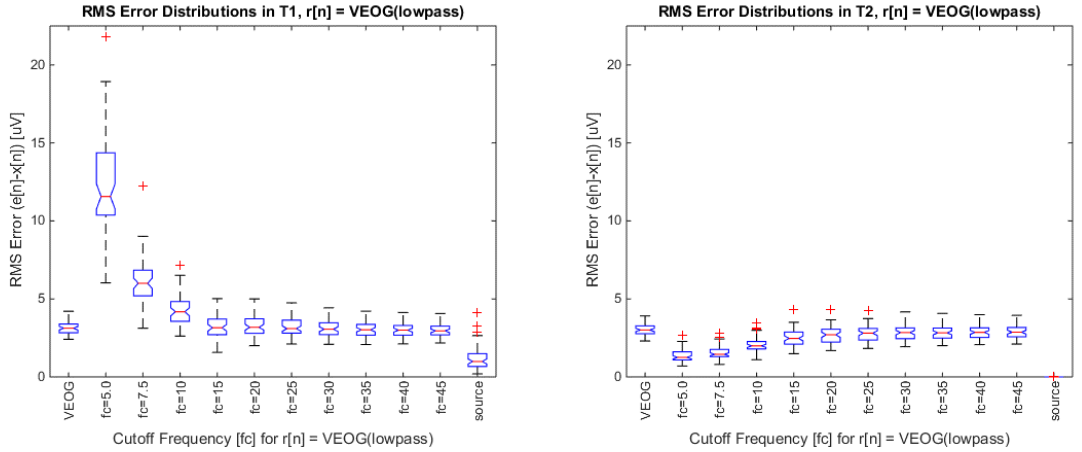

Figure 29. Exemplar RMS error distributions for T1 and T2 using lpRLS and r[n] = r(lowpass). Results for r[n] = VEOG and r[n] = r(source) are also shown for comparison.

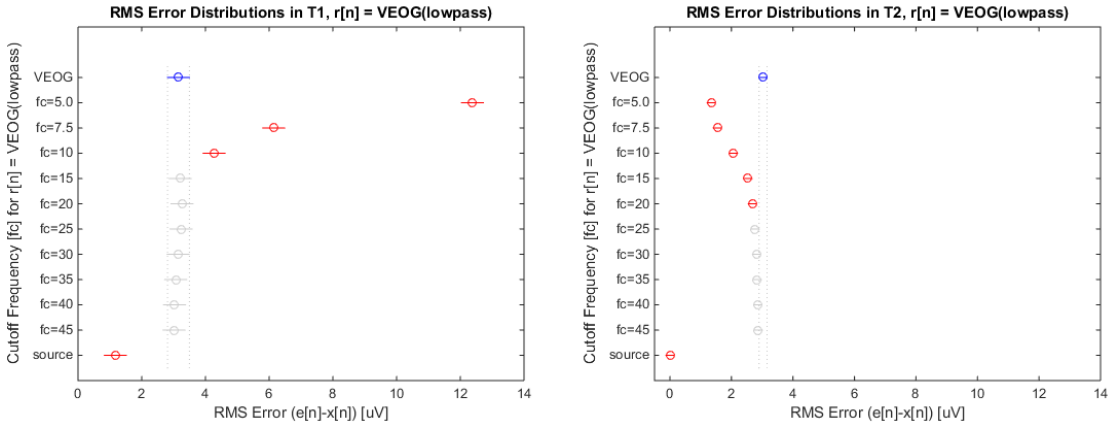

Figure 30. Post-hoc, pairwise comparisons for T1 and T2 using lpRLS and r[n] = r(lowpass). Results for r[n] = VEOG and r[n] = r(source) are also shown for comparison.

The one-way ANOVA for cutoff frequency of the low-pass filter had a significant main effect, $F_{(11,719)} = 364.9429$, $p < 0.001$, $\eta_p^2 = 0.85$, for T1. General trends in the post-hoc, pairwise comparisons revealed that no cutoff frequency for r[n] = VEOG(lowpass) achieved an error of less than r[n] = VEOG, let alone approached the error achieved with r[n] = r(source); further, cutoff frequencies for r[n] = VEOG(lowpass) at 10 [Hz] and below significantly increased the error in comparison with r[n] = VEOG. For T2, the one-way ANOVA for cutoff frequency of the low-pass filter also had a significant main effect, $F_{(11,719)} = 253.3754$, $p < 0.001$, $\eta_p^2 = 0.80$. To summarize the post-hoc, pairwise comparison tests, cutoff frequencies for r[n] = VEOG(lowpass) at or below 20 [Hz] improved the error as compared to r[n] = VEOG; cutoff frequencies for r[n] = VEOG(lowpass) at or above 25 [Hz] were not significantly different than for r[n] = VEOG. The lowest error that was produced for r[n] = VEOG(lowpass) at a cutoff frequency of 5 [Hz] produced an error well above (significantly greater) than for r[n] = r(source).

SMOOTHING SPLINES

Smoothing splines were calculated over r[n] = VEOG using smoothing parameter (p) values of 0.99985, 0.9994, 0.9998, 0.99999, 0.99999999, and 0.999999999. These smoothing parameters were chosen based on empirical testing against the desire to smooth the non-artifact segments (T2) as much as possible while trying to minimize degradation to the blink signature (T1). The results for using the generated smoothing splines for the given smoothing parameters are shown in Figure 31 (temporal aggregate), Figure 32 (exemplar boxplots), and Figure 33 (post-hoc, pairwise multiple comparisons).

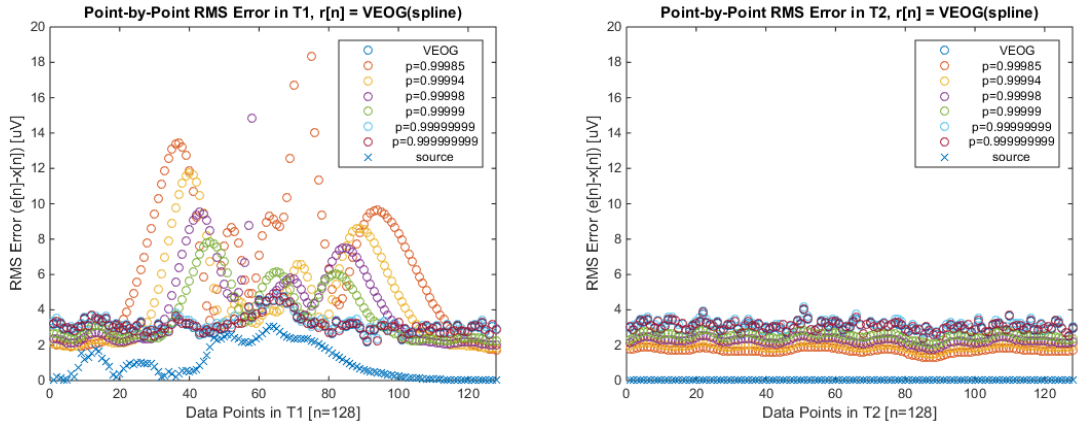

Figure 31. Temporal average RMS error for T1 and T2 using lpRLS and r[n] = r(spline). Results for r[n] = VEOG and r[n] = r(source) are also shown for comparison. Note that extreme errors with RMS errors of > 100 [uV] exist for smoothing spline parameters p = 0.99985 and p = 0.99998 during T1, but the y-axis has been scaled to a maximum of 20 [uV].

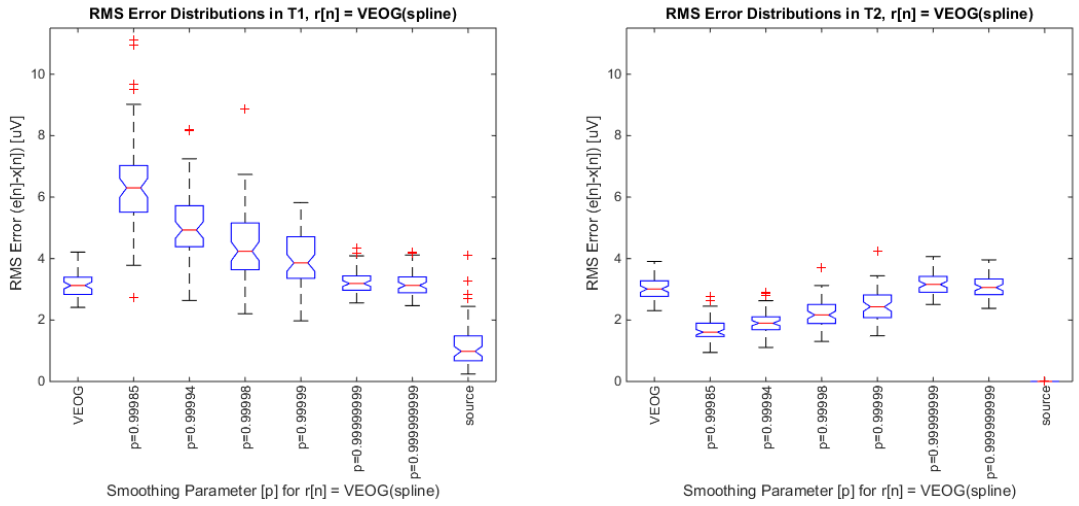

Figure 32. Exemplar RMS error distributions for T1 and T2 using lpRLS and r[n] = r(spline). Results for r[n] = VEOG and r[n] = r(source) are also shown for comparison. For the purposes of reducing the influence of the extreme errors noted in Figure 31, any distribution outliers above the y-scale shown in T1 were replaced with the group (by level) mean.

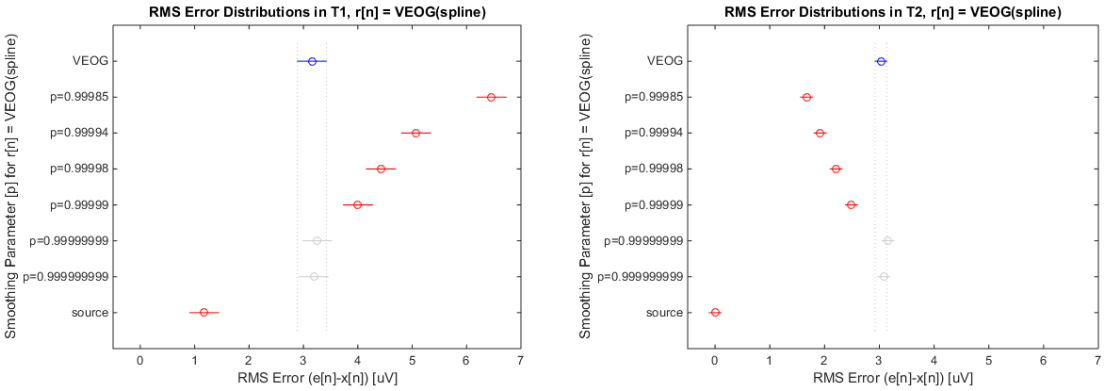

Figure 33. Post-hoc, pairwise comparisons for T1 and T2 using lpRLS and r[n] = r(spline). Results for r[n] = VEOG and r[n] = r(source) are also shown for comparison. For the purposes of reducing the influence of the extreme errors noted in Figure 31, any distribution outliers above the y-scale shown in T1 were replaced with the group (by level) mean.

The one-way ANOVA for smoothing parameter had a significant main effect, $F_{(7,479)} = 146.2892$, $p < 0.001$, $\eta_p^2 = 0.70$, for T1. General trends in the post-hoc, pairwise comparisons revealed that the smoothing spline was not able to reduce the error in T1 beyond what was achievable with prior art using r[n] = VEOG; further, the majority of smoothing parameter choices significantly increased the error in T1. For T2, the one-way ANOVA for cutoff frequency of the low-pass filter also had a significant main effect, $F_{(7,479)} = 434.9843$, $p < 0.001$, $\eta_p^2 = 0.87$. Smoothing parameters at p = 0.99999 and below were able to significantly reduce the error in T2 as compare to r[n] = VEOG, while smoothing parameters larger than this value did not significantly vary from r[n] = VEOG. The lowest aggregate error in T2 at p = 0.99985 was still significantly higher than r[n] = r(source). As compared to r[n] = VEOG, any choice of smoothing parameter that significantly reduced error in T2 also resulted in a significantly increased error in T1, making smoothing spline a particularly poor choice for conditioning the reference noise input; as such, a full analysis of the post-hoc, pairwise comparisons for the smoothing splines is omitted, and all results from the smoothing spline analysis are omitted from further omnibus testing.

BAYESIAN ADAPTIVE REGRESSION SPLINES

The BARS algorithm was implemented using a MATLAB port of the toolbox written by Wallstrom, Liebner, and Kass [94] <http://www.cnbc.cmu.edu/~rkelly/code.html>[4]. The BARS filter, like previously described methods for low-pass filtering and spline smoothing, was applied to r[n] = VEOG assuming a Poisson fitting process to the underlying data distribution [94]. Whereas the general smoothing spline algorithm was unable to smooth the artifact-free segments (T2) without distorting the blink artifact (T1), the adaptive spline is hypothesized to achieve both adequate smoothing and artifact shape preservation. The results for BARS filtering the reference

[4] Specific implementation details for the BARS algorithm are giving in Appendix E.

noise input are shown in Figure 34 (temporal aggregate), Figure 35 (exemplar boxplots), and Figure 36 (post-hoc, pairwise multiple comparisons).

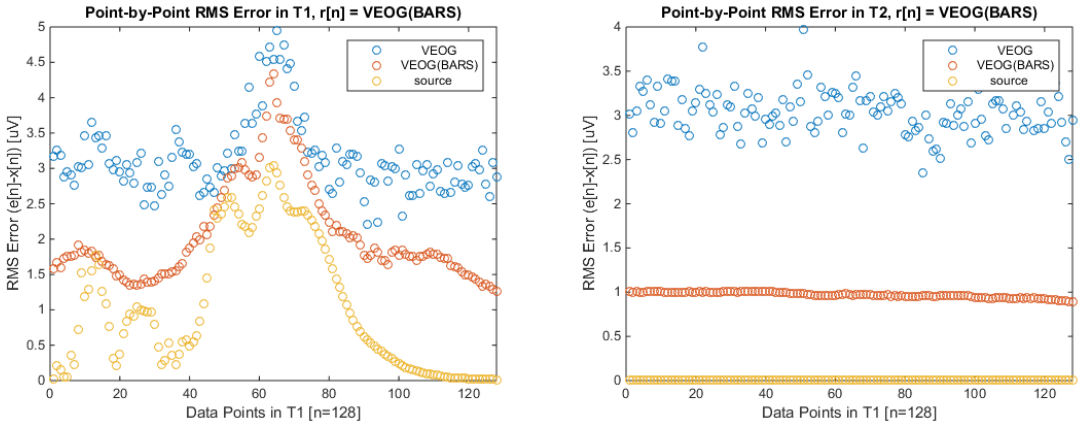

Figure 34. Temporal average RMS error for T1 and T2 using lpRLS and r[n] = r(BARS). Results for r[n] = VEOG and r[n] = r(source) are also shown for comparison.

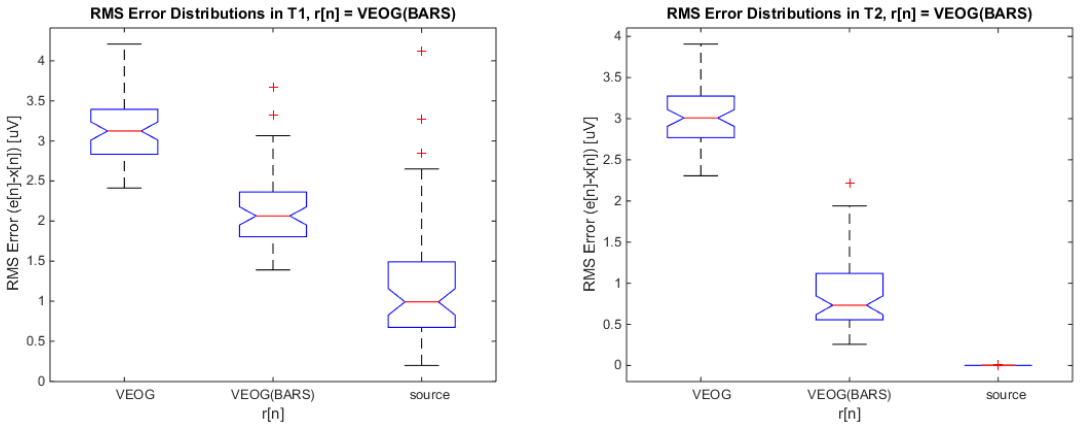

Figure 35. Exemplar RMS error distributions for T1 and T2 using lpRLS and r[n] = r(BARS). Results for r[n] = VEOG and r[n] = r(source) are also shown for comparison.

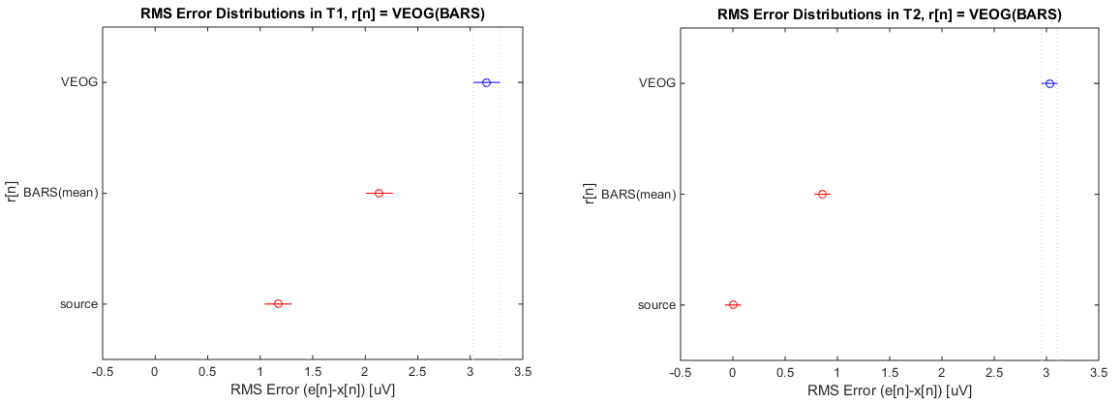

Figure 36. Post-hoc, pairwise comparisons for T1 and T2 using lpRLS and r[n] = r(BARS). Results for r[n] = VEOG and r[n] = r(source) are also shown for comparison.

The one-way ANOVA for comparing BARS to r[n] = VEOG and r[n] = r(source) had a significant main effect, $F_{(2,179)} = 176.3779$, $p < 0.001$, $\eta_p^2 = 0.67$, for T1. Post-hoc, pairwise comparisons (Table) revealed that each algorithm produced significantly different results from all other algorithms, $p < 0.001$, with BARS producing a significantly lower error than r[n] = VEOG that was also significantly higher than that produced by r[n] = r(source). For T2, the one-way ANOVA also had a significant main effect, $F_{(2,179)} = 1259.97$, $p < 0.001$, $\eta_p^2 = 0.93$. The post-hoc, pairwise comparisons for T2 were quite similar to those for T1, with BARS resulting in significantly ($p < 0.001$) less error than r[n] = VEOG, but also significantly ($p < 0.001$) more error than r[n] = r(source).

Table 6. Post-hoc, pairwise comparisons for T1 and T2 using BARS. Comparisons resulting in significant differences ($\rho < 0.05$) are highlighted in orange.

Segment	Paired Comparison	μ	95% CI	p-value
T1	r(VEOG), r(BARS)	1.0214	[0.7738, 1.2690]	< 0.001
T1	r(VEOG), r(source)	1.9837	[1.9837, 2.2313]	< 0.001
T1	r(BARS), r(source)	0.9623	[0.9623, 1.2099]	< 0.001
T2	r(VEOG), r(BARS)	2.1721	[2.0264, 2.3178]	< 0.001
T2	r(VEOG), r(source)	3.0260	[2.8803, 3.1717]	< 0.001
T2	r(BARS), r(source)	0.8538	[0.7082, 0.9996]	< 0.001

NON-LOCAL MEANS

The final algorithm to be tested for reduction in cross-talk was NLM. NLM was allowed to use the entirety of the available signal for its search neighborhood, and the variance of the underlying EEG data were calculated directly from Fp1(t) = **EEG**(Fp1,t), leaving only the patch size, P, as a user-selectable parameter for the algorithm. While a suitable patch size may be estimated

from the characteristic dimension of the underlying signal observation, a number of patch sizes can be simulated in post-hoc analysis for a better understanding of how patch size might affect the error in the recovered EEG signal. The results for NLM filtering the reference noise input are shown in Figure 37 (temporal aggregate), Figure 38 (exemplar boxplots), and Figure 39 (post-hoc, pairwise multiple comparisons).

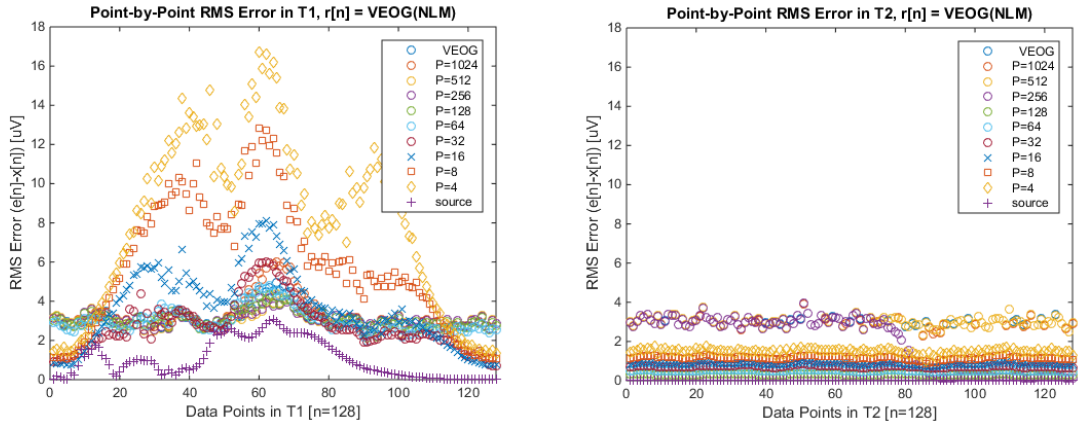

Figure 37. Temporal average RMS error for T1 and T2 using lpRLS and r[n] = r(NLM). Results for r[n] = VEOG and r[n] = r(source) are also shown for comparison.

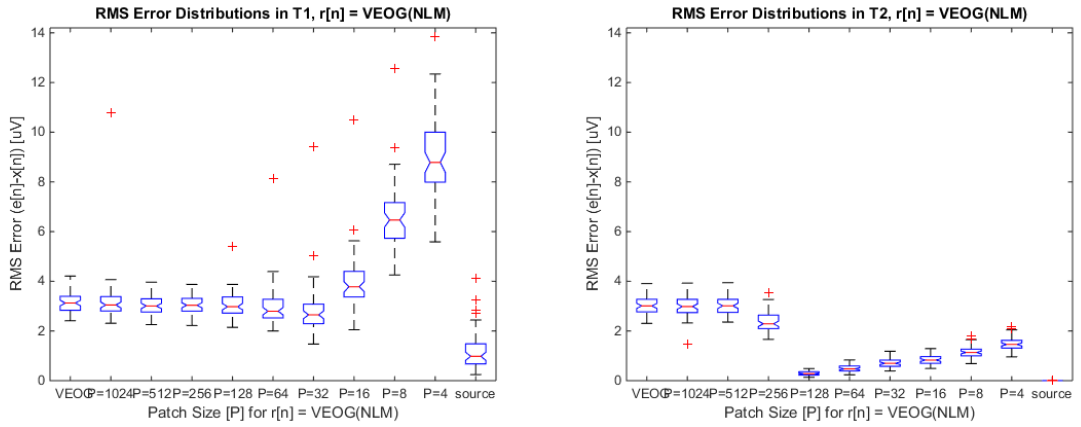

Figure 38. Exemplar RMS error distributions for T1 and T2 using lpRLS and r[n] = r(NLM). Results for r[n] = VEOG and r[n] = r(source) are also shown for comparison.

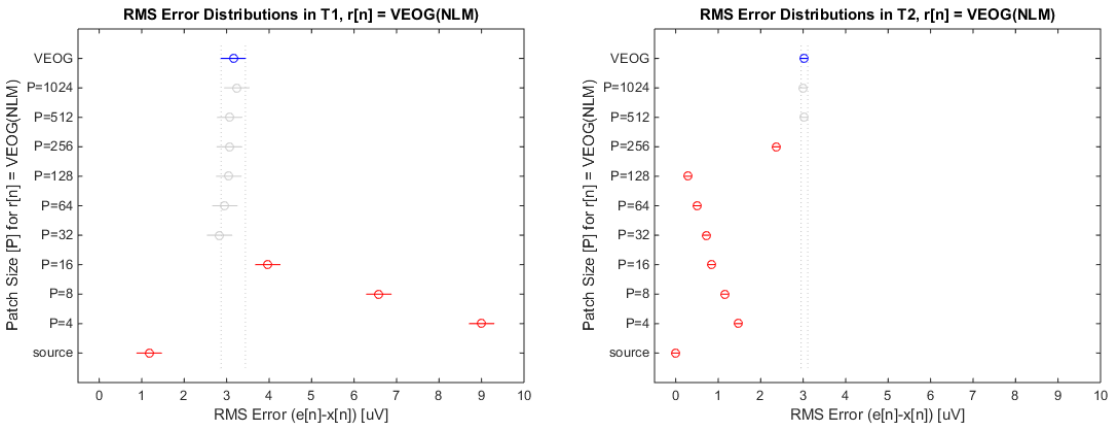

Figure 39. Post-hoc, pairwise comparisons for T1 and T2 using lpRLS and r[n] = r(NLM). Results for r[n] = VEOG and r[n] = r(source) are also shown for comparison.

The one-way ANOVA for patch size had a significant main effect, $F_{(10,659)} = 289.5125$, $p < 0.001$, $\eta_p^2 = 0.82$, for T1. Post-hoc, pairwise comparisons for T1 suggest that NLM was unsuccessful ($p \approx 1$ in most cases) at reducing the error beyond that achievable with r[n] = VEOG; further, patch sizes of size 16 (62.5 [ms]) or smaller significantly increased the error ($p < 0.001$). All patch sizes produced errors significantly greater ($p < 0.001$) than r[n] = r(source). For T2, the one-way ANOVA also had a significant main effect, $F_{(10,659)} = 1120.8387$, $p < 0.001$, $\eta_p^2 = 0.95$. The post-hoc, pairwise comparisons for T2 show results that are much different than were obtained in T1. All patch sizes of 256 (1 [s]) or smaller produced significantly ($p < 0.001$) lower error than r[n] = VEOG, the smallest of which were patch sizes of 128 [0.5 [s]), 64 (0.25 [s]), and 32 (0.125 [s]). None of the patch sizes, however, could achieve an error significantly equal to or less than ($p < 0.001$) r[n] = r(source). Because of the number of post-hoc, pairwise comparisons, the full table can be found in Appendix F.

OMNIBUS ANALYSIS

Having completed each individual algorithm analysis, the final evaluation stage is to compare the best-performing parameters from each algorithm against ICA, considered to be the benchmark of performance for this problem set. From the low-pass filtering algorithm, the results at fc = 15 [Hz] represent the most balanced between not increasing error during T1 while

decreasing error during T2 (relative to r[n] = VEOG). Although not statistically different from fc = 20 [Hz] during T1 or T2, the absolute error for fc = 15 [Hz] was less during T2; either would have been a suitable choice for comparison. The smoothing spline algorithm is not represented in the omnibus analysis because any reduction in error during T2 was accompanied by an increase in error in T1, thus making it unsuitable for implementation. The remaining two approaches are BARS (no variation in parameters) and NLM with a patch size of 128 data points (0.5 [s]). The 128-point patch size was chosen for its overall minimal error during T2, although not significantly different than either 64- (0.25 [s]) or 32-point (0.125 [s]) patch sizes, without increasing error during T1; arguably, NLM would have been equally represented by either the 128-, 64-, or 32-point patch sizes.

From the individual algorithm analyses, two outcomes became clear: NLM produced superior results in direct comparison to any other algorithm during T2, with an overall mean RMS error of 0.2905 [uV]; BARS was the next lowest at an overall mean RMS error of 0.8560 [uV]. For T1, BARS was the only algorithm tested to offer a statistically ($p < 0.05$) better error that r[n] = VEOG, with an overall mean RMS error of 2.134 [uV]. With NLM appearing optimal for T2 and BARS appearing optimal for T1, the two algorithms were also tested together, applied serially to r[n] = VEOG. To test for any effect of order of operations in the serial processing pipeline, both orders were performed. Thus, a hypothesized optimal algorithm implementation, NLM+BARS, or BARS+NLM for the opposite order of operations, was also tested; their results are included in the omnibus analysis. The results of the omnibus analysis are shown in Figure 40 (temporal aggregate), Figure 41 (exemplar boxplots), and Figure 42 (post-hoc, pairwise multiple comparisons).

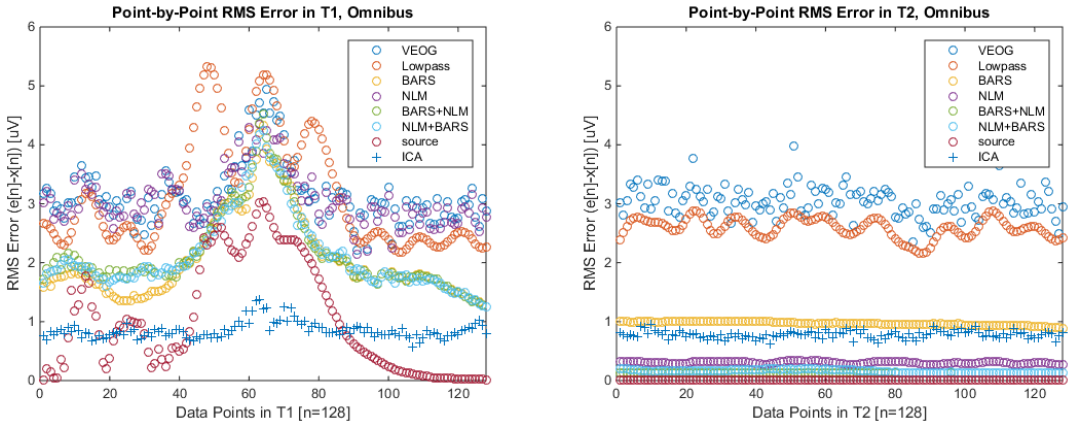

Figure 40. Temporal average RMS error for T1 and T2, omnibus analysis.

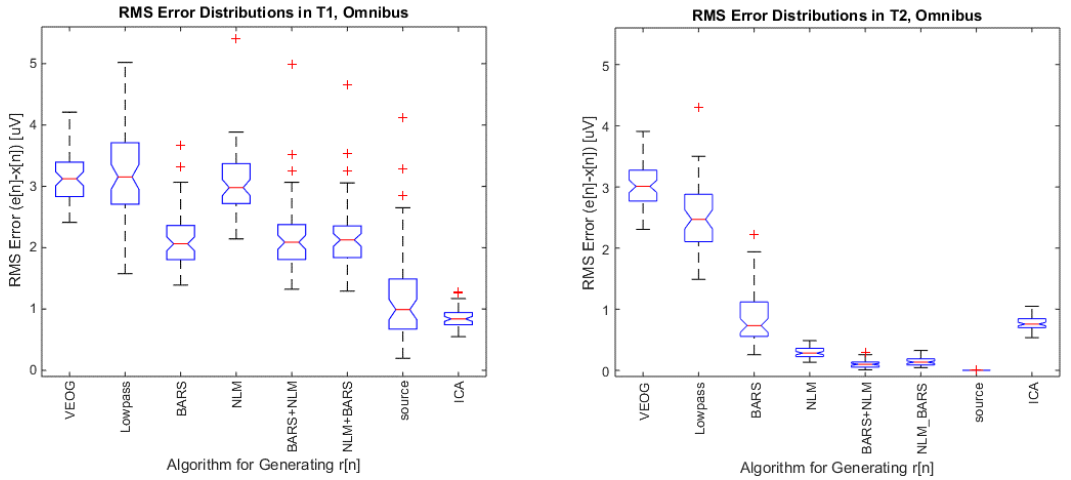

Figure 41. Exemplar RMS error distributions for T1 and T2, omnibus analysis.

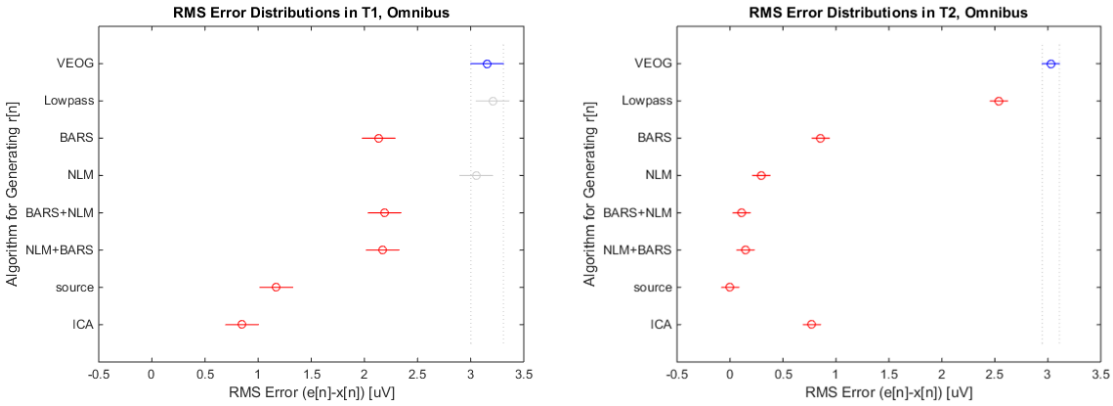

Figure 42. Post-hoc, pairwise comparisons for T1 and T2, omnibus analysis.

The one-way ANOVA for the omnibus analysis had a significant main effect, $F_{(7,479)} = 154.1127$, $p < 0.001$, $\eta_p^2 = 0.70$, for T1. Post-hoc, pairwise comparisons for T1 suggest that BARS,

BARS+NLM, and NLM+BARS produced significantly ($p < 0.001$) lower errors as compared to r[n] = VEOG. All of the algorithms produced significantly higher ($p < 0.001$) than ICA. For T2, the one-way ANOVA also had a significant main effect, $F_{(7,479)} = 953.8254$, $p < 0.001$, $\eta_p^2 = 93$. The post-hoc, pairwise comparisons for T2 revealed that all algorithms reached a significantly ($p < 0.001$) lower error than r[n] = VEOG. Both the BARS+NLM and NLM+BARS achieved the lowest overall errors; these errors were not significantly ($p = 0.47$ and $p = 0.13$, respectively) different than that achieved using r[n] = r(source). Each of the algorithms that were NLM in part or in whole obtained significantly lower errors ($p < 0.001$) than ICA. Because of the number of post-hoc, pairwise comparisons, the full table can be found in Appendix G.

REAL DATA EXAMPLE

While quantitative comparisons to the true, underlying EEG signal using real data are impossible to achieve, there is still tremendous value in visualizing results with real data to verify algorithm performance. To that end, the RLS, ICA, and lpRLS(NLM+BARS) algorithms were used on a small, real dataset for illustrative purposes. This dataset was the original data used to select the blink exemplars (Figure 6). Both the recovered, clean EEG, as well as the estimated. ocular artifact, for each algorithm are shown in Figure 43 and Figure 44, respectively. For comparison, both the recovered, clean EEG and estimated, ocular artifact are plotted against the original signal measured at Fp1.

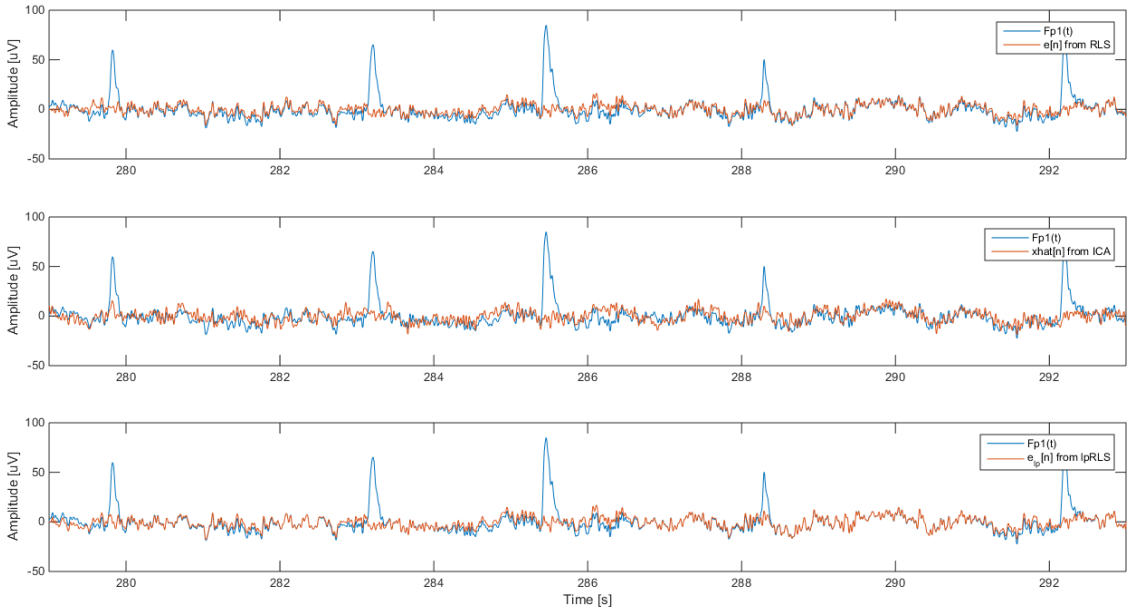

Figure 43. RLS, ICA, and lpRLS(NLM+BARS) applied to a real dataset and the recovered, clean EEG. From top to bottom, the recovered, clean EEG from RLS, ICA, and lpRLS(NLM+BARS) is plotted against the original signal recorded at Fp1.

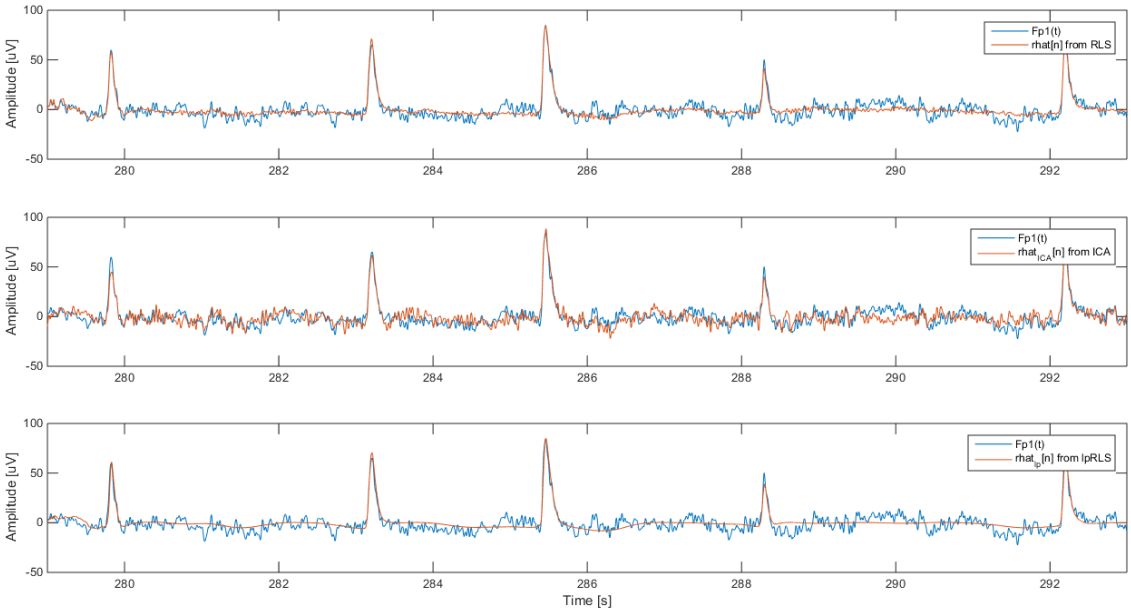

Figure 44. RLS, ICA, and lpRLS(NLM+BARS) applied to a real dataset and the estimated, ocular artifact. From top to bottom, the estimated, ocular artifact from RLS, ICA, and lpRLS(NLM+BARS) is plotted against the original signal recorded at Fp1.

Figure 43 shows that while all three methods appear to sufficiently attenuate the blink artifact, only lpRLS(NLM+BARS) was able to do so without significantly disturbing the true EEG in the absence of any artifact signal. This can also be visualized in Figure 44 by noticing that

lpRLS(NLM+BARS) estimate the ocular artifact as having an approximate zero magnitude in areas of the data during which no blink was occurring. These figures, together, demonstrate the potential confound in evaluating artifact removal methods based on visual inspection alone. From Figure 43 by itself, and without the presence of the lpRLS results or the quantitative analysis made possible by biophysically-inspired data simulation, one may come to an incorrect conclusion that RLS and ICA produce comparable, and sufficient, results concerning the removal of ocular blink artifact.

IV. DISCUSSION

AN IMPROVED ADAPTIVE FILTERING APPROACH: SUCCESS?

This work set out to explore the space by which the method of adaptive filtering could be improved in its usefulness as an algorithm for correcting, or removing, ocular artifact from EEG. Improvement was defined as achieving a level of performance, or error in recovering the true, underlying EEG signal, equal to or improved over that which could be obtained by blind source separation as realized by the extended infomax ICA algorithm. Following this, a realistic, biophysically-inspired modeling approach was developed to order to allow for carefully controlled data characterization that would permit quantitative evaluation of artifact correction algorithm performance; this was necessary in order to overcome the challenges inherent in volume conduction that limit the use of real data in this context to qualitative assessment. Knowing that the simulated data have a shared structural and functional representation with that of the true, electrophysiological generating processes is critical to having confidence in its use with real data, which is the ultimate goal.

To achieve more meaningful quantitative comparison, a new approach was developed for studying the effects of any ocular artifact contamination algorithm on both the ability to remove artifact when present as well as the capability to retain the original, undistorted waveform when not present. Concurrent analysis of these segments, labeled as T1 and T2, respectively, permitted a more comprehensive understanding of algorithm utility than achieved in most prior art. Further, it facilitated an investigation into adaptive filtering, more specifically RLS adaptive filtering, and its challenges for both correction of ocular artifact and distortion of the true EEG. This line of

analysis presented two, major areas of improvement to pursue: correctly estimating the shape of the blink artifact waveform given a non-linear phase response of the filter and cross-talk, or bidirectional contamination, of the reference noise input. More explicitly, it was hypothesized that improved phase alignment in the estimated ocular artifact source, r[n], would result in less error at the signal recovery stage of the algorithm that involves the subtraction of e[n] from the original, measured signal, s[n]. The second hypothesis developed in regard to cross-talk was that eliminating EEG contamination of the reference noise input signal should prevent a phenomenon known as 'overcorrection' whereby the adaptive filter removes correlated EEG data that appear in both the primary input and the reference noise input due to volume conduction. This reduction of cross-talk was required to be done without a significant mischaracterization of the blink artifact as represented in the reference noise input in order to maintain good removal of the blink artifact, as well. The theorized best-case performance for achieving both of these improvement goals was given by using a reference noise input, r(source), that was generated from the model data. This reference noise input was optimally conditioned for the adaptive filter in that it was free of EEG cross-talk and contained a perfect estimation of the ocular artifact data as measured from the bipolar VEOG signal, a practical source of generating the reference noise input from real data sources. In additional to meeting or exceeding the performance of extended infomax ICA, the realization of r(source) provided a second objective, which was achieving the minimal theoretical error achievable with RLS using r[n] = r(source) as the reference noise input.

When corrected for phase alignment due to the non-linear phase response of the RLS adaptive filter using a new approach, linear-phase RLS, or lpRLS, adaptive filtering, it was discovered that the ideal realization of an adaptive filter could equal the performance of ICA during T1 while exceeding the performance of ICA during T2. Thus, the motivating example that was only possible to demonstrate given the biophysically-realistic data provided intrinsic proof

that adaptive filtering could offer the performance of ICA for ocular artifact removal while maintaining other beneficial properties not otherwise afforded by ICA such as online, point-by-point processing, the ability to adapt to non-stationary processes, negligible computation time, and use for data cases with as few as two data channels (a primary input and a reference noise input). Pursing this ideal realization required not only the linear-phase RLS implementation, but also new approaches for obtained a reference noise input that was ideally free of EEG cross-talk. To that end, four signal conditioning approaches, each applied to r[n] = r(VEOG), were proposed to better evaluate and study how that may be achieved: low-pass filtering, smoothing splines, Bayesian adaptive regression splines (BARS), and non-local means (NLM) filtering. Each approach was evaluated over a plausible range of input parameters, where necessary, and its performance was compared to using reference noise inputs of r[n] = r(VEOG), as in prior art, or r[n] = r(source) as demonstrated to be the optimal case for lpRLS. An analysis of the results for each algorithm separately revealed a new hypothesis by which the properties of BARS to accurately estimate the ocular artifact and NLM to reduce cross-talk could be mutually leveraged by serially applying them to r[n] = r(VEOG) was formed. This algorithm, termed NLM+BARS produced the lowest errors, overall, of all the lpRLS approaches, in both T1 and T2.

When compared to r[n] = r(source) and ICA, NLM+BARS achieved both of its goals for T2: the reduction of EEG cross-talk achieved by the new algorithm produced less error than ICA ($p < 0.001$) and equated the error achievable with r[n] = r(source) ($p > 0.1$). This was also an improvement ($p < 0.001$) over lpRLS using r[n] = r(VEOG). For T1, NLM+BARS was able to significantly reduced the error ($p < 0.001$) as compared to lpRLS using r[n] = r(VEOG) by nearly a full RMS [uV] (2.19 RMS [uV] and 3.155 RMS [uV], respectively). While this represents a significant improvement over prior art RLS adaptive filtering, NLM+BARS did not achieve as low of an error during T1 as theorized by r[n] = r(source), or as demonstrated by ICA.

Overall, this work was very successful. To achieve a performance equal to or better than ICA was a very optimistic goal to have for an algorithmic approach that has seen little to no active development in the literature since the work of He et al. [11] [12] first demonstrated its significant utility. The importance of achieving an overall best performance during T2 is further underscored in that most laboratory study data are heavily weighted to periods of time that are not influenced by ocular artifact. While this may not necessarily be the case in studies with increased ecological validity or realism, it only serves as a motivator for continued improvement of the algorithm in parallel with the increased utility of real-world neuroimaging technologies that are facilitating the use of EEG outside of the laboratory [95]. With a mind toward that goal, and a demonstrated success of the newly developed methods for lpRLS(NLM+BARS), there are a number of very interesting findings throughout and points of discussion to make from the overall body of work presented here.

T1 VS. T2: AN INTERPRETATION

The originally-motivating choice for analyzing T1 and T2 separately was the necessity to quantify any algorithm's performance for not only removing ocular artifact when present, but also for preserving uncorrupted EEG data that wre not influenced by the detectable presence of ocular artifact.[5] This framework lent itself to adopting T1 as the segment by which ocular artifact removal could be judged while allowing T2 to serve as a reference point for any possible distortion of the underlying EEG data. As noted from using r[n] = r(source) with lpRLS in Figure 23, a near-perfect

[5] The differentiation that an artifact be detectable implies that artifact may be present, but undetectable, in a signal. For example, Romero, Mañanas, and Barbanoj (2009) used data from an eyes-closed resting state to simulate their 'clean' EEG data. During eyes-closed resting states, and sometimes during eyes-open (e.g. [107]), low-frequency potentials exist in the EEG data that are generated from slow movements of the ocular dipole, a type of ocular activity known as slow eye movement (SEM). Although SEMs are observable to a trained experimentalist, their relative lower amplitude make them far less observable in EEG data alone. This point serves two purposes: first, even 'clean' EEG data is likely to have some artifactual component, and second, not all artifact is as readily identifiable as, for example, eye blinks.

(the RMS error in every segment, while not observable from the figure due to y-axis scaling, was less than 0.01 [uV]) recovery of the true EEG signal during T2 is achievable when EEG cross-talk is eliminated from the reference noise input. Thus, an understanding of what algorithm performance features are most critical during T2 is well understood.

T1 presents a slightly more complicated interpretation. Under no choice of adaptive filtering algorithm or reference noise input, ICA to be included, did T1 achieve the same near-perfect signal recovery as T2. Eliminating cross-talk (Figure 16) showed a strong improvement in RLS, and further solving the non-linear phase effects of RLS with lpRLS (Figure 23) also reduced the error in T1. This can be primarily interpreted to mean that there is still room for improvement in the estimation of the ocular artifact during T1 by the adaptive filter. A secondary interpretation that perhaps also contributes to the error during T1, although likely to a less significant degree, is that cross-talk elimination during T1 is not as optimal as during T2.

A formal proof of this idea is difficult to achieve as any signal conditioning algorithm applied to the reference noise input can potentially affect both the characterization of the blink artifact and the observed EEG cross-talk. As an example, the individual algorithm results for NLM and BARS would suggest that NLM improves T2 and BARS primarily improves T1 but also improves T2, as well (as their combined performance is superior to either algorithm alone during T2). It would be possible to simulate a 2x2 design of T1 with factors of blink artifact (with and without) and EEG cross-talk (with and without) in the reference noise input to better understand this problem space in the context of using NLM, BARS, and NLM+BARS to condition the reference noise input; this would be and interesting, future analysis to perform in an effort to clarify the contribution of error sources during T1 more succinctly.

ON THE SUITABILITY OF lpRLS AS A SOLUTION TO PHASE ALIGNMENT

The implementation of lpRLS requires a delay of the primary input, s[n], to the recursive algorithm that is then compensated at the output of the algorithm by the delay that is introduced to the estimation of $\hat{r}[n]$ as constrained by Type I FIR. As evidenced by the analysis presented here (Figure 25 and Figure 26), this approach leads to a significantly reduced error in estimating the ocular artifact after the filter response has converged, or stabilized, during T1. The result of delaying s[n] is that the recursion algorithm seeks to solve an expected value minimization problem between s[n-d] and r[n]. Figure 24 clearly illustrates that this new relationship between s[n-d] and r[n] changes the magnitude response of the filter, although this should be expected given that phase response of the filter has been constrained to a new form. What is interesting to see is that there is also a change in the *characteristic* of the magnitude response, as well. In Figure 24, there is a small inflection in the magnitude response of the RLS filter just beyond t = 307.25 [s], and a similar inflection in the magnitude response of the lpRLS filter at or near the same time. This inflection is more directly characterized in Figure 45.

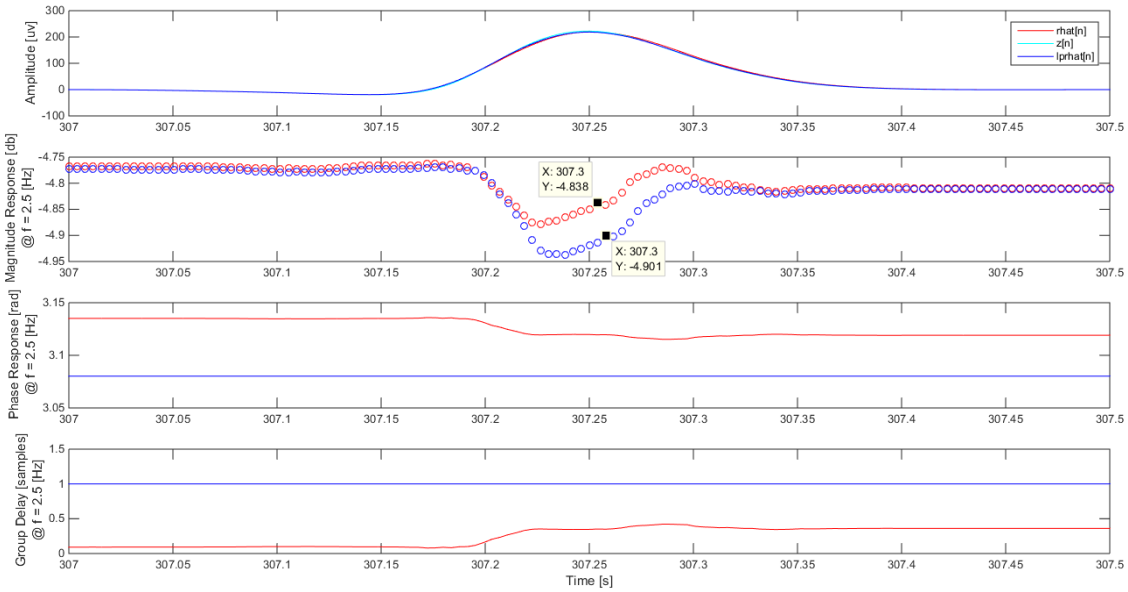

Figure 45. Magnitude, phase, and group delay responses for h[m] and h_{lp}[m] during T1 using RLS and lpRLS, respectively. The reference noise input for both algorithms was r[n] = r(source). The data shown on the first subplot, $\hat{r}[n]$, $z[n]$, and $\hat{r}_{lp}[n]$ are from the same blink artifact segment shown in Figure 21. This is a replication of Figure 24 that specifically highlights the inflection seen in the magnitude responses just after t = 307.25 [s] using datatips.

What is seen in Figure 45 is that the inflection that was originally seen in the magnitude response of the RLS filter is *delayed* by a single sample point in the lpRLS filter; at M = 3, this delay of d = 1 is equivalent to the delay of the s[n] at the input to the adaptive filter. Could this be evidence that the delay of s[n], while ultimately solving the non-linear phase delay of the RLS method, is actually introducing a *delay* into the convergence of the magnitude response of the filter? The proof is not difficult to understand: if RLS is solving an expected value minimization of $E(e[n]^2) = E[(z[n]- \hat{r}[n])^2]$ [11], then lpRLS is solving a *delayed* expected value minimization of $E(e[n-d]^2) = E(x[n-d]^2) + E[(z[n-d]- \hat{r}[n])^2]$. If at some point n, $n = n_0$, there is no blink artifact, then $E(x[n_0-d]^2) = E(e[n_0-d]^2) = z[n_0-d] = 0$, which would also imply that $\hat{r}[n] = 0$. Now, at the *next* data point n, $n_1 = n_0 + 1$, assume that there is blink artifact. Even so, the exact same equation holds true for $d \geq 1$: $E(x[n_1-d]^2) = E(e[n_1-d]^2) = z[n_1-d] = 0$. Why? Because, at $d \geq 1$, $n_1 \leq (n_0 - d)$, which implies that the blink has not yet appeared in z[n-d], and thus $\hat{r}[n] = 0$ and $n_1 = n_0 + 1$ *even when r[n] ≠ 0!* In fact, $\hat{r}[n] = 0$ will hold true until $n = n_d = (n_1 + d)$, at which time the recursive equation will 'see'

the blink artifact such that $z[n_d] = z[n_1 + d - d] = z[n_1]$, and $z[n_1] > 0$ when the blink artifact starts. Thus, ***the linear-phase adaptive filter will estimate the ocular artifact as being absent until the delay has shifted the artifact-contaminated primary input into the expected value minimization recursion after it appeared in the reference noise input [d] samples prior***. The end result is that the magnitude response convergence will also be delayed by [d] samples, as shown in Figure 45 for the case where M = 3 and d = 1. The effect of this delay for small values of M may be negligible given that z[n] is of small amplitude at the onset of eye closure. Further, the results presented here indicate that the net effect of allowing for phase alignment with some small error in the magnitude response for M = 3 is still a positive reduction in overall RMS error across the duration of the blink artifact.

For this implementation on lpRLS, small error in the ideal magnitude response is further compounded by imprecision in the filter coefficients due to numerical error associated with the matrix inversion. As discussed in Appendix B, the choice made for the analysis presented here was to preserve linear phase at the cost of small errors in the magnitude response by reflecting coefficients from the first half of the recursively-determined filter, $h_{lp}[m]$. While the impact of this imprecision has not been objectively quantified, it still remains that this particular lpRLS approach achieved overall less error than prior art RLS (Figure 23). Given these other, potential sources error, it is possible that the linear-phase constraint may be implemented in other computational forms such as to eliminate the delay in magnitude response convergence and numerical imprecision due to matrix inversion. Future work should explore these concepts in more detail to see if the lpRLS approach may be further improved from what has been demonstrated here.

It is also of note to discuss the potential inappropriateness of the assumption of phase alignment between the estimated artifact and measured data sources in real data situations. From a purely biophysical perspective, the assumption of phase alignment (from linear superposition)

is well-justified and understood. However, in practical data collection and acquisition, sources of misalignment could arise from small differences in analog to digital conversion hardware, dissimilar filters (such as low-pass or band-pass filtering, both of which are very common processes in EEG data analysis) being applied to the estimated artifact and measured data sources prior to adaptive filtering, or other, unknown sources of electromagnetic interference. In these cases, allowing for the non-linear phase response of the RLS adaptive filter may be preferred. While future exploration of this notion is warranted, the selection of linear- or non-linear phase response may ultimately be a choice left to the individual researcher or practitioner based on their knowledge of the underlying data.

ON THE CHOICE OF RLS AND lpRLS ALGORITHM PARAMETERS

Throughout this work, a number of choices were made for many algorithm parameters. Some algorithm parameter choices were simulated over a range of plausible values; others were fixed based on the recommendations of prior art. The discussion in this section concerns these choices, their justification, and, where appropriate, an analysis of their simulation as it pertains to the adaptive noise cancellation problem of removing ocular artifact from EEG.

LINEAR-PHASE ADAPTIVE FILTERING: M AND λ

The choice of $M = 3$ and $\lambda = 0.9999$ for both the RLS and lpRLS filter implementations used in this work was motivated by that which was recommended by He et al. [12]. As a practical choice, $M = 3$ is logical because it allows for other processes that may not be purely frequency-independent to be tolerated. These processes could arise from variable impedance at the electrode interface, as properties of the analog-to-digital conversion, or due to other, un-specified sources not of electrophysiological origin. The choice of λ, the forgetting factor, is also a practical choice that is made based on the estimated temporal characteristics of any possible non-stationary. The choice of λ, $0 \leq \lambda \leq 1$, is determined by the equation $\lambda^N = 0.5$, where N is the

estimated window length that contributes some weight to the current filter coefficients. A value of λ=0.9999 allows for a window of approximately 30 [s] at the sampling rate of 256 [Hz] used here. The special case where M = λ = 1 is that of special case of linear regression [12]. While additional values for M and λ are not simulated here, and the volume conduction model used for the simulated data were assumed to be frequency independent and without any sources of non-stationarity, this work shows that a practical choice of M = 3 and λ = 0.9999 can still produce quality results under the simplest of simulation conditions. The benefits of M > 1 and λ < 1 may be explored in future analyses that are explicitly focused on sources of frequency dependence and non-stationarity.

LOWPASS FILTERING: f_c

The low-pass filtering cutoff was varied over a range of frequencies expected to be seen in EEG. The error results produced by this process are consistent with a preservation of the blink artifact in T1 coupled with an attenuation of the EEG cross-talk in T2 at or around the frequencies that reasonably separate the spectral content of the blink from the large-amplitude frequencies seen in EEG between 15 and 20 [Hz] (Figure 28, Figure 29, and Figure 30). Above 20 [Hz], any attenuation in higher-frequencies was insufficient to result in reduced error during T2; below 15 [Hz], the distortion of the blink artifact was enough to increase the error during T1. While cutoff frequencies of 15 and 20 [Hz] could provide some decrease in error during T2, it was the highest of any error (other than r[n] = VEOG) found in the omnibus results (Figure 40, Figure 41, and Figure 42). Having observed these results, low-pass filtering should not be considered a viable candidate for conditioning the reference noise input.

SMOOTHING SPLINE: p

The choice of smoothing spline was meant to serve as a basis for comparison to BARS, primarily. When faced with the challenge of smoothing the non-artifact segments while trying to

minimize degradation while minimizing the blink signature in T1, the smoothing spline failed to achieve reasonable results for any choice of the smoothing parameter, p (Figure 31, Figure 32, and Figure 33). A smoothing of the non-artifact data during T2 resulted in distortion of the blink signature in T1 that increased the ocular source noise estimation error in exchange for any improvement that may have been achieved during T2. As a result, smoothing splines should not be considered to have any value in this adaptive noise cancellation problem, save for a baseline comparison to BARS in this work only.

BAYESIAN ADAPTIVE REGRESSION SPLINES

The goal of the BARS algorithm is, in essence, to achieve what a generic smoothing spline cannot: adequate smoothing of the non-blink segments while preserving the shape and characteristics of the blink signature. This is accomplished via the free-knot splines procedure, where the knots, or endpoints, of the spline fits to the data time series are adaptively adjusted. Concentrating the knots around the blinks, as discussed by Wallstrom et al. [70], allows for the characteristic blink shape to be retained when it would otherwise be smoothed by the sparsely-placed knots during non-ocular events that effectively attenuate the EEG cross-talk. Applying the BARS algorithm to reference noise input r[n] = VEOG resulted in significantly less error during both T1 and T2 over prior art, although neither reached equivalence to the theoretical error achievable as given by r[n] = r(source) (Figure 40, Figure 41, and Figure 42).

NON-LOCAL MEANS: P

The concept of NLM averaging is to preserve edges in either one- or two-dimensional signals. When applied to the reference noise input, it was hypothesized that NLM would preserve the blink artifacts as observed during T1 while attenuating the EEG cross-talk in T2; this was the case as demonstrated by the empirical results (Figure 37, Figure 38, and Figure 39). The effect of patch size, P, on the errors obtained during both T1 and T2 can be easily explained by considering

properties of the simulated data. A patch size equal to or approximating the characteristic signature of the signal that is to be preserved should be the best choice. In the simulated data here, the blink artifact exemplars were 128 data points in length; not surprisingly, P = 128 had the lowest overall error during T2. However, the error during T2 for P = 128 was not significantly different from that achieved by P = 64 and P = 32, as well. The characteristic blink itself is typically between 100-200 [ms] in half-amplitude duration [85], and thus the full width of the eye closure from open, to close, to open again extends slightly beyond that range. The other patch sizes that were not significantly different from P = 128 more closely align to characteristics of the blink itself from open, to close, to open (P = 64, or 0.25 [s]), or one half of the blink cycle, either open to maximal closure or maximal closure to open (P = 32, or 0.125 [s]). Reducing the patch size further increases the probability that sequences of only a few data points will be highly similar, and thus highly weighted in the non-local means procedure, to many other sequences of only a few data points. Because of the relative abundance of these shorter segments, the relative weighting of the blink artifact may begin to decrease as patch size decreased below P = 32, which would result in an accompanied error during T1; this is the result that was observed (Figure 37, Figure 38, and Figure 39). Patch sizes that were significantly larger than the representative blink signature, either physiologically or by choice of simulation exemplar length, produced little to no chance in either T1 or T2. In this case, the variation in weighting applied to the individual is minimal as the patches themselves become very unique as they grow in size.

NLM+BARS (OR BARS+NLM)

The combination of NLM+BARS takes advantage of the relative strengths of both algorithms: the preservation of the blink signature with the free-knot splines signature coupled with the simultaneous attenuation of the EEG cross-talk and the further attenuation of the EEG cross-talk by the non-local means weighting procedure. While NLM+BARS did not achieve any

further error reduction in T1 in comparison to BARS alone, the combined attenuation of EEG cross-talk in T2 resulted in an error that was not statistically different than what could be achieved with the ideal reference noise input, r[n] = r(source), but was significantly less than what was achieved with ICA.

OTHER EEG ARTIFACTS

Having demonstrated success for eye blink artifact, other EEG artifacts may be sufficiently removed by the lpRLS(NLM+BARS) procedure, as well. Here, the applicability of such a method is extended to other sources of artifact that are common in in EEG data, and a theoretical discussion of the applicability of lpRLS(NLM+BARS) is provided for consideration and to stimulate possible future work.

EOG ARTIFACT AT LARGE: VERTICAL AND HORIZONTAL EYE MOVEMENTS

While only blink artifact were considered in this work, other artifacts due to the rotation of the ocular dipole during vertical and horizontal eye movements are also of interest in the general ocular artifact paradigm. The original implementation of the RLS adaptive filter by He, Wilson, & Russell [11] considered both horizontal and vertical eye movement, in combination with eye blink artifact, as dual inputs to the adaptive noise cancellation algorithm. Visual inspection of these results suggest that the dual reference noise inputs of VEOG and HEOG were successful at attenuating all three types of artifact from the EEG. Given that these results are what inspired this work, it is logical to believe that the framework presented here, which is consistent with the original adaptive filter theory for this noise cancellation problem, would translate well to other sources of ocular artifact.

ELECTROMYOGRAPHIC ARTIFACT

One of the largest reasons for the success of the adaptive filtering paradigm for ocular artifact removal is that ocular artifact can, in general, be represented by a small, finite number of

equivalent dipole noise sources that can be well-represented by a small, finite number of reference noise inputs into the adaptive noise canceller. Further, each equivalent dipole noise source is characteristically well-represented in the EEG data and by a process that does not exhibit any strong interference from other processes. EMG would not be expected to perform well in the adaptive filtering paradigm because it has properties that are representatively worst-cased scenarios for an adaptive filtering paradigm. EMG arises from a finite, although largely unknown, number of equivalent dipole noise sources that are spatially distributed throughout the scalp. Because of its high-frequency characteristic, EMG artifact as observed on the scalp surface often exhibits destructive interference from other EMG sources such that any reference noise input signal that could be obtained for and EMG source may not be well representative of its observation at any given EEG channel. ICA and other blind source separation approaches have shown to be very favorable in comparison to other approaches for the removal of muscle artifact in high-dimensional EEG data (e.g. [96] [97]), although this in and of itself is an enormous literature) and are, of this writing, the preferred method for correction.

ONLINE VS. POST-HOC IMPLEMENTATION

One of the primary, attractive features of the adaptive filter is that its point-by-point process and minimal computational requirements make it ideal for use in real-time, or online, data collection and processing systems (e.g. [68] [69] [98] [99]). For the same reason, although where the constraints of processing time are far more relaxed, it can also be used for post-hoc analysis. In comparison to ICA, which requires an aggregate data matrix on the order of [N x $(20*N^2)$], where N is the number of electrodes in the EEG montage [100], the online processing advantages are quite obvious.

The lpRLS filter described here exhibits the same desirable properties with regard to online processing as the original RLS method. BARS and NLM are, however, sufficiently laborious,

computational processes. In the implementation of BARS presented here, a single data point estimate of its fit in free-knot splines space required anywhere from 3 to 4 [s] on a workstation of era-representative speed (e.g., 64-bit architecture on an Intel Core-i7 chipset @ 2.4 GHz). NLM, for all practical purposes, was equally computationally expensive; a full, exhaustive search of the entire neighborhood of the simulated data used here of required 24 hours or greater in a fully-parallel, quad-core processing architecture on the same workstation. In order for the algorithm to be computationally tractable for online applications, advancements in both NLM and BARS would need to be achieved (either computationally, in hardware, or both). Significant algorithmic work to improve computational requirements as compared to the original NLM approach as implemented here is an ongoing area of research (e.g. [101] [102]).

LEAST-MEAN SQUARES

As part of the point-by-point recursive property of the RLS algorithm, the filter coefficients, h[m], may change with each and every successive data point. As seen in Figure 24, this allows the filter coefficients to quickly adapt to noise when it's seen simultaneously in the reference noise and primary inputs to the algorithm. As the filter changes, it converges on a solution that minimizes the expected value function that is the foundation of the adaptive filtering paradigm. The convergence process, however, can lead to less than desirable filter performance as was shown in Figure 25, Figure 26, and Figure 27, where the convergence of the filter at the onset of the blink (T1 First Half) results is significantly higher error than after the filter has reached stability (T1 Second Half).

Another form of adaptive filter, the so called least-mean squares (LMS) algorithm, can be applied to the entirety of a time series in post-hoc analysis. In another form, LMS can also be applied as a point-by-point process similar to RLS; for this discussion, only the post-hoc adaptation of LMS is considered, as the point-by-point LMS formulation is not suitably dissimilar in its

functionality from RLS where λ approaches 0. The goal of post-hoc LMS is to determine a single set of filter coefficients, $h_{lms}[m]$, that solve the expected value minimization for the entirety of s[n]; in fact, least-mean squares, by definition, is the minimization (least) of the expected value (mean) of the square of e[n] (squared). LMS adjusts $h_{lms}[m]$ for a given s[n] and r[n] iteratively until a convergence criteria on the error is met. While this results in a single set of coefficients, $h_{lms}[m]$, that are applied to the entirety of r[n], the assumption of stationarity that is afforded by this formulation resolves the filter convergence error that is seen in the RLS formulation of an adaptive filter.

There are many analytic and numerical approaches for solving the general LMS problem. While it is not the goal of this work to determine the most suitable solver, the LMS case is a useful construct for demonstrating how filter convergence may affect the overall error in T1 by eliminating the convergence effect in its entirety and using a single filter, $h_{lms}[m]$, that satisfactorily represents the filter transfer function that allows z[n] to be estimated by $\hat{r}[n]$. For illustration purposes only, consider the RLS algorithm to generate a set of coefficients over the entirety of the available time series s[n] that are attempting to converge on the same stationary process that describes how $\hat{r}[n]$ is estimated from r[n]. In the simulated data here, the propagation of the blink artifact source to the EEG electrode is governed by a single, stationary process; thus, a reasonable estimate to $h_{lms}[m]$ that solves the expected value minimization problem in the least-squares sense is an average of h[m] (or, $h_{lp}[m]$) over the entirety of the time series for which it was recursively derived.

To observe the effect of convergence, the stationary filter response, $h_{lms}[m]$, was calculated for each of the reference noise inputs, r[n] = r(VEOG), r[n] = r(NLM+BARS), and r[n] = r(source), using the lpRLS algorithm. The error in both T1 and T2 was compared between $h_{lp}[m]$ and $h_{lms}[m]$ for each algorithm, and the results derived from ICA for completeness. This allows for

the simulation of LMS without needing to define a specific algorithm for solving the LMS problem that may or may not be theoretically optimal. These results are shown in Figure 46 (temporal aggregate), Figure 47 (exemplar boxplots), and Figure 48 (post-hoc, pairwise multiple comparisons). Because of the number of post-hoc, pairwise comparisons, the full table can be found in Appendix H.

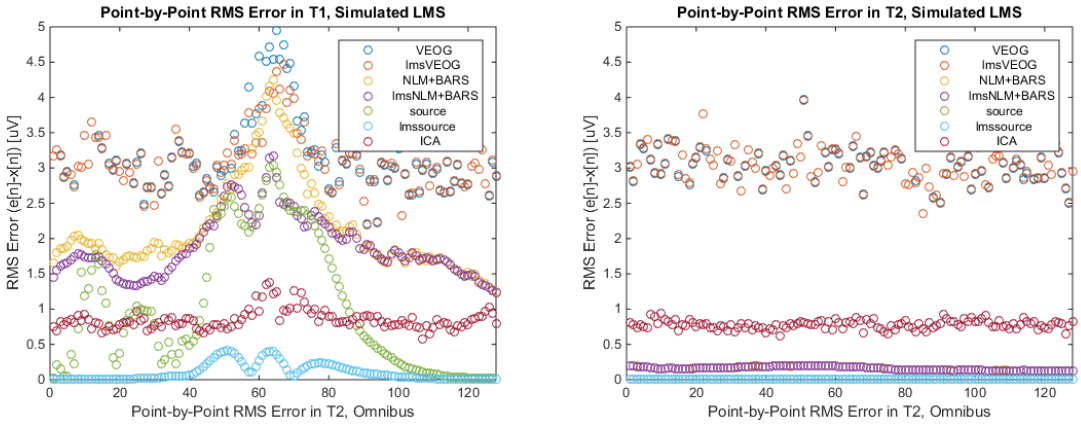

Figure 46. Temporal average RMS error for T1 and T2, simulated LMS.

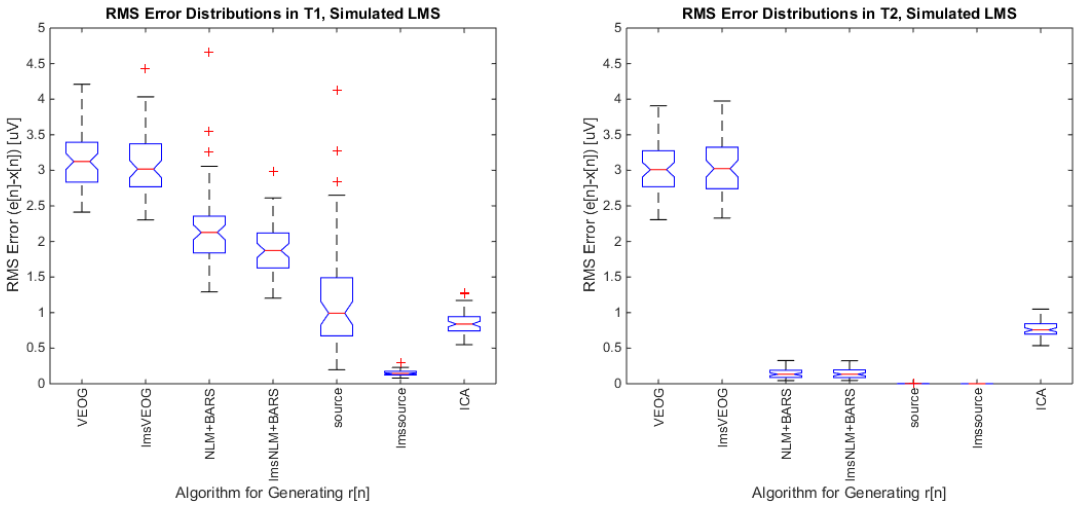

Figure 47. Exemplar RMS error distributions for T1 and T2, simulated LMS.

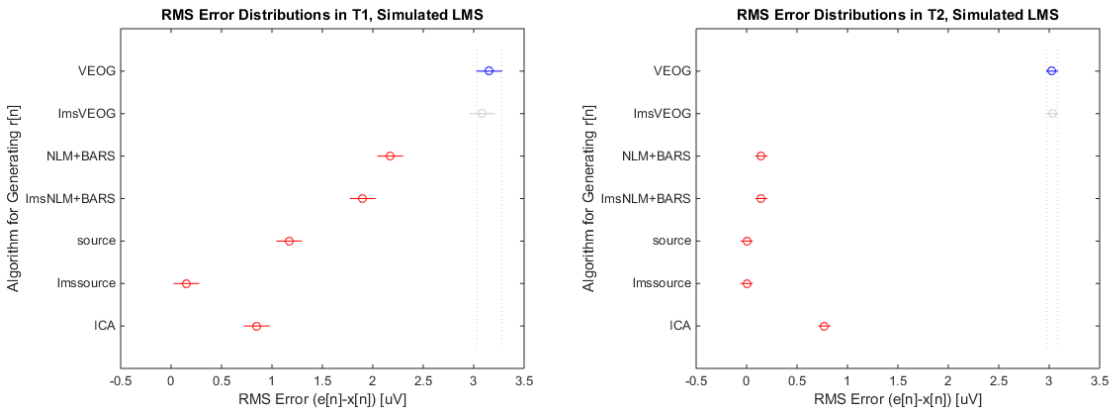

Figure 48. Post-hoc, pairwise comparisons for T1 and T2, omnibus analysis.

The one-way ANOVA for simulated LMS had a significant main effect, $F_{(6,419)} = 366.8763$, $p < 0.001$, $\eta_p^2 = 0.84$, for T1. Post-hoc, pairwise comparisons reveled that both r[n] = r(NLM+BARS) and r[n] = r(source) achieved a significantly ($p < 0.001$) lower error in its simulated LMS implementation than when using lpRLS; the same was not true for VEOG ($p = 0.98$). For T2, the one-way ANOVA also had a significant main effect, $F_{(6,419)} = 2779.2079$, $p < 0.001$, $\eta_p^2 = 98$. The post-hoc, pairwise comparisons for T2 revealed no significant changes between the simulated LMS and lpRLS algorithm implementations for r[n] = r(VEOG), r[n] = r(NLM+BARS), or r[n] = r(source), $p = 1.00$, $p = 1.00$, $p = 1.00$, respectively. Because of the number of post-hoc, pairwise comparisons, the full table can be found in Appendix H.

These simulated LMS results show that when estimating $h_{lms}[m]$ by the average of $h_{lp}[m]$ as determined by lpRLS, assuming that lpRLS is trying to converge on a set of coefficients that accurately describe the stationary process that allows for z[n] to be estimated by $\hat{r}[n]$, the result of eliminating filter convergence is that error in T1 is significantly decreased for both r[n] = r(NLM+BARS) and r[n] = r(source). Using r[n] = r(VEOG), which is already significantly flawed, is not improved by the simulated LMS implementation; neither are the errors during T2, where filter convergence was not observed to be a confound (Figure 21 and Figure 22).

REAL DATA VISUALIZATION

The final algorithm, lpRLS, (NLM+BARS)was applied to a segment of real data; for comparison purposes, traditional RLS, using r[n] = r(VEOG), and ICA were applied to the same data and plotted in Figure 43 and Figure 44. In Figure 43, the recovered, clean EEG signals are plotted against the original signal as measured at Fp1. The noticeable ability of lpRLS(NLM+BARS) to preserve the original EEG when there was otherwise no ocular artifact clearly exceeds that of either RLS or ICA. The estimated noise component is plotted against the original signal measured at Fp1 in Figure 44. Here, the preservation of the blink artifact and the simultaneous, near-ideal elimination of the cross-talk from EEG are evident. In fact, from this Figure, ICA appears to produce the worst results of all three algorithms. The data used to produce the ICA decomposition only contained 5 [min] of data and 134 data channels sampled at 256 [Hz]; thus, the total amount of data did not reach the recommend threshold of $20*N^2$ data points per channel, where N equals the number of data channels in the decomposition [100]. It is possible that this underdetermined data case for ICA lead to what appears to be the least accurate estimated noise source of all three algorithms; this should strongly be considered when interpreting these results. What is quite clear, however, is that the performance of lpRLS(NLM+BARS) far exceeds that that is obtained by traditional RLS, where VEOG is the reference noise input channel.

V. CONCLUSION

This is the first body of work on improving adaptive filtering, without the use of blind source separation, for removing ocular artifact from the EEG to be completed since He et al. [12]. A number of advancements in adaptive filtering theory in this problem space have been made, namely: an improved, biophysically-realistic methodology for simulating data that can be used for meaningful algorithm comparison; a study of and a proposed mitigation for the non-linear phase response of traditional RLS; and, a signal conditioning algorithm for the reference noise input that simultaneously preserves the signature blink noise representation while nearly perfectly eliminating other sources of non-ocular cross-talk, such as EEG. While much work remains to be done, these results unequivocally demonstrate that adaptive filtering has a strong set of advantages for ocular artifact correction when *a prioi* conditions of blind source separation may not be met; in fact, many of the results presented here suggest that adaptive filtering may be capable of producing *better* results that blind source separation for the areas of data that matter the most to ensuring high-quality data analysis. Future work should seek solutions to some of the aforementioned areas of improvement in this algorithm space as well as the application of these methods, and others, to real data for validation and comparison of neurophysiological signals and analyses of interest.

APPENDIX A: A DISCUSSION ON THE FREQUENCY-INDEPENDENCE OF EEG NEUROPHYSICS

Several prominent researchers have reported finding effects of frequency-dependence in empirical, neurophysiological data. For example, Pfurtscheller & Cooper [103] reported the presence of beta waves in subdural electrodes and, simultaneously, an apparent lack of them in scalp electrodes. Knowing that tissue impedance between cortex and scalp had been previously shown to be quite similar for low and high frequencies of interest in EEG, they attributed this effect not to a low-pass characteristic of volume conduction, but to "summation of polyphasic cortical activity." That is to say that high-frequency cortical sources at the neuronal level may be slightly out of phase in comparison to lower-frequency activity over the same relative volume of tissue, thus reducing their coherence. Nunez and Srinivasan [104] offer a similar viewpoint, noting that high-frequency coherence at the cortical level results in the recruitment of a smaller volume of tissue than low-frequency sources, the effect of which is that the observed 'low-pass' behavior is of a spatial, and not of a temporal, of frequency-dependent volume conduction, nature. This explains, in essence, the $1/\sqrt{f}$ magnitude falloff of scalp EEG frequency spectra, whereby coherent, cortical activity of higher frequencies is observed at overall lower power than low-frequency activity.

Some authors (e.g. [34] [29] [105]) have reported a preference for frequency-dependent regression approaches for, in particular, ocular artifact removal. As Lins et al. [85] [106] propose, although not necessarily unique to frequency-dependence, the properties of artifact propagation in the linear regression case may be calculated in error when the presence of other sources, like EEG and EMG, in the EOG channels are not considered, or when the choice of reference signal

may influence results. With the benefit of hindsight and the adoption of more contemporary dipolar source estimation and reconstruction approaches to artifact removal that necessarily rely on frequency-independent volume conduction, it reasonable to assume that previous results arguing for the necessity of frequency-dependent considerations may have, in fact, observed a process not specifically related to volume conduction. As with all scientific debates, the matter of frequency-(in)dependence has been valuable to the community, and thus should be considered of merit.

It should be noted, however, that this assumption of frequency-independence extends only to the properties of volume conduction in and of itself. That does not necessarily rule out other frequency-dependent phenomena that may affect quantitative results, such as post-hoc filtering, complex and variable impedance between the electrode and scalp interface, and A/D amplifier characteristics.

APPENDIX B: THE MATRIX INVERSE OPERATION AND ITS EFFECT ON lpRLS

The process of matrix inversion can lead to numerical imprecision in results. In the work presented here, per the original derivation of Friedlander and Morf [86], the lpRLS method requires a matrix inversion operation in the updating of the linear phase filter coefficients that is part of the recursion algorithm. In the MATLAB function written to execute lpRLS, the 'mrdivide' function is allowed as an alternate to using the inverse function, 'inv', for updating the linear filter coefficients; however, the possibility for small numerical imprecision still exists.

The lpRLS function therefore allows for the user to select from three options: (1) use the (possibly) numerically imprecise coefficients returned by the recursion, (2) reflect the coefficients about the [(M-1)/2]th coefficient from either the lower-order or higher-order coefficients so the resulting filter is perfectly Type I FIR. This will, of course, result in a filter that may have a slightly varying magnitude response than that as determined by the recursion, but is done so to maintain the precise linear phase implementation. All results presented here used MATLAB's 'mrdivide' function in conjunction with reflecting the lower-order coefficients about the [(M-1)/2]th coefficient to preserve linear phase. It may be possible to realize a linear-phase adaptive filter implementation without the need for matrix inversion, but this is beyond the scope of this effort.

APPENDIX C: ESTIMATING SIGNIFICANT EFFECTS FROM BOXPLOTS

It is common practice to use boxplots in order to represent data distributions such that effects of treatments on factors may be estimated from the corresponding data. This is most typically done by looking for overlap in the notches on the boxplots, as that overlap is typically indicative of a lack of pairwise significance ($p > 0.05$) between any two distributions. Main effects ($p < 0.05$) are then observed when at least one boxplot's notches (within a single factor) do not overlap with any of the other levels in that factor. Interaction effects can be observed in the same way, only by looking for changes in the relationship between levels across factors (i.e., a significant difference between levels is found in one factor, but not another). Interactions could also result in the reversal of the relationship between levels across factors (i.e., the relative magnitude between non-overlapping boxplot notches is reversed across factors). Finally, and most simply, pairwise significance can be estimated for any two boxplots regardless of level or factor. Note that these pairwise comparisons do not necessarily take into account any correction for multiple comparisons, and any other observation of main, interaction, or pairwise effects should never be stated or suggested without support of the appropriate statistical test(s). However, as opposed to large table of post-hoc analyses which can be cumbersome to interpret, boxplots allow any researcher to quickly and easily observe distributions that can lead to a more complete understanding of the underlying data.

APPENDIX D: POST-HOC, PAIRWISE COMPARISON TABLE FOR r[n] = VEOG(lowpass)

Table A-1. Post-hoc, pairwise comparisons for T1 and T2 using r[n] = r(lowpass). Comparisons resulting in significant differences ($\rho < 0.05$) are highlighted in orange.

Segment	Paired Comparison	μ	95% CI	p-value
T1	VEOG, fc = 5 [Hz]	-9.22501	[-9.9123, -8.5377]	< 0.001
T1	VEOG, fc = 7.5 [Hz]	-2.98766	[-3.6750, -2.3004]	< 0.001
T1	VEOG, fc = 10 [Hz]	-1.11749	[-1.8048, -0.4302]	< 0.001
T1	VEOG, fc = 15 [Hz]	-0.0517	[-0.7390, 0.6356]	1
T1	VEOG, fc = 20 [Hz]	-0.10889	[-0.7962, 0.5784]	0.999997
T1	VEOG, fc = 25 [Hz]	-0.08121	[-0.7685, 0.6061]	1
T1	VEOG, fc = 30 [Hz]	0.012375	[-0.6749, 0.6997]	1
T1	VEOG, fc = 35 [Hz]	0.087407	[-0.5999, 0.7747]	1
T1	VEOG, fc = 40 [Hz]	0.124927	[-0.5624, 0.8122]	0.999986
T1	VEOG, fc = 5 [Hz]	0.140524	[-0.5468, 0.8278]	0.999953
T1	VEOG, source	1.983738	[1.2964, 2.6710]	< 0.001
T1	fc = 5 [Hz], fc = 7.5 [Hz]	6.237354	[5.5501, 6.9247]	< 0.001
T1	fc = 5 [Hz], fc = 10 [Hz]	8.107525	[7.4202, 8.7948]	< 0.001
T1	fc = 5 [Hz], fc = 15 [Hz]	9.173314	[8.4860, 9.8606]	< 0.001
T1	fc = 5 [Hz], fc = 20 [Hz]	9.116122	[8.4288, 9.8034]	< 0.001
T1	fc = 5 [Hz], fc = 25 [Hz]	9.1438	[8.4565, 9.8311]	< 0.001
T1	fc = 5 [Hz], fc = 30 [Hz]	9.237387	[8.5501, 9.9247]	< 0.001
T1	fc = 5 [Hz], fc = 35 [Hz]	9.312419	[8.6251, 9.9997]	< 0.001
T1	fc = 5 [Hz], fc = 40 [Hz]	9.349938	[8.6626, 10.0372]	< 0.001
T1	fc = 5 [Hz], fc = 45 [Hz]	9.365536	[8.6782, 10.0528]	< 0.001
T1	fc = 5 [Hz], source	11.20875	[10.5215, 11.8960]	< 0.001
T1	fc = 7.5 [Hz], fc = 10 [Hz]	1.870171	[1.1829, 2.5575]	< 0.001
T1	fc = 7.5 [Hz], fc = 15 [Hz]	2.93596	[2.2487, 3.6233]	< 0.001
T1	fc = 7.5 [Hz], fc = 20 [Hz]	2.878768	[2.1915, 3.5661]	< 0.001
T1	fc = 7.5 [Hz], fc = 25 [Hz]	2.906446	[2.2191, 3.5937]	< 0.001
T1	fc = 7.5 [Hz], fc = 30 [Hz]	3.000032	[2.3127, 3.6873]	< 0.001
T1	fc = 7.5 [Hz], fc = 35 [Hz]	3.075065	[2.3878, 3.7624]	< 0.001
T1	fc = 7.5 [Hz], fc = 40 [Hz]	3.112584	[2.4253, 3.7999]	< 0.001
T1	fc = 7.5 [Hz], fc = 45 [Hz]	3.128181	[2.4409, 3.8155]	< 0.001
T1	fc = 7.5 [Hz], source	4.971396	[4.2841, 5.6587]	< 0.001
T1	fc = 10 [Hz], fc = 15 [Hz]	1.06579	[0.3785, 1.7531]	< 0.001
T1	fc = 10 [Hz], fc = 20 [Hz]	1.008598	[0.3213, 1.6959]	< 0.001
T1	fc = 10 [Hz], fc = 25 [Hz]	1.036275	[0.3490, 1.7236]	< 0.001
T1	fc = 10 [Hz], fc = 30 [Hz]	1.129862	[0.4426, 1.8172]	< 0.001
T1	fc = 10 [Hz], fc = 35 [Hz]	1.204894	[0.5176, 1.8922]	< 0.001

T1	fc = 10 [Hz], fc = 40 [Hz]	1.242413	[0.5551, 1.9297]	< 0.001
T1	fc = 10 [Hz], fc = 45 [Hz]	1.258011	[0.5707, 1.9453]	< 0.001
T1	fc = 10 [Hz], source	3.101225	[2.4139, 3.7885]	< 0.001
T1	fc = 15 [Hz], fc = 20 [Hz]	-0.05719	[-0.7445, 0.6301]	1
T1	fc = 15 [Hz], fc = 25 [Hz]	-0.02951	[-0.7168, 0.6578]	1
T1	fc = 15 [Hz], fc = 30 [Hz]	0.064072	[-0.6232, 0.7514]	1
T1	fc = 15 [Hz], fc = 35 [Hz]	0.139105	[-0.5482, 0.8264]	0.999957
T1	fc = 15 [Hz], fc = 40 [Hz]	0.176624	[-0.5107, 0.8639]	0.999552
T1	fc = 15 [Hz], fc = 45 [Hz]	0.192221	[-0.4951, 0.8795]	0.999005
T1	fc = 15 [Hz], fc = source	2.035436	[1.3481, 2.7227]	< 0.001
T1	fc = 20 [Hz], fc = 25 [Hz]	0.027677	[-0.6596, 0.7150]	1
T1	fc = 20 [Hz], fc = 30 [Hz]	0.121264	[-0.5660, 0.8086]	0.999989
T1	fc = 20 [Hz], fc = 35 [Hz]	0.196297	[-0.4910, 0.8836]	0.998791
T1	fc = 20 [Hz], fc = 40 [Hz]	0.233816	[-0.4535, 0.9211]	0.994249
T1	fc = 20 [Hz], fc = 45 [Hz]	0.249413	[-0.4379, 0.9367]	0.9901
T1	fc = 20 [Hz], source	2.092628	[1.4053, 2.7799]	< 0.001
T1	fc = 25 [Hz], fc = 30 [Hz]	0.093587	[-0.5937, 0.7809]	0.999999
T1	fc = 25 [Hz], fc = 35 [Hz]	0.168619	[-0.5187, 0.8559]	0.999713
T1	fc = 25 [Hz], fc = 40 [Hz]	0.206139	[-0.4812, 0.8934]	0.998108
T1	fc = 25 [Hz], fc = 45 [Hz]	0.221736	[-0.4656, 0.9090]	0.996371
T1	fc = 25 [Hz], source	2.06495	[1.3777, 2.7522]	< 0.001
T1	fc = 30 [Hz], fc = 35 [Hz]	0.075033	[-0.6123, 0.7623]	1
T1	fc = 30 [Hz], fc = 40 [Hz]	0.112552	[-0.5747, 0.7998]	0.999995
T1	fc = 30 [Hz], fc = 45 [Hz]	0.128149	[-0.5591, 0.8154]	0.999981
T1	fc = 30 [Hz], source	1.971364	[1.2841, 2.6587]	< 0.001
T1	fc = 35 [Hz], fc = 40 [Hz]	0.037519	[-0.6498, 0.7248]	1
T1	fc = 35 [Hz], fc = 45 [Hz]	0.053116	[-0.6342, 0.7404]	1
T1	fc = 35 [Hz], source	1.896331	[1.2090, 2.5836]	< 0.001
T1	fc = 40 [Hz], fc = 45 [Hz]	0.015597	[-0.6717, 0.7029]	1
T1	fc = 40 [Hz], source	1.858812	[1.1715, 2.5461]	< 0.001
T1	fc = 45 [Hz], source	1.843214	[1.1559, 2.5305]	< 0.001
T2	VEOG, fc = 5 [Hz]	1.684695	[1.4224, 1.9469]	< 0.001
T2	VEOG, fc = 7.5 [Hz]	1.487013	[1.2248, 1.7493]	< 0.001
T2	VEOG, fc = 10 [Hz]	0.962416	[0.7002, 1.2247]	< 0.001
T2	VEOG, fc = 15 [Hz]	0.489361	[0.2271, 0.7516]	< 0.001
T2	VEOG, fc = 20 [Hz]	0.346206	[0.0840, 0.6085]	< 0.001
T2	VEOG, fc = 25 [Hz]	0.255328	[-0.0069, 0.5176]	0.064878
T2	VEOG, fc = 30 [Hz]	0.211148	[-0.0511, 0.4734]	0.261991
T2	VEOG, fc = 35 [Hz]	0.188502	[-0.0737, 0.4508]	0.441419
T2	VEOG, fc = 40 [Hz]	0.17083	[-0.0914, 0.4331]	0.601876
T2	VEOG, fc = 5 [Hz]	0.156113	[-0.1061, 0.4184]	0.730412
T2	VEOG, source	3.026017	[2.7638, 3.2883]	< 0.001
T2	fc = 5 [Hz], fc = 7.5 [Hz]	-0.19768	[-0.4599, 0.0646]	0.363279
T2	fc = 5 [Hz], fc = 10 [Hz]	-0.72228	[-0.9845, -0.4600]	< 0.001
T2	fc = 5 [Hz], fc = 15 [Hz]	-1.19533	[-1.4576, -0.9331]	< 0.001
T2	fc = 5 [Hz], fc = 20 [Hz]	-1.33849	[-1.6007, -1.0762]	< 0.001

T2	fc = 5 [Hz], fc = 25 [Hz]	-1.42937	[-1.6916, -1.1671]	< 0.001
T2	fc = 5 [Hz], fc = 30 [Hz]	-1.47355	[-1.7358, -1.2113]	< 0.001
T2	fc = 5 [Hz], fc = 35 [Hz]	-1.49619	[-1.7584, -1.2339]	< 0.001
T2	fc = 5 [Hz], fc = 40 [Hz]	-1.51387	[-1.7761, -1.2516]	< 0.001
T2	fc = 5 [Hz], fc = 45 [Hz]	-1.52858	[-1.7908, -1.2663]	< 0.001
T2	fc = 5 [Hz], source	1.341322	[1.0791, 1.6036]	< 0.001
T2	fc = 7.5 [Hz], fc = 10 [Hz]	-0.5246	[-0.7868, -0.2623]	< 0.001
T2	fc = 7.5 [Hz], fc = 15 [Hz]	-0.99765	[-1.2599, -0.7354]	< 0.001
T2	fc = 7.5 [Hz], fc = 20 [Hz]	-1.14081	[-1.4031, -0.8786]	< 0.001
T2	fc = 7.5 [Hz], fc = 25 [Hz]	-1.23168	[-1.4939, -0.9694]	< 0.001
T2	fc = 7.5 [Hz], fc = 30 [Hz]	-1.27586	[-1.5381, -1.0136]	< 0.001
T2	fc = 7.5 [Hz], fc = 35 [Hz]	-1.29851	[-1.5608, -1.0363]	< 0.001
T2	fc = 7.5 [Hz], fc = 40 [Hz]	-1.31618	[-1.5784, -1.0539]	< 0.001
T2	fc = 7.5 [Hz], fc = 45 [Hz]	-1.3309	[-1.5931, -1.0686]	< 0.001
T2	fc = 7.5 [Hz], source	1.539004	[1.2768, 1.8013]	< 0.001
T2	fc = 10 [Hz], fc = 15 [Hz]	-0.47305	[-0.7353, -0.2108]	< 0.001
T2	fc = 10 [Hz], fc = 20 [Hz]	-0.61621	[-0.8785, -0.3540]	< 0.001
T2	fc = 10 [Hz], fc = 25 [Hz]	-0.70709	[-0.9693, -0.4448]	< 0.001
T2	fc = 10 [Hz], fc = 30 [Hz]	-0.75127	[-1.0135, -0.4890]	< 0.001
T2	fc = 10 [Hz], fc = 35 [Hz]	-0.77391	[-1.0362, -0.5117]	< 0.001
T2	fc = 10 [Hz], fc = 40 [Hz]	-0.79159	[-1.0538, -0.5293]	< 0.001
T2	fc = 10 [Hz], fc = 45 [Hz]	-0.8063	[-1.0686, -0.5441]	< 0.001
T2	fc = 10 [Hz], source	2.063601	[1.8014, 2.3259]	< 0.001
T2	fc = 15 [Hz], fc = 20 [Hz]	-0.14315	[-0.4054, 0.1191]	0.827162
T2	fc = 15 [Hz], fc = 25 [Hz]	-0.23403	[-0.4963, 0.0282]	0.134935
T2	fc = 15 [Hz], fc = 30 [Hz]	-0.27821	[-0.5405, -0.0160]	0.026345
T2	fc = 15 [Hz], fc = 35 [Hz]	-0.30086	[-0.5631, -0.0386]	0.009693
T2	fc = 15 [Hz], fc = 40 [Hz]	-0.31853	[-0.5808, -0.0563]	0.004141
T2	fc = 15 [Hz], fc = 45 [Hz]	-0.33325	[-0.5955, -0.0710]	0.00195
T2	fc = 15 [Hz], fc = source	2.536655	[2.2744, 2.7989]	< 0.001
T2	fc = 20 [Hz], fc = 25 [Hz]	-0.09088	[-0.3531, 0.1714]	0.99327
T2	fc = 20 [Hz], fc = 30 [Hz]	-0.13506	[-0.3973, 0.1272]	0.876337
T2	fc = 20 [Hz], fc = 35 [Hz]	-0.1577	[-0.4200, 0.1045]	0.71726
T2	fc = 20 [Hz], fc = 40 [Hz]	-0.17538	[-0.4376, 0.0869]	0.560289
T2	fc = 20 [Hz], fc = 45 [Hz]	-0.19009	[-0.4523, 0.0722]	0.427468
T2	fc = 20 [Hz], source	2.67981	[2.4176, 2.9421]	< 0.001
T2	fc = 25 [Hz], fc = 30 [Hz]	-0.04418	[-0.3064, 0.2181]	0.999993
T2	fc = 25 [Hz], fc = 35 [Hz]	-0.06683	[-0.3291, 0.1954]	0.999587
T2	fc = 25 [Hz], fc = 40 [Hz]	-0.0845	[-0.3467, 0.1778]	0.996411
T2	fc = 25 [Hz], fc = 45 [Hz]	-0.09922	[-0.3615, 0.1630]	0.986099
T2	fc = 25 [Hz], source	2.770689	[2.5084, 3.0329]	< 0.001
T2	fc = 30 [Hz], fc = 35 [Hz]	-0.02265	[-0.2849, 0.2396]	1
T2	fc = 30 [Hz], fc = 40 [Hz]	-0.04032	[-0.3026, 0.2219]	0.999997
T2	fc = 30 [Hz], fc = 45 [Hz]	-0.05503	[-0.3173, 0.2072]	0.999939
T2	fc = 30 [Hz], source	2.814869	[2.5526, 3.0771]	< 0.001
T2	fc = 35 [Hz], fc = 40 [Hz]	-0.01767	[-0.2799, 0.2446]	1

T2	fc = 35 [Hz], fc = 45 [Hz]	-0.03239	[-0.2946, 0.2299]	1
T2	fc = 35 [Hz], source	2.837514	[2.5753, 3.0998]	< 0.001
T2	fc = 40 [Hz], fc = 45 [Hz]	-0.01472	[-0.2770, 0.2475]	1
T2	fc = 40 [Hz], source	2.855187	[2.5929, 3.1174]	< 0.001
T2	fc = 45 [Hz], source	2.869904	[2.6077, 3.1322]	< 0.001

APPENDIX E: BARS ALGORITHM IMPLEMENTATION DETEAILS

Due to computational limitations, some adjustments were made to the BARS algorithm in order to make it practically suitable for the time series data used in the aforementioned simulated and real data cases. The BARS implementation used here [94] requires computation of an [NxN] matrix, where N is the overall length of the time series that is being fitted to the adaptive spine functions. For the simulated data case, N = 230,400; at double precision (64 bits per cell in the matrix), the [NxN] matrix would have required nearly 400 GB of available memory for that single variable, alone. Without the availability of large-scale server or supercomputer resources to perform such a computation, it was not possible to implement BARS on the entire time series as a single function call.

Instead, BARS was allowed to fit adaptive spline functions to 1 [s] (256-point)-long pieces of the time series at a time. The resulting output of this BARS implementation was achieved by overlapping the 256-point time series by 255 points and using the 129th data point (approximately the center of the segment) of each overlapped window as the [i]th data point in the filtered time series. The ends of the N = 230,400-point time series were zero-padded to allow for the [i]th data points in the filtered time series to be calculated for the first and last 128 data points, as well. The approximate midpoint of each overlapped window was chosen to mitigate the effects of poor fits at the edges of the time series while also allowing for the BARS algorithm to provide a reasonable, local smoothing of each time window.

Additional parameter settings of the MATLAB implementation of the BARS algorithm [94] involved using the default parameters, ‘bp’, provided by the authors of the code,

with the exception of setting ‘bp.prior_id’ to ‘POISSON’, and ‘bp.dparams’ to ‘4’, as shown in the sample provided with the downloaded code. Also note that it would appear that this algorithm as implemented in the provided code requires a positively-valued time series; to facilitate this, a sufficiently large (+500 [uV]) was applied to the input time series prior to applying BARS, and then subtracted from the filtered time series prior to using it as an input to the adaptive filter. Increased computational efficiency was achieved by using MATLAB’s Parallel Computing Toolbox (for R2014b) to execute each overlapping window calculation, as they are independent and can therefore be executed in a parfor loop. While not discussed in detail elsewhere, the same parallel processing strategy was also used to implement NLM, as local patch comparisons for any given sample point, s, in v, could be executed independently in a similar parfor loop structure.

APPENDIX F: POST-HOC, PAIRWISE COMPARISON TABLE FOR r[n] = VEOG(NLM)

Table A-2. Post-hoc, pairwise comparisons for T1 and T2 using NLM. Comparisons resulting in significant differences ($\rho < 0.05$) are highlighted in orange.

Segment	Paired Comparison	μ	95% CI	p-value
T1	VEOG, P = 1024	-0.08392	[-0.6560, 0.4881]	1
T1	VEOG, P = 512	0.0847	[-0.4874, 0.6567]	1
T1	VEOG, P = 256	0.0918	[-0.4803, 0.6638]	1
T1	VEOG, P = 128	0.1045	[-0.4676, 0.6766]	1
T1	VEOG, P = 64	0.1963	[-0.3758, 0.7683]	0.9908
T1	VEOG, P = 32	0.3215	[-0.2505, 0.8936]	0.7751
T1	VEOG, P = 16	-0.8129	[-1.3849, -0.2408]	0.0003
T1	VEOG, P = 8	-3.4270	[-3.9991, -2.8550]	< 0.001
T1	VEOG, P = 4	-5.8480	[-6.4201, -5.2759]	< 0.001
T1	VEOG, source	1.9792	[1.4071, 2.5513]	< 0.001
T1	P = 1024, P = 512	0.1686	[-0.4035, 0.7407]	0.9973
T1	P = 1024, P = 256	0.1757	[-0.3964, 0.7478]	0.9962
T1	P = 1024, P = 128	0.1884	[-0.3837, 0.7605]	0.9933
T1	P = 1024, P = 64	0.2802	[-0.2919, 0.8523]	0.8925
T1	P = 1024, P = 32	0.4055	[-0.1666, 0.9775]	0.4468
T1	P = 1024, P = 16	-0.7290	[-1.3010, -0.1569]	0.0020
T1	P = 1024, P = 8	-3.3431	[-3.9152, -2.7711]	< 0.001
T1	P = 1024, P = 4	-5.7641	[-6.3361, -5.1920]	< 0.001
T1	P = 1024, source	2.0631	[1.4910, 2.6352]	< 0.001
T1	P = 512, P = 256	0.0071	[-0.5650, 0.5792]	1
T1	P = 512, P = 128	0.0198	[-0.5523, 0.5919]	1
T1	P = 512, P = 64	0.1116	[-0.4605, 0.6837]	0.9999
T1	P = 512, P = 32	0.2369	[-0.3352, 0.8089]	0.9633
T1	P = 512, P = 16	-0.8976	[-1.4696, -0.3255]	< 0.001
T1	P = 512, P = 8	-3.5117	[-4.0838, -2.9397]	< 0.001
T1	P = 512, P = 4	-5.9327	[-6.5047, -5.3606]	< 0.001
T1	P = 512, source	1.8945	[1.3224, 2.4666]	< 0.001
T1	P = 256, P = 128	0.0127	[-0.5594, 0.5848]	1
T1	P = 256, P = 64	0.1045	[-0.4676, 0.6766]	1
T1	P = 256, P = 32	0.2298	[-0.3423, 0.8018]	0.9703
T1	P = 256, P = 16	-0.9047	[-1.4767, -0.3326]	< 0.001
T1	P = 256, P = 8	-3.5188	[-4.0909, -2.9468]	< 0.001
T1	P = 256, P = 4	-5.9398	[-6.5118, -5.3677]	< 0.001
T1	P = 256, source	1.8874	[1.3153, 2.4595]	< 0.001
T1	P = 128, P = 64	0.0918	[-0.4803, 0.6638]	1

T1	P = 128, P = 32	0.2171	[-0.3550, 0.7891]	0.9803
T1	P = 128, P = 16	-0.9174	[-1.4894, -0.3453]	< 0.001
T1	P = 128, P = 8	-3.5315	[-4.1036, -2.9595]	< 0.001
T1	P = 128, P = 4	-5.9525	[-6.5246, -5.3804]	< 0.001
T1	P = 128, source	1.8747	[1.3026, 2.4468]	< 0.001
T1	P = 64, P = 32	0.1253	[-0.4468, 0.6973]	0.9998
T1	P = 64, P = 16	-1.0092	[-1.5812, -0.4371]	< 0.001
T1	P = 64, P = 8	-3.6233	[-4.1954, -3.0513]	< 0.001
T1	P = 64, P = 4	-6.0443	[-6.6163, -5.4722]	< 0.001
T1	P = 64, source	1.7829	[1.2109, 2.3550]	< 0.001
T1	P = 32, P = 16	-1.1344	[-1.7065, -0.5624]	< 0.001
T1	P = 32, P = 8	-3.7486	[-4.3206, -3.1765]	< 0.001
T1	P = 32, P = 4	-6.1695	[-6.7416, -5.5975]	< 0.001
T1	P = 32, source	1.6576	[1.0856, 2.2297]	< 0.001
T1	P = 16, P = 8	-2.6142	[-3.1862, -2.0421]	< 0.001
T1	P = 16, P = 4	-5.0351	[-5.6072, -4.4630]	< 0.001
T1	P = 16, source	2.7921	[2.2200, 3.3641]	< 0.001
T1	P = 8, P = 4	-2.4210	[-2.9930, -1.8489]	< 0.001
T1	P = 8, source	5.4062	[4.8342, 5.9783]	< 0.001
T1	P = 4, source	7.8272	[7.2551, 8.3992]	< 0.001
T2	VEOG, P = 1024	0.0283	[-0.1299, 0.1865]	1
T2	VEOG, P = 512	0.0079	[-0.1503, 0.1661]	1
T2	VEOG, P = 256	0.6549	[0.4967, 0.8131]	< 0.001
T2	VEOG, P = 128	2.7331	[2.5749, 2.8913]	< 0.001
T2	VEOG, P = 64	2.5347	[2.3764, 2.6929]	< 0.001
T2	VEOG, P = 32	2.3180	[2.1597, 2.4762]	< 0.001
T2	VEOG, P = 16	2.1827	[2.0245, 2.3409]	< 0.001
T2	VEOG, P = 8	1.8814	[1.7232, 2.0396]	< 0.001
T2	VEOG, P = 4	1.5452	[1.3870, 1.7035]	< 0.001
T2	VEOG, source	3.0260	[2.8678, 3.1842]	< 0.001
T2	P = 1024, P = 512	-0.0204	[-0.1786, 0.1378]	1
T2	P = 1024, P = 256	0.6266	[0.4684, 0.7848]	< 0.001
T2	P = 1024, P = 128	2.7048	[2.5466, 2.8630]	< 0.001
T2	P = 1024, P = 64	2.5064	[2.3482, 2.6646]	< 0.001
T2	P = 1024, P = 32	2.2897	[2.1314, 2.4479]	< 0.001
T2	P = 1024, P = 16	2.1544	[1.9962, 2.3127]	< 0.001
T2	P = 1024, P = 8	1.8531	[1.6949, 2.0113]	< 0.001
T2	P = 1024, P = 4	1.5169	[1.3587, 1.6752]	< 0.001
T2	P = 1024, source	2.9977	[2.8395, 3.1560]	< 0.001
T2	P = 512, P = 256	0.6470	[0.4888, 0.8053]	< 0.001
T2	P = 512, P = 128	2.7252	[2.5670, 2.8834]	< 0.001
T2	P = 512, P = 64	2.5268	[2.3686, 2.6850]	< 0.001
T2	P = 512, P = 32	2.3101	[2.1518, 2.4683]	< 0.001
T2	P = 512, P = 16	2.1748	[2.0166, 2.3331]	< 0.001
T2	P = 512, P = 8	1.8735	[1.7153, 2.0317]	< 0.001
T2	P = 512, P = 4	1.5374	[1.3791, 1.6956]	< 0.001

T2	P = 512, source	3.0181	[2.8599, 3.1764]	< 0.001
T2	P = 256, P = 128	2.0782	[1.9199, 2.2364]	< 0.001
T2	P = 256, P = 64	1.8798	[1.7215, 2.0380]	< 0.001
T2	P = 256, P = 32	1.6631	[1.5048, 1.8213]	< 0.001
T2	P = 256, P = 16	1.5278	[1.3696, 1.6860]	< 0.001
T2	P = 256, P = 8	1.2265	[1.0683, 1.3847]	< 0.001
T2	P = 256, P = 4	0.8903	[0.7321, 1.0486]	< 0.001
T2	P = 256, source	2.3711	[2.2129, 2.5293]	< 0.001
T2	P = 128, P = 64	-0.1984	[-0.3566, -0.0402]	0.0027
T2	P = 128, P = 32	-0.4151	[-0.5733, -0.2569]	< 0.001
T2	P = 128, P = 16	-0.5504	[-0.7086, -0.3921]	< 0.001
T2	P = 128, P = 8	-0.8517	[-1.0099, -0.6935]	< 0.001
T2	P = 128, P = 4	-1.1878	[-1.3461, -1.0296]	< 0.001
T2	P = 128, source	0.2929	[0.1347, 0.4512]	< 0.001
T2	P = 64, P = 32	-0.2167	[-0.3749, -0.0585]	< 0.001
T2	P = 64, P = 16	-0.3520	[-0.5102, -0.1937]	< 0.001
T2	P = 64, P = 8	-0.6533	[-0.8115, -0.4951]	< 0.001
T2	P = 64, P = 4	-0.9894	[-1.1477, -0.8312]	< 0.001
T2	P = 64, source	0.4913	[0.3331, 0.6496]	< 0.001
T2	P = 32, P = 16	-0.1352	[-0.2935, 0.0230]	0.1774
T2	P = 32, P = 8	-0.4366	[-0.5948, -0.2783]	< 0.001
T2	P = 32, P = 4	-0.7727	[-0.9310, -0.6145]	< 0.001
T2	P = 32, source	0.7081	[0.5498, 0.8663]	< 0.001
T2	P = 16, P = 8	-0.3013	[-0.4596, -0.1431]	< 0.001
T2	P = 16, P = 4	-0.6375	[-0.7957, -0.4793]	< 0.001
T2	P = 16, source	0.8433	[0.6851, 1.0015]	< 0.001
T2	P = 8, P = 4	-0.3362	[-0.4944, -0.1779]	< 0.001
T2	P = 8, source	1.1446	[0.9864, 1.3029]	< 0.001
T2	P = 4, source	1.4808	[1.3226, 1.6390]	< 0.001

APPENDIX G: POST-HOC, PAIRWISE COMPARISON TABLE FOR OMNIBUS ANALYSIS

Table A-3. Post-hoc, pairwise comparisons for T1 and T2 from the omnibus analysis. Comparisons resulting in significant differences ($\rho < 0.05$) are highlighted in orange.

Segment	Paired Comparison	μ	95% CI	p-value
T1	VEOG, Lowpass	-0.0517	[-0.3585, 0.2551]	0.9996
T1	VEOG, BARS	1.0214	[0.7146, 1.3283]	< 0.001
T1	VEOG, NLM	0.1025	[-0.2044, 0.4093]	0.9728
T1	VEOG, BARS+NLM	0.9651	[0.6583, 1.2719]	< 0.001
T1	VEOG, NLM_BARS	0.9832	[0.6764, 1.2901]	< 0.001
T1	VEOG, source	1.9837	[1.6769, 2.2906]	< 0.001
T1	VEOG, ICA	2.3062	[1.9994, 2.6131]	< 0.001
T1	Lowpass, BARS	1.0731	[0.7663, 1.3799]	< 0.001
T1	Lowpass, NLM	0.1542	[-0.1527, 0.4610]	0.7953
T1	Lowpass, BARS+NLM	1.0168	[0.7100, 1.3236]	< 0.001
T1	Lowpass, NLM_BARS	1.0349	[0.7281, 1.3418]	< 0.001
T1	Lowpass, source	2.0354	[1.7286, 2.3423]	< 0.001
T1	Lowpass, ICA	2.3579	[2.0511, 2.6648]	< 0.001
T1	BARS, NLM	-0.9189	[-1.2258, -0.6121]	< 0.001
T1	BARS, BARS+NLM	-0.0563	[-0.3631, 0.2505]	0.9993
T1	BARS, NLM_BARS	-0.0382	[-0.3450, 0.2687]	0.9999
T1	BARS, source	0.9623	[0.6555, 1.2692]	< 0.001
T1	BARS, ICA	1.2848	[0.9780, 1.5917]	< 0.001
T1	NLM, BARS+NLM	0.8626	[0.5558, 1.1695]	< 0.001
T1	NLM, NLM_BARS	0.8808	[0.5739, 1.1876]	< 0.001
T1	NLM, source	1.8813	[1.5744, 2.1881]	< 0.001
T1	NLM, ICA	2.2037	[1.8969, 2.5106]	< 0.001
T1	BARS+NLM, NLM_BARS	0.0181	[-0.2887, 0.3250]	1.0000
T1	BARS+NLM, source	1.0186	[0.7118, 1.3255]	< 0.001
T1	BARS+NLM, ICA	1.3411	[1.0343, 1.6480]	< 0.001
T1	NLM+BARS, source	1.0005	[0.6937, 1.3073]	< 0.001
T1	NLM+BARS, ICA	1.3230	[1.0162, 1.6298]	< 0.001
T1	source, ICA	0.3225	[0.0157, 0.6293]	0.0313
T2	VEOG, Lowpass	0.4894	[0.3272, 0.6515]	< 0.001
T2	VEOG, BARS	2.1721	[2.0099, 2.3343]	< 0.001
T2	VEOG, NLM	2.7331	[2.5709, 2.8953]	< 0.001
T2	VEOG, BARS+NLM	2.9182	[2.7560, 3.0804]	< 0.001
T2	VEOG, NLM_BARS	2.8818	[2.7196, 3.0439]	< 0.001
T2	VEOG, source	3.0260	[2.8638, 3.1882]	< 0.001
T2	VEOG, ICA	2.2552	[2.0930, 2.4174]	< 0.001

T2	Lowpass, BARS	1.6828	[1.5206, 1.8449]	< 0.001
T2	Lowpass, NLM	2.2437	[2.0815, 2.4059]	< 0.001
T2	Lowpass, BARS+NLM	2.4289	[2.2667, 2.5910]	< 0.001
T2	Lowpass, NLM_BARS	2.3924	[2.2302, 2.5546]	< 0.001
T2	Lowpass, source	2.5367	[2.3745, 2.6988]	< 0.001
T2	Lowpass, ICA	1.7659	[1.6037, 1.9280]	< 0.001
T2	BARS, NLM	0.5610	[0.3988, 0.7231]	< 0.001
T2	BARS, BARS+NLM	0.7461	[0.5839, 0.9083]	< 0.001
T2	BARS, NLM_BARS	0.7096	[0.5474, 0.8718]	< 0.001
T2	BARS, source	0.8539	[0.6917, 1.0161]	< 0.001
T2	BARS, ICA	0.0831	[-0.0791, 0.2453]	0.7784
T2	NLM, BARS+NLM	0.1851	[0.0230, 0.3473]	0.0126
T2	NLM, NLM_BARS	0.1487	[-0.0135, 0.3109]	0.1004
T2	NLM, source	0.2929	[0.1308, 0.4551]	< 0.001
T2	NLM, ICA	-0.4779	[-0.6400, -0.3157]	< 0.001
T2	BARS+NLM, NLM_BARS	-0.0365	[-0.1987, 0.1257]	0.9975
T2	BARS+NLM, source	0.1078	[-0.0544, 0.2700]	0.4719
T2	BARS+NLM, ICA	-0.6630	[-0.8252, -0.5008]	< 0.001
T2	NLM+BARS, source	0.1443	[-0.0179, 0.3064]	0.1237
T2	NLM+BARS, ICA	-0.6265	[-0.7887, -0.4644]	< 0.001
T2	source, ICA	-0.7708	[-0.9330, -0.6086]	< 0.001

APPENDIX H: POST-HOC, PAIRWISE COMPARISON TABLE FOR RLS VS. SIMULATED LMS

Table A-4. Post-hoc, pairwise comparisons for T1 and T2 for simulated LMS. Comparisons resulting in significant differences ($p < 0.05$) are highlighted in orange.

Segment	Paired Comparison	μ	95% CI	p-value
T1	VEOG, lmsVEOG	0.0714	[-0.1744, 0.3172]	0.9787
T1	VEOG, NLM+BARS	0.9832	[0.7375, 1.2290]	0.0000
T1	VEOG, lmsNLM+BARS	1.2545	[1.0087, 1.5003]	0.0000
T1	VEOG, source	1.9837	[1.7379, 2.2295]	0.0000
T1	VEOG, lmssource	3.0041	[2.7583, 3.2499]	0.0000
T1	VEOG, ICA	2.3062	[2.0604, 2.5520]	0.0000
T1	lmsVEOG, NLM+BARS	0.9118	[0.6660, 1.1576]	0.0000
T1	lmsVEOG, lmsNLM+BARS	1.1831	[0.9373, 1.4288]	0.0000
T1	lmsVEOG, source	1.9123	[1.6665, 2.1581]	0.0000
T1	lmsVEOG, lmssource	2.9327	[2.6869, 3.1784]	0.0000
T1	lmsVEOG, ICA	2.2348	[1.9890, 2.4806]	0.0000
T1	NLM+BARS, lmsNLM+BARS	0.2712	[0.0255, 0.5170]	0.0196
T1	NLM+BARS, source	1.0005	[0.7547, 1.2463]	0.0000
T1	NLM+BARS, lmssource	2.0208	[1.7750, 2.2666]	0.0000
T1	NLM+BARS, ICA	1.3230	[1.0772, 1.5688]	0.0000
T1	lmsNLM+BARS, source	0.7292	[0.4835, 0.9750]	0.0000
T1	lmsNLM+BARS, lmssource	1.7496	[1.5038, 1.9954]	0.0000
T1	lmsNLM+BARS, ICA	1.0517	[0.8060, 1.2975]	0.0000
T1	source, lmssource	1.0203	[0.7746, 1.2661]	0.0000
T1	source, ICA	0.3225	[0.0767, 0.5683]	0.0021
T1	lmssource, ICA	-0.6979	[-0.9436, -0.4521]	0.0000
T2	VEOG, lmsVEOG	-0.0051	[-0.1158, 0.1055]	1.0000
T2	VEOG, NLM+BARS	2.8818	[2.7711, 2.9924]	0.0000
T2	VEOG, lmsNLM+BARS	2.8824	[2.7717, 2.9930]	0.0000
T2	VEOG, source	3.0260	[2.9153, 3.1367]	0.0000
T2	VEOG, lmssource	3.0271	[2.9164, 3.1378]	0.0000
T2	VEOG, ICA	2.2552	[2.1445, 2.3659]	0.0000
T2	lmsVEOG, NLM+BARS	2.8869	[2.7762, 2.9976]	0.0000
T2	lmsVEOG, lmsNLM+BARS	2.8875	[2.7768, 2.9982]	0.0000
T2	lmsVEOG, source	3.0312	[2.9205, 3.1418]	0.0000
T2	lmsVEOG, lmssource	3.0323	[2.9216, 3.1429]	0.0000
T2	lmsVEOG, ICA	2.2604	[2.1497, 2.3710]	0.0000
T2	NLM+BARS, lmsNLM+BARS	0.0006	[-0.1101, 0.1113]	1.0000
T2	NLM+BARS, source	0.1443	[0.0336, 0.2549]	0.0023
T2	NLM+BARS, lmssource	0.1454	[0.0347, 0.2560]	0.0021

T2	NLM+BARS, ICA	-0.6265	[-0.7372, -0.5159]	0.0000
T2	lmsNLM+BARS, source	0.1437	[0.0330, 0.2543]	0.0025
T2	lmsNLM+BARS, lmssource	0.1448	[0.0341, 0.2554]	0.0022
T2	lmsNLM+BARS, ICA	-0.6271	[-0.7378, -0.5165]	0.0000
T2	source, lmssource	0.0011	[-0.1096, 0.1118]	1.0000
T2	source, ICA	-0.7708	[-0.8815, -0.6601]	0.0000
T2	lmssource, ICA	-0.7719	[-0.8826, -0.6612]	0.0000

REFERENCES

[1] H. Berger, "Über das elektrenkephalogramm des menschen," *Archiv für Psychiatrie Nervenkrankheiten,* vol. 87, no. 1, pp. 527-570, 1929.

[2] S. J. Luck, An introduction to the event-related potential technique, Cambridge, Massachusetts: The MIT Press, 2014.

[3] E. D. Adrian and B. H. Matthews, "The Berger rhythm: potential changes from the occipital lobes in man," *Brain,* vol. 57, pp. 355-385, 1934.

[4] F. A. Gibbs, H. Davis and M. D. Lennox, "The elecro-encephalogram in epilepsy and in conditions of impaired consciousness," *Archives of Neurology and Psychiatry,* vol. 34, no. 6, pp. 1133-1148, 1935.

[5] H. H. Jasper and L. Carmichael, "Electrical potentials from the intact human brain," *Science,* vol. 81, pp. 51-53, 1935.

[6] M. Fatourechi, A. Bashashati, R. K. Ward and G. E. Birch, "EMG and EOG artifacts in brain computer interface systems: A survey," *Clinical Neurophysiology,* vol. 118, no. 3, pp. 480-494, 2007.

[7] E. S. Kappenman and S. J. Luck, "The effects of electrode impedance on data quality and statistical significance in ERP recordings," *Psychophysiology,* vol. 47, no. 5, pp. 888-904, 2010.

[8] C. J. Ochoa and J. Polich, "P300 and blink instructions," *Clinical Neurophysiology,* vol. 111, no. 1, pp. 93-98, 2000.

[9] G. Gratton, "Dealing with artifacts: The EOG contamination of the event-related brain potential," *Behavior Research Methods, Instruments, & Computers,* vol. 30, no. 1, pp. 44-53, 1998.

[10] B. Widrow, J. R. Glover, J. M. McCool, J. Kaunitz, C. S. Williams, R. H. Hearn, J. R. Zeidler, E. Dong and R. C. Goodlin, "Adaptive noise cancelling: Principles and applications," *Proceedings of the IEEE,* vol. 63, no. 12, pp. 1692-1716, 1975.

[11] P. He, G. Wilson and C. Russell, "Removal of ocular artifacts from electro-encephalogram by adaptive filtering," *Medical and Biological Engineering and Computing,* vol. 42, no. 3, pp. 407-412, 2004.

[12] P. He, G. Wilson, C. Russell and M. Gerschutz, "Removal of ocular artifacts from the EEG: a comparison between time-domain regression method and adaptive filtering method using simulated data," *Medical & Biological Engineering & Computing,* vol. 45, no. 5, pp. 495-503, 2007.

[13] J. R. Wolpaw and E. W. Wolpaw, Brain-Computer Interfaces: Principles and Practice, New York, New York: Oxford University Press, Inc., 2012.

[14] T.-W. Lee, M. Girolami and T. J. Sejnowski, "Independent component analysis using an extended infomax algorithm for mixed subgaussian and supergaussian sources," *Neural Computation,* vol. 11, no. 2, pp. 417-441, 1999.

[15] P. L. Nunez and R. Srinivasan, Electric Fields of the Brain: The Neurophysics of EEG, New York, New York: Oxford University Press, Inc., 2006.

[16] D. A. Overton and C. Shagass, "Distribution of eye movement and eyeblink potentials over the scalp," *Electroencephalography and Clinical Neurophysiology,* vol. 27, no. 5, pp. 546-546, 1969.

[17] S. A. Hillyard and R. Galambos, "Eye movement artifact in the CNV," *Electroencephalography and Clinical Neurophysiology,* vol. 28, no. 2, pp. 173-182, 1970.

[18] D. G. Girton and J. Kamiya, "A simple on-line technique for removing eye movement artifacts from the EEG," *Electroencephalography and Clinical Neurophysiology,* vol. 34, no. 2, pp. 212-216, 1973.

[19] R. Verleger, T. Gasser and J. Möcks, "Correction of EOG artifacts in event-related potentials of the EEG: Aspects of reliability and validity," *Psychophysiology,* vol. 19, no. 4, pp. 472-480, 1982.

[20] G. Gratton, M. G. Coles and E. Donchin, "A new method for off-line removal of ocular artifact," *Electroencephalography and Clinical Neurophysiology,* vol. 55, no. 4, pp. 468-484, 1983.

[21] H. V. Semlitsch, P. Anderer, P. Schuster and O. Presslich, "A solution for reliable and valid reduction of ocular artifacts, applied to the P300 ERP," *Psychophysiology,* vol. 23, no. 6, pp. 695-703, 1986.

[22] J. C. Woestenburg, M. N. Verbaten and J. L. Slangen, "The removal of the eye-movement artifact from the EEG by regression analysis in the frequency domain," *Biological Psychology,* vol. 16, no. 1-2, pp. 127-147, 1983.

[23] R. J. Croft and R. J. Barry, "EOG correction: a new perspective," *Electroencephalography and Clinical Neurophysiology,* vol. 107, no. 6, pp. 387-394, 1998.

[24] R. J. Croft and R. J. Barry, "EOG correction: a new aligned-artifact average solution," *Electroencephalography and Clinical Neurophysiology,* vol. 107, no. 6, pp. 395-401, 1998.

[25] R. J. Croft and R. J. Barry, "EOG correction: which regression should we use?," *Psychophysiology,* vol. 37, no. 1, pp. 123-125, 2000.

[26] R. J. Croft and R. J. Barry, "EOG correction of blinks with saccade coefficients: a test and revision of the aligned-artefact average solution," *Clinical Neurophysiology,* vol. 111, no. 3, pp. 444-451, 2000.

[27] R. J. Croft and R. J. Barry, "Removal of ocular artifact from the EEG: a review," *Clinical Neurophysiology,* vol. 30, no. 1, pp. 5-19, 2000.

[28] P. Berg and M. Scherg, "A multiple source approach to the correction of eye artifacts," *Electroencephalography and Clinical Neurophysiology,* vol. 90, no. 3, pp. 229-241, 1994.

[29] T. Gasser, L. Sroka and J. Möcks, "The transfer of EOG activity into the EEG for eyes open and closed," *Electroencephalography and Clinical Neurophysiology,* vol. 61, no. 2, pp. 181-193, 1985.

[30] W. G. Iacono and D. T. Lykken, "Two-year retest stability of eye tracking performance and a comparison of electro-oculographic and infrared recording techniques: evidence of EEG in the electro-oculogram," *Psychophysiology,* vol. 18, no. 1, pp. 49-55, 1981.

[31] W. Barry and G. M. Jones, "Influence of eye lid movement upon electro-oculographic recording of vertical eye movements," *Aerospace Medicine,* vol. 36, pp. 855-858, 1965.

[32] F. Matsuo, J. F. Peters and E. L. Reilly, "Electrical phenomena associated with movements of the eyelid," *Electroencephalography and Clinical Neurophysiology,* vol. 38, no. 5, pp. 507-511, 1975.

[33] P. Berg and M. Scherg, "Dipole models of eye movements and blinks," *Electroencephalography and Clinical Neurophysiology,* vol. 79, no. 1, pp. 36-44, 1991.

[34] T. Elbert, W. Lutzenberger, B. Rockstroh and N. Birbaumer, "Removal of ocular artifacts from the EEG — A biophysical approach to the EOG," *Electroencephalography and Clinical Neurophysiology,* vol. 60, no. 5, pp. 455-463, 1985.

[35] P. Berg and M. Scherg, "Dipole modelling of eye activity and its application to the removal of eye artefacts from the EEG and MEG," *Clinical Physics and Physiological Measurement,* vol. 12, no. A, pp. 49-54, 1991.

[36] S. Makeig, A. J. Bell, T.-P. Jung and T. J. Sejnowski, "Independent component analysis of electroencephalographic data," *Advances in Neural Information Processing Systems,* vol. 8, pp. 145-151, 1996.

[37] R. N. Vigário, "Extraction of ocular artefacts from EEG using independent component analysis," *Electroencephalography and Clinical Neurophysiology,* vol. 103, no. 3, pp. 395-404, 1997.

[38] A. J. Bell and T. J. Sejnowski, "An information-maximization approach to blind separation and blind deconvolution," *Neural Computation,* vol. 7, no. 6, pp. 1129-1159, 1995.

[39] T.-P. Jung, C. Humphries, T.-W. Lee, S. Makeig, M. J. McKeown, V. Iragui and T. J. Sejnowski, "Extended ICA removes artifacts from electroencephalographic recordings," *Advances in Neural Information Processing Systems,* vol. 10, pp. 894-900, 1998.

[40] A. Hyvärinen and E. Oja, "A fast fixed-point algorithm for independent component analysis," *Neural Computation,* vol. 9, no. 7, pp. 1483-1492, 1997.

[41] A. Hyvärinen and E. Oja, "One-unit learning rules for independent component analysis," *Advances in Neural Information Processing Systems,* vol. 9, pp. 480-486, 1997.

[42] A. Delorme and S. Makeig, "EEGLAB: an open source toolbox for analysis of single-trial EEG dynamics including independent component analysis," *Journal of Neuroscience Methods,* vol. 134, no. 1, pp. 9-21, 2004.

[43] T.-P. Jung, C. Humphries, T.-W. Lee, S. Makeig, M. J. McKeown, V. Iragui and T. J. Sejnowski, "Removing electroencephalographic artifacts: comparison between ICA and PCA," *Neural Networks for Signal Processing,* vol. VIII, pp. 63-72, 1998.

[44] T.-P. Jung, S. Makeig, M. Westerfield, J. Townsend, E. Courchesne and T. J. Sejnowski, "Removal of eye activity artifacts from visual event-related potentials in normal and clinical subjects," *Clinical Neurophysiology,* vol. 111, no. 10, pp. 1745-1758, 2000.

[45] T.-P. Jung, S. Makeig, C. Humphries, T.-W. Lee, M. J. McKeown, V. Iragui and T. J. Sejnowski, "Removing electroencephalographic artifacts by blind source separation," *Psychophysiology,* vol. 37, no. 2, pp. 163-178, 2000.

[46] T.-P. Jung, S. Makeig, M. J. McKeown, A. J. Bell, T.-W. Lee and T. J. Sejnowski, "Imaging brain dynamics using independent component analysis," *Proceedings of the IEEE,* vol. 89, no. 7, pp. 1107-1122, 2001.

[47] A. Delorme, J. Palmer, J. Onton, R. Oostenveld and S. Makeig, "Independent EEG sources are dipolar," *PLoS ONE,* vol. 7, no. 2, p. e30135, 2012.

[48] A. Delorme, T. Sejnowski and S. Makeig, "Enhanced detection of artifacts in EEG data using higher-order statistics and independent component analysis," *NeuroImage,* vol. 34, no. 4, pp. 1443-1449, 2007.

[49] F. C. Viola, J. Thorne, B. Edmonds, T. Schneider, T. Eichele and S. Debener, "Semi-automatic indentification of independent components representing EEG artifact," *Clinical Neurophysiology,* vol. 120, no. 5, pp. 868-877, 2009.

[50] M. Chaumon, D. V. M. Bishop and N. A. Busch, "A practical guide to the selection of independent component of the electroencephalogram for artifact correction," *Journal of Neuroscience Methods,* In Press.

[51] L. Frolich, T. S. Andersen and M. Mørup, "Classification of independent components of EEG into multiple artifact classes," *Psychophysiology,* vol. 52, no. 1, pp. 32-45, 2015.

[52] P. LeVan, E. Urrestarazu and J. Gotman, "A system for automatic artifact removal in ictal scalp EEG based on independent component analysis and Bayesian classification," *Clinical Neurophysiology,* vol. 117, no. 4, pp. 912-927, 2006.

[53] A. Mognon, J. Jovicich, L. Bruzzone and M. Bulatti, "ADJUST: an automatic EEG artifact detector based on the joint use of spatial and temporal features," *Psychophysiology,* vol. 48, no. 2, pp. 229-240, 2011.

[54] H. Nolan, R. Whelan and R. B. Reilly, "FASTER: Fully Automated Statistical Thresholding for EEG artifact rejection," *Journal of Neuroscience Methods,* vol. 192, no. 1, pp. 152-162, 2010.

[55] A. Schlögl, C. Keinrath, D. Zimmermann, R. Scherer, R. Leeb and G. Pfurtscheller, "A fully automated correction method of EOG artifacts in EEG recordings," *Clinical Neurophysiology,* vol. 118, no. 1, pp. 98-104, 2007.

[56] A. Schlögl, K.-R. Müller and A. Ziehe, "Automated ocular artifact removal: comparing regression and component-based methods," *Nature Proceedings,* 2009.

[57] C. W. Anderson, J. N. Knight, T. O'Connor, M. J. Kirby and A. Sokolov, "Geometric subspace methods and time-delay embedding for EEG artifact removal and classification," *IEEE Transactions on Neural Systems and Rehabilitation Engineering,* vol. 14, no. 2, pp. 142-146, 2006.

[58] N. Ille, P. Berg and M. Scherg, "Artifact correction of the ongoing EEG using spatial filters based on artifact and brain signal topographies," *Journal of Clinical Neurophysiology,* vol. 19, no. 2, pp. 113-124, 2002.

[59] C. A. Joyce, I. F. Gorodnitsky and M. Kutas, "Automatic removal of eye movement and blink artifacts from EEG data using blink component separation," *Psyuchophysiology,* vol. 41, no. 2, pp. 313-325, 2004.

[60] J. Ma, S. Bayram, P. Tao and V. Svetnik, "igh-throughput ocular artifact reduction in multichannel electroencephalography (EEG) using component subspace projection," *Journal of Neuroscience Methods,* vol. 196, no. 1, pp. 131-140, 2011.

[61] L. Parra and P. Sajda, "Blind source separation via generalized eigenvalue decomposition," *The Journal of Machine Learning Research,* vol. 4, pp. 1261-1269, 2003.

[62] R. Sameni and C. Gouy-Pailler, "An iterative subspace denoising algorithm for removing electroencephalogram ocular artifacts," *Journal of Neuroscience Methods,* vol. 225, pp. 97-105, 2014.

[63] W. Du, H. M. Leong and A. S. Gevins, "Ocular artifact minimization by adaptive filtering," in *IEEE Seventh SP Workshop on Statistical Signal and Array Processing*, 1994.

[64] C. J. James, M. T. Hagan, R. D. Jones, P. J. Bones and G. J. Carroll, "Multireference adaptive noise canceling applied to the EEG," *IEEE Transactions on Biomedical Engineering,* vol. 44, no. 8, pp. 775-779, 1997.

[65] S. Selvan and R. Srinivasan, "Removal of ocular artifacts from EEG using an efficient neural network based adaptive filtering technique," *IEEE Signal Processing Letters,* vol. 6, no. 12, pp. 330-332, 1999.

[66] C. A. Kothe and S. Makeig, "BCILAB: a platform for brain–computer interface development," *Journal of Neural Engineering,* vol. 10, p. 056014, 2013.

[67] F. Ghaderi, S. K. Kim and E. A. Kirchner, "Effects of eye artifact removal methods on single trial P300 detection, a comparative study," *Journal of Neuroscience Methods,* vol. 221, pp. 41-47, 2014.

[68] J. C. Christensen and J. R. Estepp, "Coadaptive aiding and automation enhance operator performance," *Human Factors,* vol. 55, no. 5, pp. 965-975, 2013.

[69] J. R. Estepp and J. C. Christensen, "Electrode replacement does not affect classification accuracy in dual-session use of a passive brain-computer interface for assessing cognitive workload," *Frontiers in Neuroscience,* vol. 9, no. 54, 2015.

[70] G. L. Wallstrom, R. E. Kass, A. Miller, J. F. Cohn and N. A. Fox, "Automatic correction of ocular artifacts in the EEG: a comparison of regression-based and component-based methods," *International Journal of Psychophysiology,* vol. 53, no. 2, pp. 105-119, 2004.

[71] I. Dimatteo, C. R. Genovese and R. E. Kass, "Bayesian curve-fitting with free-knot splines," *Biometrika,* vol. 88, no. 4, pp. 1055-1071, 2001.

[72] S. Romero, M. A. Mañanas and M. J. Barbanoj, "Ocular reduction in EEG signals based on adaptive filtering, regression, and blind source separation," *Annals of Biomedical Engineering,* vol. 37, no. 1, pp. 176-191, 2009.

[73] J. J. M. Kierkels, G. J. M. van Boxtel and L. L. M. Vogten, "A model-based objective evaluation of eye movement correction in EEG recordings," *IEEE Transactions on Biomedical Engineering,* vol. 53, no. 2, pp. 246-253, 2006.

[74] J. J. M. Kierkels, J. Riani, J. W. M. Bergmans and G. J. M. van Boxtel, "Using an eye tracker for accurate eye movement artifact correction," *IEEE Transactions on Biomedical Engineering,* vol. 54, no. 7, pp. 1256-1267, 2007.

[75] B. Noureddin, P. D. Lawrence and G. E. Birch, "Online removal of eye movement and blink EEG artifacts using a high-speed eye tracker," *IEEE Transactions on Biomedical Engineering,* vol. 59, no. 8, pp. 2103-2110, 2011.

[76] M. Plöchl, J. P. Ossandón and P. König, "Combining EEG and eye tracking: identification, characterization, and correction of eye movement artifacts in electroencephalographic data," *Frontiers in Human Neuroscience,* vol. 6, p. 278, 2012.

[77] S. Puthusserypady and T. Ratnarajah, "H∞ adaptive filters for eye blink artifact minimization from electroencephalogram," *IEEE Signal Processing Letters,* vol. 12, no. 12, pp. 816-819, 2005.

[78] S. Puthusserypady and T. Ratnarajah, "Robust adaptive techniques for minimization of EOG artefacts from EEG signals," *Signal Processing,* vol. 86, no. 9, pp. 2351-2363, 2006.

[79] H.-L. Chan, Y.-T. Tsai, L.-F. Meng and T. Wu, "The removal of ocular artifacts from EEG signals using adaptive filters based on ocular source components," *Annals of Biomedical Engineering,* vol. 38, no. 1, pp. 3489-3499, 2010.

[80] A. Belourchrani, K. Abed-Meraim, J.-F. Cardoso and E. Moulines, "A blind source separation technique using second-order statistics," *IEEE Transactions on Signal Processing,* vol. 45, no. 2, pp. 434-444, 1997.

[81] M. A. Klados, C. Papadelis, C. Braun and P. D. Bamidis, "REG-ICA: A hybrid methodology combining Blind Source Separation and regression techniques for the rejection of ocular artifacts," *Biomedical Signal Processing and Control,* vol. 6, no. 3, pp. 291-300, 2011.

[82] N. P. Castellanos and V. A. Makarov, "Recovering EEG brain signals: Artifact suppression with wavelet enhanced independent component analysis," *Journal of Neuroscience Methods,* vol. 158, no. 2, pp. 300-312, 2006.

[83] M. Kirkove, C. François and J. Verly, "Comparative evaluation of existing and new methods for correcting ocular artifacts in electroencephalographic recordings," *Signal Processing,* vol. 98, pp. 102-120, 2014.

[84] P. Berg and M. Scherg, "A fast method for forward computation of multiple-shell spherical head models," *Electroencephalography and Clinical Neurophysiology,* vol. 90, no. 1, pp. 58-64, 1994.

[85] O. G. Lins, T. W. Picton, P. Berg and M. Scherg, "Ocular artifacts in EEG and event-related potentials I: Scalp topography," *Brain Topography,* vol. 6, no. 1, pp. 51-63, 1993.

[86] B. Friedlander and M. Morf, "Least squares algorithms for adaptive linear-phase filtering," *IEEE Transactions on Acoustics, Speech and Signal Processing,* vol. 30, no. 3, pp. 381-390, 1982.

[87] S. Butterworth, "On the theory of filter amplifiers," *Wireless Engineer,* vol. 7, no. 6, pp. 536-541, 1930.

[88] A. Buades, B. Coll and J. M. Morel, "A non-local algorithm for image denoising," in *IEEE Computer Society Conference on Computer Vision and Pattern Recognition*, San Diego, CA, USA, 2005.

[89] A. Buades, B. Coll and J. M. Morel, "A review of image denoising algorithms, with a new one," *Multiscale Modeling & Simulation,* vol. 4, no. 2, pp. 490-530, 2005.

[90] B. H. Tracey and E. L. Miller, "Nonlocal means denoising of ECG signals," *IEEE Transactions on Biomedical Engineering,* vol. 59, no. 9, pp. 2383-2386, 2012.

[91] P. Coupé, P. Yger, S. Prima, P. Hellier, C. Kervrann and C. Barillot, "An optimized blockwise nonlocal means denoising filter for 3-D magnetic resonance images," *IEEE Transactions on Medical Imaging,* vol. 27, no. 4, pp. 425-441, 2008.

[92] J. V. Manjón, J. Carbonnel-Caballero, J. J. Lull, G. Garcia-Marti, L. Marti-Bonmati and M. Robles, "MRI denoising using Non-Local Means," *Medical Image Analysis,* vol. 12, no. 4, pp. 514-523, 2008.

[93] E. M. Whitham, K. J. Pope, S. P. Fitzgibbon, T. Lewis, C. R. Clark, S. Loveless, M. Broberg, A. Wallace, D. DeLosAngeles, P. Lillie, A. Hardy, R. Fronsko, A. Pulbrook and J. O. Willoughby, "Scalp electrical recording during paralysis: Quantitative evidence that EEG frequencies above 20Hz are contaminated by EMG," *Clinical Neurophysiology,* vol. 118, no. 8, pp. 1877-1888, 2007.

[94] G. Wallstrom, J. Liebner and R. E. Kass, "An implementation of Bayesian adaptive regression splines (BARS) in C with S and R wrappers," *Journal of Statistical Software,* vol. 26, no. 1, pp. 1-21, 2008.

[95] K. McDowell, C.-T. Lin, K. S. Oie, T.-P. Jung, S. Gordon, K. W. Whitaker, S.-Y. Li, S.-W. Lu and W. D. Hairston, "Real-world neuroimaging technologies," *IEEE Access,* vol. 1, pp. 131-149, 2013.

[96] B. W. McMenamin, A. J. Shackman, J. S. Maxwell, D. R. W. Bauchhuber, A. M. Koppenhaver, L. L. Greischar and R. J. Davidson, "Validation of ICA-based myogenic artifact correction for scalp and source-localized EEG," *NeuroImage,* vol. 49, no. 3, pp. 2416-2432, 2010.

[97] B. W. McMenamin, A. J. Shackman, L. L. Greischar and R. J. Davidson, "Electromyogenic artifacts and electroencephalographic inferences revisited," *NeuroImage,* vol. 54, no. 1, pp. 4-9, 2011.

[98] G. F. Wilson, J. A. Caldwell and C. A. Russell, "Performance and psychophysiological measures of fatigue effects on aviation related tasks of varying difficulty," *The International Journal of Aviation Psychology,* vol. 17, no. 2, pp. 219-247, 2007.

[99] G. F. Wilson and C. A. Russell, "Performance enhancement in an uninhabited air vehicle task using psychophysiologically determined adaptive aiding," *Human Factors,* vol. 49, no. 6, pp. 1005-1018, 2007.

[100] J. Onton, M. Westerfield, J. Townsend and S. Makeig, "Imaging human EEG dynamics using independent component analysis," *Neuroscience & Biobehavioral Reviews,* vol. 30, no. 6, pp. 808-822, 2006.

[101] Y.-L. Liu, J. Wang, X. Chen, Y.-W. Guo and Q.-S. Peng, "A robust and fast non-local means algorithm for image denoising," *Journal of Computer Science and Technology,* vol. 23, no. 2, pp. 270-279, 2008.

[102] D. Van De Ville and M. Kocher, "SURE-based non-local means," *IEEE Signal Processing Letters,* vol. 16, no. 11, pp. 973-976, 2009.

[103] G. Pfurtscheller and R. Cooper, "Frequency dependence of the transmission of the EEG from cortex to scalp," *Electroencephalography and Clinical Neurophysiology,* vol. 38, no. 1, pp. 93-96, 1875.

[104] P. L. Nunez and R. Srinivasan, "Neocortical dynamics due to axon propagation delays in cortico-cortical fibers: EEG traveling and standing waves with implications for top-down influences on local networks and white matter disease," *Brain Research,* vol. 1542, pp. 138-166, 2014.

[105] T. Gasser, L. Sroka and J. Möcks, "The correction of EOG artifacts by frequency dependent and frequency independent methods," *Psychophysiology,* vol. 23, no. 6, pp. 704-712, 1986.

[106] O. G. Lins, T. W. Picton, P. Berg and M. Scherg, "Ocular artifacts in recording EEGs and event-related potentials II: Source dipoles and source components," *Brain Topography,* vol. 6, no. 1, pp. 65-78, 1993.

[107] T. Åkerstedt and M. Gillberg, "Subjective and objective sleepiness in the active individual," *International Journal of Neuroscience,* vol. 52, no. 1-2, pp. 29-37, 1990.